# MICRO-AND NANOSTRUCTURING OF POLYVINYLIDENE FLUORIDE WITH TAILORED CRYSTAL POLYMORPHS AND ENHANCED PIEZOELECTRIC PROPERTY

JI EUN LEE

A THESIS SUBMITTED TO THE FACULTY OF GRADUATE STUDIES

IN PARTIAL FULFILMENT OF THE REQUIREMENTS FOR THE DEGREE OF

MASTER OF APPLIED SCIENCE

GRADUATE PROGRAM IN MECHANICAL ENGINEERING

YORK UNIVERSITY

TORONTO, ONTARIO

AUGUST 2018

# ABSTRACT

Polyvinylidene fluoride (PVDF) has garnered interest due to its piezoelectric property and as a non-toxic, conformable, and low-cost alternative to the popular piezoelectric ceramic. A novel processing method through the combination of thermal and supercritical carbon dioxide ($ScCO_2$) has been used to successfully promote the formation of electroactive phases (i.e., $\beta$ and $\gamma$ phases), as well as its piezoelectric property. In this report, the processing-to-structure properties and mechanisms that affect crystallization behaviors of electroactive phases were elucidated. It was revealed that $\gamma$ crystal formation was through thermal processing while $\beta$ phase was nucleated through fast cooling and physical foaming of $CO_2$ bubbles. The results were comparable to common processing method and literature, with a maximum electroactive crystal phase of 72.2% and a corresponding piezoelectric coefficient of 7.7 pC/N. The findings in this study could provide insight to future research work on PVDF, advancing its development in piezoelectric applications.

# ACKNOWLEDGEMENTS

To my parents and my brother. Thank you for everything.

# TABLE OF CONTENTS

# LIST OF TABLES

# LIST OF FIGURES

# LIST OF ABBREVIATIONS AND SYMBOLS

| **Abbreviations** | **Description** |
|---|---|
| PVDF | Polyvinylidene fluoride |
| P(VDF-TrFE) | Polyvinyledenedifluoride–Trifluoroethylene |
| PZT | Lead Zirconate Titanate |
| $CO_2$ | Carbon Dioxide |
| $ScCO_2$ | Supercritical Carbon Dioxide |
| VER | Volume Expansion Ratio |
| SEM | Scanning electron microscopy |
| DSC | Differential scanning calorimetry |
| FTIR | Fourier transform infrared spectroscopy |
| XRD | X-Ray diffractometer |

| **Symbols** | **Description** |
|---|---|
| $\alpha$ | Alpha crystal |
| $\beta$ | Beta crystal |
| $\gamma$ | Gamma crystal |
| $T_H$ | Heating temperature |
| $t_{hold}$ | Holding time |
| $T_{sat}$ | Saturation temperature |
| $P_{sat}$ | Saturation pressure |
| $-dP/dt$ | Pressure drop rate |
| $\rho$ | Density of bulk PVDF (1.789 g $cm^{-3}$) |
| $\rho_{water@Tw}$ | Density of water at $T_w$ |
| $T_w$ | Water temperature |
| $m_{air}$ | Sample's mass measured in air |
| $m_{water}$ | Sample's mass measured in water |
| $N_o$ | Cell population density |
| $n$ | Number of cells in SEM micrograph |

| | |
|---|---|
| $M$ | Magnification factor of SEM micrograph |
| $A$ | Area of SEM micrograph |
| $\chi_c$ | Degree of crystallinity |
| $\Delta H_f$ | Heat of fusion of PVDF sample |
| $\Delta H_{f(Crys)}$ | Heat of fusion of 100% crystalline PVDF (104.7 J/g) |
| $F_{EA}$ | Fraction of electroactive crystal phase in PVDF's crystalline region |
| $A_{EA}$ | Electroactive phase absorbance band (840 $cm^{-1}$) |
| $A_\alpha$ | $\alpha$ phase absorbance band (763 $cm^{-1}$) |
| $F_\beta$ | Fraction of $\beta$ crystal phase in PVDF's crystalline region |
| $F_\gamma$ | Fraction of $\gamma$ crystal phase in PVDF's crystalline region |
| $\Delta H_\beta$ | Height between $\beta$ crystal peak at 1275 $cm^{-1}$ to its nearest valley |
| $\Delta H_\gamma$ | Height between $\gamma$ crystal peak at 1234 $cm^{-1}$ to its nearest valley |
| $d_{31}$ | Piezoelectric coefficient in the 3-1 mode |

# LIST OF APPENDICES

# Chapter 1 Introduction

## 1.1 Background and Motivation

Piezoelectric effect is the appearance of an electrical charge when mechanical stress is applied (Figure 1.1) [1]. Due to this property, piezoelectric materials have been utilized in a wide range of industries from automotive to medical to military [2]. Their applications include tactile and infrared imaging sensors, acoustic sound transducers, as well as possible nanogenerators [3] [4]. Barium Titanate ($BaTiO_3$) was the first ferroelectric ceramic discovered and was used in many of the mentioned applications, especially as multilayer capacitors. However, despite its excellent piezoelectric property, $BaTiO_3$ has a low Curie temperature (i.e., 100°C). This makes its polarization unstable due to the complex changes in its lattice [5]. Currently, the most commonly used piezoelectric material is a ceramic, Lead Zirconate Titanate (PZT). Its excellent piezoelectric property makes it ideal for many uses, but PZT has a high lead content and its lead toxicity is causing concerns [6]. With the world moving away from such harmful elements and emerging lead restrictions, the uses of PZT will eventually be eliminated. Polyvinylidene Fluoride (PVDF) is a thermoplastic fluoropolymer from the polymerization of vinylidene difluoride. This piezoelectric polymer provides an inexpensive, environmentally friendly, and conformable alternative to the toxic PZT [7]. Moreover, PVDF and its copolymer with trifluoroethylene (TrFE) have been found to be suited for the high frequency applications in the 100 MHz range, such as ultrasonic transducers in biomedical imaging, that PZT's grain sizes will not allow [8] [9]. However, despite all of PVDF's great advantages, its piezoelectric property is

low and not yet ready to replace its ceramic counterpart PZT [10]. Therefore, the research on PVDF and the promotion of its piezoelectric property has drawn extensive interests from researchers all over the world, perceiving great potential for novel organic electronic devices and energy harvesters.

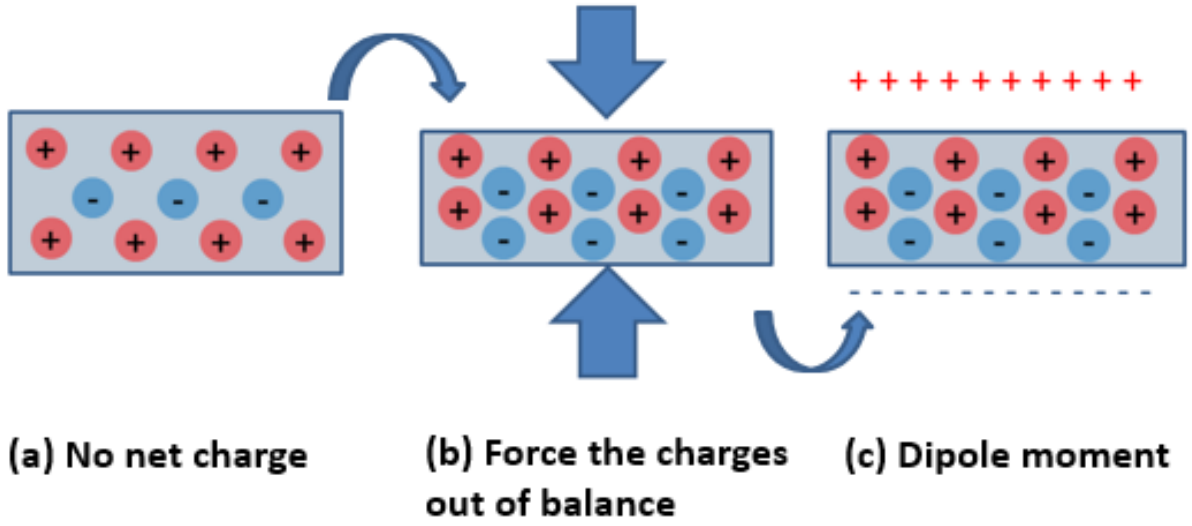


**Figure 1.1 Piezoelectric Effect**

## 1.2 Polyvinylidene fluoride (PVDF) and its co-polymer

Polyvinylidene fluoride (PVDF) is a ferroelectric polymer that exhibits spontaneous electric polarization and develops charge when external stress is applied [11]. This piezoelectric property comes from the polymer's unique crystal structure. PVDF is semi-crystalline and its crystalline structure conforms in five distinct polymorphs (i.e. $\alpha$, $\beta$, $\gamma$, $\delta$, and $\varepsilon$) [7]. $\alpha$ and $\delta$ have trans-gauche-trans-gauche (TGTG') chain conformation, $\beta$ has zigzag all-trans (TTT) chain confirmation, and $\gamma$ and $\varepsilon$ have $T_3GT_3G$' chain conformation. Out of these five polymorphs, $\alpha$, $\beta$,

and $\gamma$ phases are the most researched, with the two latter being electroactive. PVDF is most commonly found in the non-polar $\alpha$ phase due to its stability; however it can be transformed into the electroactive phases through various processing methods. Out of the two electroactive phases, $\beta$ phase has a higher dipole moment (i.e. $8 \times 10^{-30}$ Cm) per unit cell, and thereby has the best piezoelectric property [12]. This is due to the particular alignment of the positive Hydrogen and negative Fluorine atoms of PVDF, maximizing the polarization within the unit cell (Figure 1.2). Therefore, the development of new processing strategies to promote PVDF's piezoelectric property through the increases in the degree of crystallinity and the electroactive crystal phases are very desirable to convert PVDF into a commercially usable material.

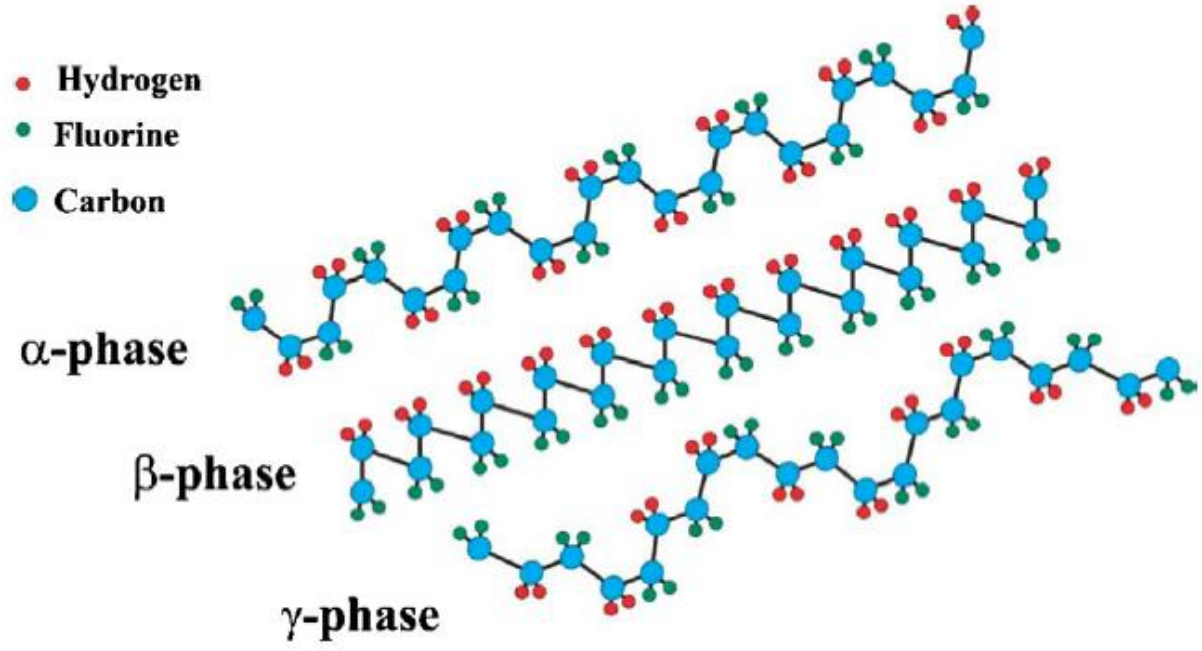


**Figure 1.2 Crystalline structures of $\alpha$, $\beta$, and $\gamma$ phases of PVDF with positive Hydrogen and negative Fluorine atoms, on a Carbon skeleton [7], Copyright 2013. Reproduced with permission from Elsevier.**

Ever since the discovery of the piezoelectric effect in PVDF by Heiji Kawai in 1969 [2], researchers have found increasing number of applications for PVDF in various fields. A common PVDF application is in the biomedical field. Riberiro *et al.* [13] observed that the positively charged $\beta$ PVDF films can provide enough electrical stimuli for the growth of specific cells, a quality advantageous in medical research such as cancer therapy [14]. Recent research involved using PVDF films to replace the polyethylene separator membrane of conventional Lithium ion batteries [15]. The piezoelectric potential from mechanical strain would drive Lithium ions to migrate from the cathode to the anode, accompanied by charging reactions at the electrode [16]. There have also been continued research from 1984 until now on PVDF energy harvesters. Due to PVDF's flexibility, it was easily integrated into clothes, shoes [17], or even a dog's rib cage [18], using the natural motion to generate an electric charge to power wearable electronics. In 2015, Wong *et al.* [19] harvested vibration energy from PVDF when it was impacted by rain drops. They looked at parameters such as rain drop size, fall velocity, and impact types of the raindrop onto the material. While they were able to produce a maximum voltage of 3.5V, they saw the limitations of this device to be used outdoors. More specifically, how this device will be affected by the natural environment (i.e., sunlight and wind) while still being sensitive enough for raindrop impacts.

PVDF copolymer with trifluoroethylene (TrFE) is the most studied piezoelectric copolymer because it is able to crystallize predominantly in the $\beta$ phase [20]. The introduction of TrFE units to PVDF stabilized the all-trans (TTT) chain conformation, yielding a material with high piezoelectric property. However, due to the third Fluorine atom per repeat unit from the

TrFE, the dipole moment of the PVDF chain is reduced [21]. PVDF-TrFE copolymer can be produced as thin films or membranes with controlled micro-porosity, making it ideal for lithium-ion battery applications. However, many processing methods are focused on pure PVDF, making its enhanced version readily usable for any composite, post-processing step, or application.

## 1.3 Thesis organization

Chapter 1 summarized the background of piezoelectric materials, the motivation for this research, and the selected piezoelectric polymer PVDF and its co-polymer, including its current applications. Chapter 2 is a literature review of conventional processing methods utilized to promote the electroactive phases of PVDF. These processing methods include those on pure PVDF, such as mechanical stretching and annealing, as well as the use of high voltage and nanofillers. Additionally, it includes background on the post processing poling step and common methods to measure piezoelectric property. The chapter ends with the proposed research's main objectives. Chapter 3 and 4 discusses the two different experimental methods used in the novel PVDF processing technique, including material used, film preparation, characterization analysis, and its distinct processing phases utilizing temperature, pressure, and time. Chapter 4 will also briefly compare the results of the proposed novel processing method to a current popular method. Chapter 5 discusses the experimental procedure and results to successfully quantify the piezoelectric property of the processed PVDF samples, including the electric poling post-processing step. Finally, Chapter 6 concludes this research along with future work recommendations. The appendices provide additional details of the work done for this research.

# Chapter 2 Literature Review

Processing of PVDF can be accomplished through many strategies and conditions to promote specific polymorphs and/or the crystallinity by aligning the crystal in specific conformations. The processing methods compiled below were effective and good motivators for the current PVDF research. These methods have been split into those that promote the electroactive $\beta$ and $\gamma$ crystals individually. Lastly, the post processing electric poling step and common methods to measure and analyze the piezoelectric property of PVDF are reviewed.

## 2.1 Processing to promote $\beta$ phase crystals

With the best piezoelectric property amongst all polymorphs, the $\beta$ crystal phase of PVDF has been the most extensively researched. Many different processing methods have been proposed to achieve high $\beta$ crystal phase content, each with their own advantages and disadvantages. This section will cover common and notable processing methods which include mechanical stretching, annealing, fast cooling, high pressure, electric poling, electrospinning, supercritical carbon dioxide, and the use of nanofillers.

### 2.1.1 Mechanical Stretching

The most commonly used method to achieve a high $\beta$ phase content is through uniaxial mechanical stretching of PVDF films or filaments. This method relied on two main parameters: temperature and an applied uniaxial stress. With a raised temperature, the mobility of the chain

groups increased. By applying uniaxial stress, the molecular chain groups rearranged from the non-polar $\alpha$ phase to the polar $\beta$ phase's TTT conformation following the uniaxial tensile direction (Figure 2.1) [22]. The optimal stretching temperature was found to be above the glass transition temperature, $\alpha_c$ (i.e., 80°C), which is the initiation temperature for $\alpha$ to $\beta$ phase transformation [23]. When the stretching temperature was below $\alpha_c$, the high viscosity of the material resulted in low chain mobility. This meant that the PVDF molecular chain groups composed of Carbon, Hydrogen, and Fluorine atoms were not free to move, lowering its probability to change its conformation. However, when the temperature went beyond 100°C, the mobility of the chain groups increased too much, decreasing the $\beta$ phase content. Therefore, the optimal temperature was observed to be between 80°C to 100°C [22] [24].

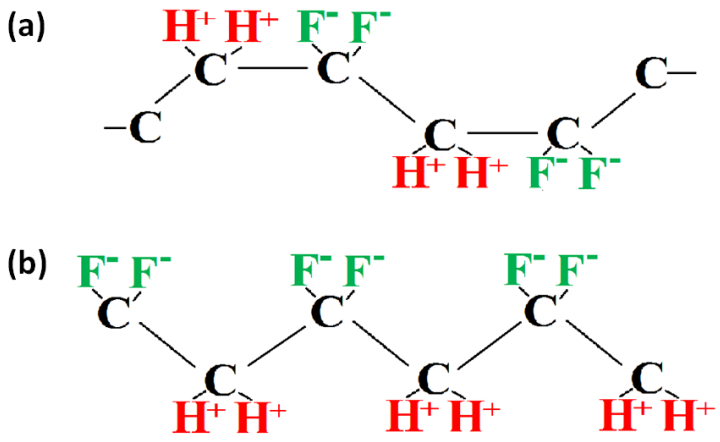


**Figure 2.1 Structures of (a) non-polar $\alpha$ phase and (b) electroactive $\beta$ phase of PVDF with Hydrogen and Fluorine atoms on a Carbon skeleton.**

Kim *et al.* [25] stretched PVDF films by 40% at 90°C. They saw no transformation from $\alpha$ to the $\beta$ phase and concluded that the stretch ratio (i.e., final to initial length) was too low

causing a low $\beta$ phase content. The optimal stretch ratio was found to be approximately five [22] [26] and the stretching speed was observed to have minimal effect on the $\beta$ phase content [26].

Many found that the deformation process from mechanical stretching led to a partial destruction of the crystalline structure, resulting in a decrease in the degree of crystallinity [27] [28]. Mechanical stretching PVDF yielded a maximum $\beta$ phase content, $F_\beta$, of 80% and a corresponding degree of crystallinity, $\chi_c$, of 40.6% [29].

### 2.1.2 Annealing

Annealing of PVDF films has also shown to promote $\beta$ phase formation by increasing PVDF's molecular chain group mobility. Satapathy *et al.* [30] observed that the ideal temperature for this process was just above $\alpha_c$, as previously observed for the mechanical stretching process. At low temperatures (i.e., < 80°C), the temperature was not sufficient to destroy the crystalline order present in the PVDF film, resulting in no change of phase. $\alpha$ to $\beta$ transformation was initiated around 90°C, with the $\beta$ phase formation optimized at 100°C due to the increase in chain group mobility. However, above 115°C, the excessive increase in chain mobility caused $\beta$ phase chain groups to revert back to the more stable $\alpha$ phase. Benz *et al.* [31] observed that the annealing method does not create or destroy crystals but rather transform the crystal phases to one another, such as the $\alpha$ to $\beta$ transformation.

### 2.1.3 Fast Cooling

Soin *et al.* [32] quenched PVDF samples from 100°C to -20°C, and observed a transformation

from 90% $\alpha$ phase to 98% $\beta$ phase, the nucleation of $\beta$ phase being favored at low temperatures [33]. They also observed that fast quenching at this low temperature induced a strong thermal field gradient, causing the crystals to align along this thermal field direction. Gradys *et al.* [34] observed that increasing the cooling rate above 150 K/s enhanced the formation of $\beta$ phase. Further increase of the cooling rate to 2000 K/s caused $\alpha$ crystallization to stop, resulting in the formation of only $\beta$ crystals. Oka *et al.* [35] explained these concepts following that the nucleation of $\beta$ crystals are lower than that of the $\alpha$ crystals. During slow quenching, the sample spends most of the time in the high temperature region. This time is long enough to complete the nucleation of $\alpha$ crystals. After this process, there is no room in the sample for the nucleation of $\beta$ crystals when the sample reaches the lower temperature region, resulting in a dominant $\alpha$ phase sample. During fast quenching, the time to pass through the high temperature region is too short for the nucleation of $\alpha$ crystals to occur in an appreciable amount. Therefore, the nucleation mainly proceeds in the lower temperature region leading to form predominantly $\beta$ phase sample.

### 2.1.4 High Pressure

Melt crystallization of PVDF samples at high pressure starting from 14.5 kpsi to 91 kpsi resulted in 81% $\beta$ phase crystals [36]. When this pressure was further increased to 116 kpsi, PVDF samples with 100% $\beta$ phase crystals were yielded. This was coupled with an increase in temperature to 234°C. It was observed that $\beta$ crystals started to form above 50 kpsi, the tight conformation of the $\beta$ phase being more stable at high pressures and temperatures compared to that of the $\alpha$ phase [37].

Scheinbeim *et al.* [36] illustrated their findings, depicting at which temperature and pressure the nucleation of $\beta$ phase can be achieved (Figure 2.2). From this graph, the formation of $\beta$ phase crystal will occur at temperatures above 230°C and pressures above 50 kpsi, similar to the findings by Matsushige *et al.* [37].

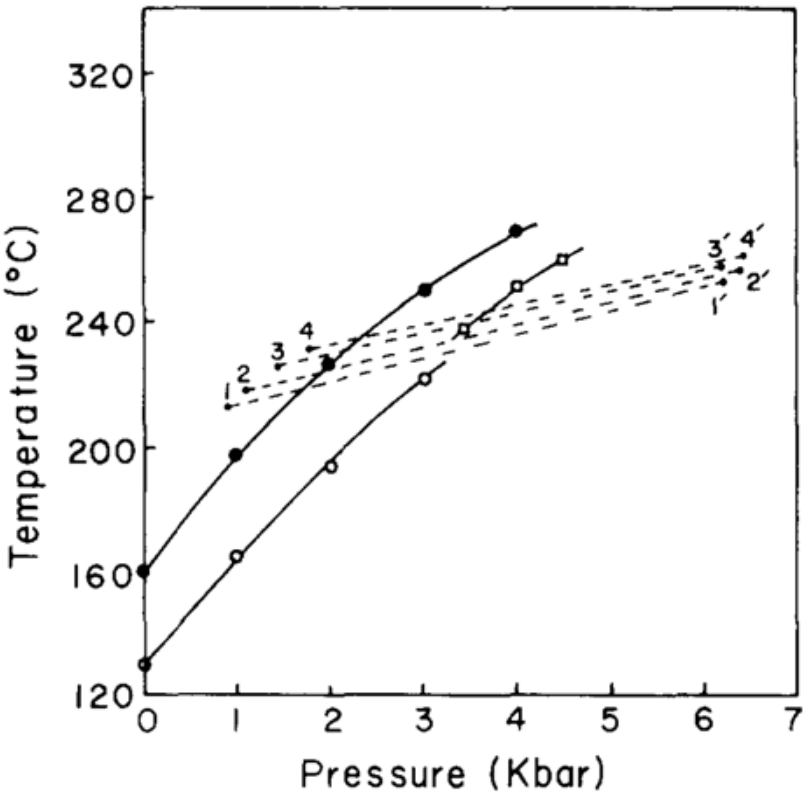


**Figure 2.2 Plot of the melting of $\alpha$ crystals (●), crystallization of $\alpha$ crystals (○), and the crystallization of $\beta$ crystals (□) at high temperatures and pressures. The dotted lines represent different initial and final processing conditions. [36], Copyright 2018. Reproduced with permission from AIP Publishing.**

### 2.1.5 Electric Poling

Electric poling utilizes an applied high electrical field to align the dipoles of the PVDF matrix,

resulting in polarization. There are two different electric poling methods: contact and corona poling. While contact poling has a simpler setup, corona poling had been able to better promote $\beta$ crystals. Corona poling utilizes a high voltage applied to the tip of the needle to ionize the air above the polymer (Figure 2.3). The polarized ions in the air travel down to the PVDF sample below due to the charged metal grid in between and the ground plate underneath the sample. Mahadeva *et al.* [38] observed that without a charged metal grid in between, very few ions reached the sample below due to the small potential difference between the grid and the ground plate underneath sample. As the applied voltage to the metal grid was increased, the ions could easily pass through the grid and reach the sample. With an optimal applied voltage of 2 kV to the metal grid, $F_\beta$ content of 85% was yielded.

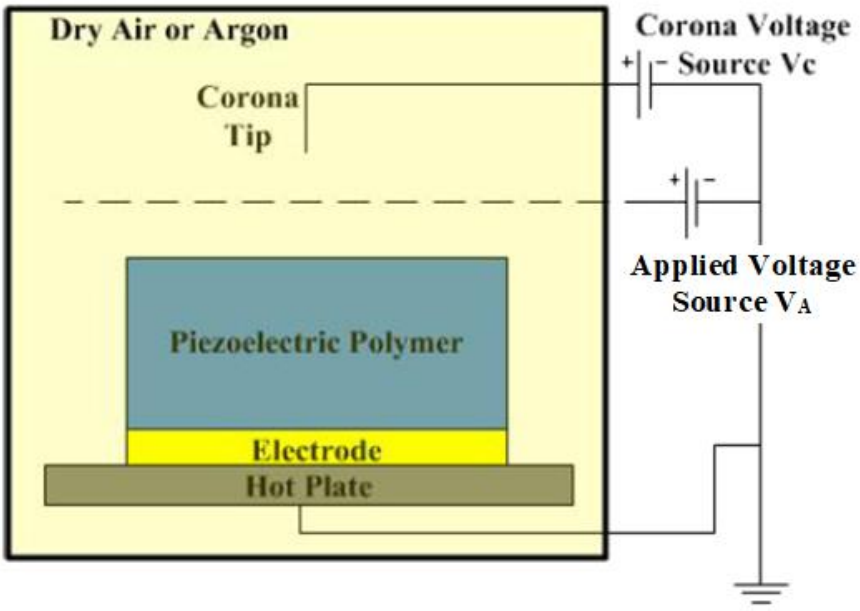


**Figure 2.3 Schematic of Corona Poling [39], Copyright 2018. Reproduced with permission from IOP Publishing.**

### 2.1.6 Electrospinning

A more recently reported approach to promote $\beta$ phase formation in PVDF is electrospinning. This can simultaneously induce mechanical stretching and electric poling in a single processing step [40]. In this approach, a high voltage of 15kV is applied at the opening of a small nozzle [41] . The voltage is high enough for the polymer solution inside the nozzle to overcome surface tension and eject itself out of the nozzle and onto a moving collector plate (Figure 2.4). This method has been advantageous for mass production of nanofibers. The morphologies and the crystal forms are controlled through variations in applied voltage, spinning temperature, flow rate, nozzle size, and the distance between the nozzle and the collecting plate [42] [43]. Zheng *et al.* [44] observed that lowering the spinning temperature, decreasing the flow rate, and reducing the separation distance between the nozzle and the collecting plate promoted the formation of $\beta$ crystals in the electrospun PVDF fibers. Zhong *et al.* [45] observed that the mechanical stretching portion of the electrospun PVDF fibers was responsible for the high $\beta$ phase content. This was proven to be true when the mechanical stretching portion was removed and it produced predominantly $\alpha$ phase samples.

While one key advantage of electrospinning is not requiring any post-processing step, the electrostatically driven jet of polymer solution can only yield electroactive PVDF fibers in submicron to nanoscale. PVDF nanofiber arrays are also produced with random orientation so the polarities cancel out one another such that the overall electric outputs are close to zero [42].

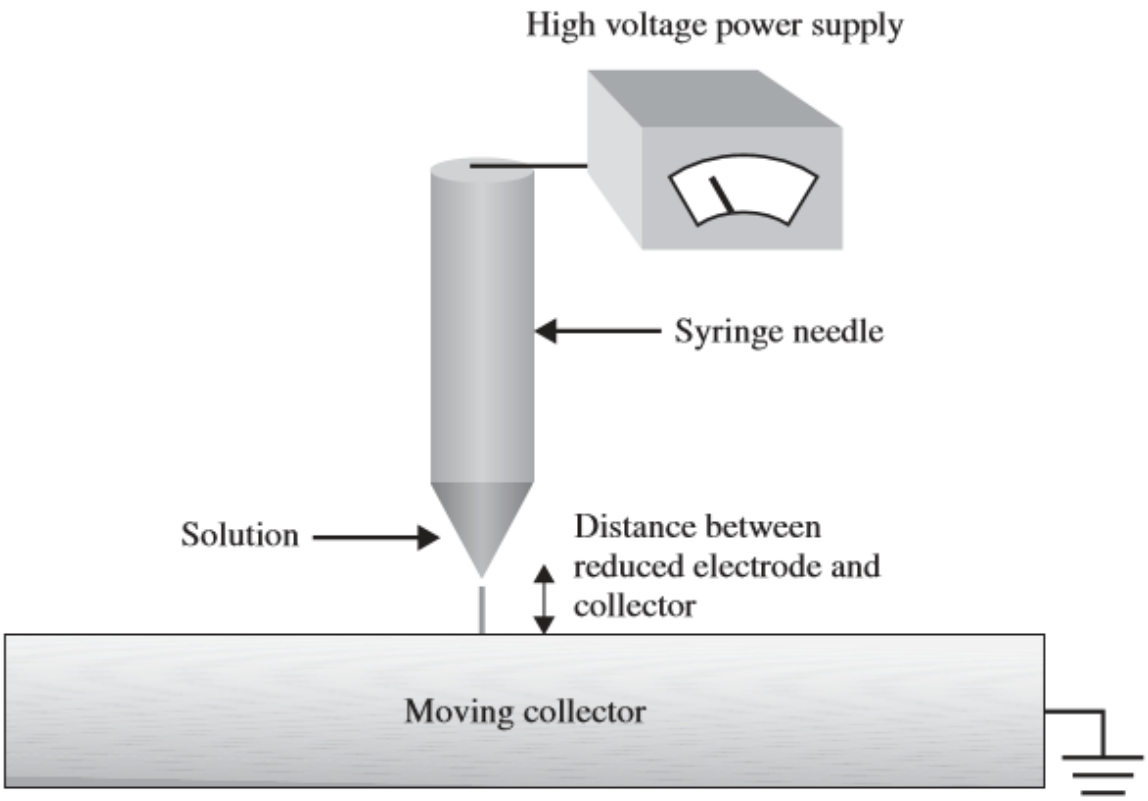


**Figure 2.4 Schematic of electrospinning method [42], Copyright 2014. Reproduced with permission from John Wiley and Sons.**

### 2.1.7 Supercritical Carbon Dioxide

An uncommon method to increase PVDF's electroactive $\beta$ phase content is through supercritical carbon dioxide ($ScCO_2$) processing. Carbon dioxide ($CO_2$) is environmentally benign, non-flammable, chemically inert, inexpensive, and non-toxic, allowing processing at moderate conditions [46]. $CO_2$ is also commonly used due to its well-known properties and its condensability at certain pressures. This causes a more rapid sorption process, allowing an

enhanced $CO_2$ induced plasticization effect on the material [47] [48]. Xiang *et al.* [49] observed that during $ScCO_2$ processing at high pressures, the PVDF sample underwent fast crystallization which favored the formation of $\beta$ crystals. Shieh *et al.* [50] did not see a change when varying pressures from 1200 to 7000 psi, but that may be due to their low operational temperature of 140°C.

### 2.1.8 Nanofillers

While all the previous processing methods dealt with pure PVDF, the addition of nanofillers has yielded great results in the formation of $\beta$ crystals [51]. Martins *et al.* [52] saw a strong interaction between the positive $CH_2$ dipoles of PVDF and the negatively charged surfaces of the $CoFe_2O_4$ nanofillers (Figure 2.5). This dipole-ion interaction resulted in a stabilized TTT conformation on the negative surfaces of the nanofillers. Thakur *et al.* [53] utilized the effects of the stronger hydrogen bonds between the Fluorine atoms of PVDF and –OH groups of $Ni(OH)_2$ fillers to form a larger number of $\beta$ crystal conformation that they have denoted as TTTT conformation. They achieved a $\beta$ crystal phase content of 82% and a degree of crystallinity of 53.8%. Sebastian *et al.* [54] observed that while negatively charge nanofillers promoted the $\beta$ phase nucleation in PVDF, positive surface nanoparticles failed to nucleate the $\beta$ phase.

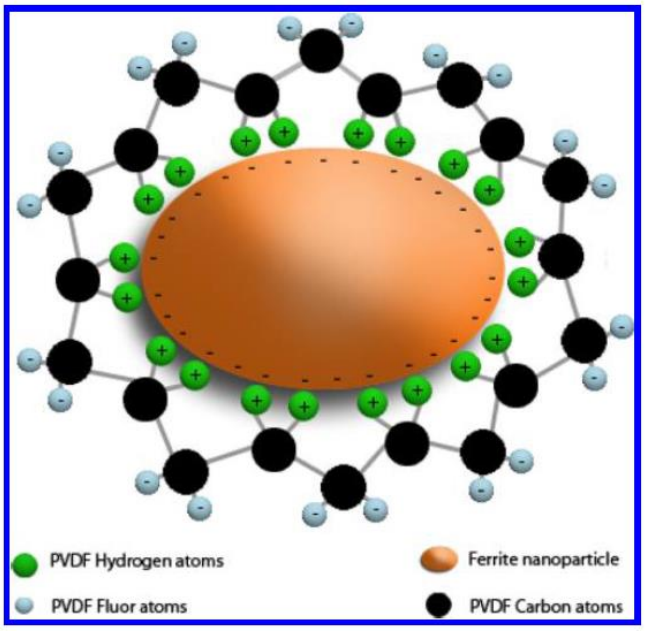


**Figure 2.5 Schematic of hydrogen bonds between PVDF and $Ni(OH)_2$ filler to form a longer TTTT $\beta$ phase conformation [52], Copyright 2012. Reproduced with permission from American Chemical Society.**

## 2.2 Processing to promote $\gamma$ phase crystals

While most researchers focused their efforts to promote the formation of $\beta$ phase crystals in PVDF, some researchers have attempted to identify potential methods to facilitate the formation of the electroactive $\gamma$ phase crystals.

### 2.2.1 Annealing

Various studies revealed that melt crystallization at extremely high temperatures (i.e., close to the melting temperature of $\gamma$ phase crystals) and at very slow cooling rates [55] promoted the formation of $\gamma$ phase crystals. Silva *et al.* [56] observed the formation of $\gamma$ crystals from the $\alpha$

phase spherulites already present in the polymer. Due to $\gamma$ phase's high stability, the amount of $\gamma$ crystals increased with increasing temperature. Using $\alpha$ crystals as seeds, many had observed that processing at extremely high temperatures (i.e., >160°C) for long periods (i.e., 95 hours) combined with a slow cooling rate (i.e., 2°C/min) enhanced the $\gamma$ phase due to its slow crystallization rate [57] [58]. It was observed that prolonged isothermal crystallization time nucleated the $\gamma'$ phase, the result of a direct $\alpha$ to $\gamma$ phase transformation. This crystal phase had a melting point 8°C higher than the regular $\gamma$ phase melting peak (i.e., 180°C) because the transformation took place during a long annealing process and therefore, the crystals formed were more organized [59].

### 2.2.2 Nanofillers

Similar to using nanofillers to promote the nucleation of the $\beta$ phase, the addition of fillers was also used for the promotion of $\gamma$ phase. Using a PVDF nanocomposite with montmorillonite clay, it was observed that the sample tended to crystallize in the $\gamma$ phase below a processing temperature of 210°C. Above this temperature, the elimination of interlayer water caused a reduction in interlayer spacing of the nanoparticle fillers. This resulted in a reduction of contact area between the negative fillers and the PVDF dipolar moments [60], reducing the nucleation of $\gamma$ phase crystals. Lopes *et al.* [61] observed a critical nanoparticle size where the nanofillers lose its nucleation efficiency if it is too small relative to polymer macromolecules (Figure 2.6(a)). Beyond the critical size, more of the monomer chains were in contact with the nanoparticle surfaces, resulting in effective transformation to the $\gamma$ phase conformation (Figure 2.6(b)). It was

also observed that while the ion-dipole interactions from the addition of nanofillers provide energy for the formation of the $T_3GT_3G'$ $\gamma$ conformation, these interactions also reduced the mobility of polymer chains, resulting in lower growth rate of $\gamma$ crystals compared to that of $\alpha$ crystals [62]. Therefore, longer time was needed to adjust to the proper conformation for the nucleation of $\gamma$ phase.

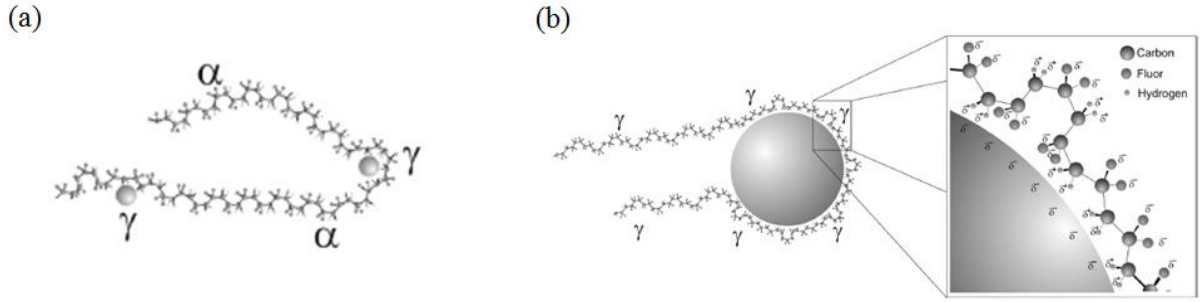


**Figure 2.6 PVDF dipoles interacting with: (a) small 6nm Ag nanoparticles; and (b) large 60 nm Ag nanoparticles. [61], Copyright 2013. Reproduced with permission from John Wiley and Sons.**

## 2.3 Post processing electric poling

Contact electric poling has a simple setup of two electrodes on either side of the sample and an applied electric field across the sample thickness to align the dipoles of the material, resulting in polarization (Figure 2.7). Due to polarization's nonlinearity with applied electrical field, the alignment of dipoles can only be achieved if the applied electrical field is greater than the material's coercive field (i.e., point where dipoles start to switch directions) [63]. However, if the applied electrical field is too high, breakdown of the material could occur. This will be evident by signs of burning, flashovers, and/or increase in the current in the circuit due to the applied

voltage physically breaking through the material and creating a direct path through [64]. Wang *et al.* [65] used a dielectric plate in between the electrode and the sample to limit the current through the polymer and reduce the probability of a dielectric breakdown. For typical PVDF, the coercive and breakdown field is around 0.05 – 0.12 kV/μm and 0.42 kV/μm, respectively [66].

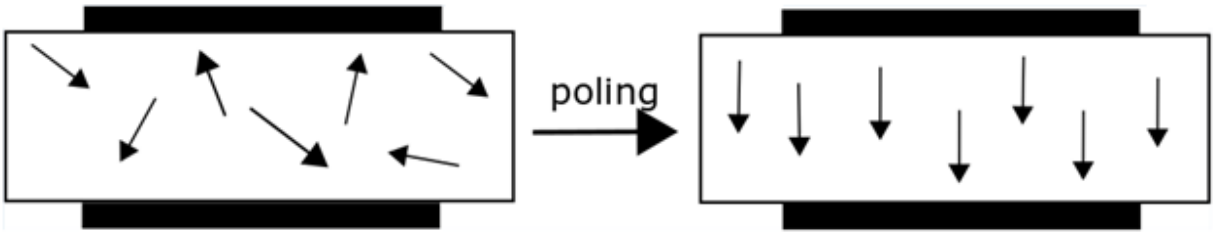


**Figure 2.7 Reorientation of PVDF dipoles via contact electric poling.**

Other than voltage, there are many factors that affect the polarization of a material such as electrode, poling temperature, poling time, and medium. Poor contact of pressed on electrodes may lead to local discharges, breakdown, or non-homogenous poling fields [67]. Therefore, evaporated, sputtered, or painted electrodes are recommended for the superior contact. While many had recommended poling at an elevated temperature (i.e., 85 – 103°C) [67] due to the increased dipole mobility, Sessler [68] observed that if poling time was long enough, polarization is only a function of poling field. Poling temperature, in this case, affected only the rate of polarization, not the final degree of polarization. Blevin [69] observed that between poling temperatures of 20°C to 100°C, poling temperature had little effect as long as poling time was sufficient. With piezoelectric property reaching saturation at a poling time of 30 minutes, long poling times were implemented (i.e., 1 hour) to negate effects associated with poling time

[38] [70]. Additionally, Mopsik *et al.* [71] observed that poling at room temperature avoided non-uniform temperature problems that would induce non-uniform polarization. Kenney *et al.* [66] compared contact poling in an oil versus air medium and saw very little difference in the breakdown time. Many papers reported a standard poling field of 0.1 kV/μm at room temperature to successfully pole PVDF [72] [73].

## 2.4 Measurement of Piezoelectric Property

A material's piezoelectric property can be quantified by measuring and calculating for its piezoelectric coefficient, $d_{ij}$. The *i* and *j* variables are the directional components for the induced charge and stress applied, respectively (Figure 2.8). The directionality is important because PVDF is anisotropic due to their unique crystalline structure [74]. The most commonly measured piezoelectric coefficients is $d_{33}$ because it can apply a greater stress along the thickness of the material. The $d_{33}$ value can be obtained using the normal load method [75]. This method uses a round metallic tip to apply a force downwards towards the sample, causing a compressive stress on that section of the sample, and measures the charge induced in the same direction. While it is a simple setup, the stiff tip applying force on thin films will always have air gaps, which may result in a large measurement errors [76]. To determine $d_{31}$, a simple tensile setup can be used, applying tension in the 1 direction and measuring the charge developed in the 3 direction [77]. The most popular method is the cantilever method. With one end of the film fixed and the other end free, the film will experience uniaxial strain along its 1 direction when a load is applied at the free end causing a deflection. This method has high sensitivity and reliability in data due to

the measurement procedure being similar to real sensor applications. However, the assumptions of zero strain along the 3 direction and uniformity of uniaxial strain along the beam that are necessary to use this method are precarious [78].

Newman *et al.* [70] applied heat treatment followed by poling and achieved a $d_{31}$ of 7.0 pC/N. Wang *et al.* [79] and Das-Gupta *et al.* [80] used particularly high electric fields (i.e., >0.2 kV/μm) to obtain $d_{31}$ values of 7.2 pC/N and 5.8 pC/N through contact and corona poling, respectively. Haghiashtiani *et al.* [81] measured the piezoelectric coefficient of a carbon fiber-reinforced PVDF but got a $d_{31}$ value much lower than expected, due to with the majority of the stress developed on the carbon fiber layer and not the PVDF sample. Kaura *et al.* [82] simultaneously applied mechanical stretching and corona poling at an elevated temperature and obtained a significantly high $d_{31}$ value of 60 pC/N. This was twice the $d_{31}$ values if the two processing steps occurred sequentially.

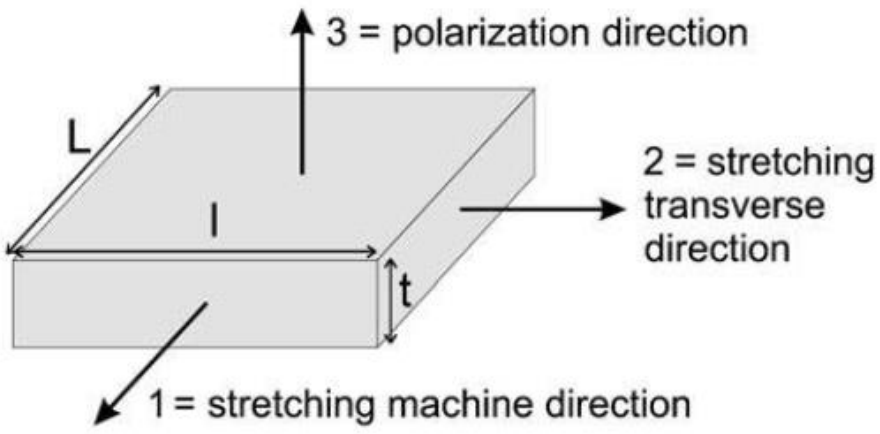


**Figure 2.8 Directional axis for piezoelectric coefficient measurement [1], Copyright 2018. Reproduced with permission from Emerald Publishing.**

## 2.5 Objectives

The main objectives of this research have been split into long term objective, looking at the big picture, and short term objective, exploring the first starting steps and goals of the proposed research.

### 2.5.1 Long term objective

The long term objective of the proposed research is to develop PVDF with excellent piezoelectric property by altering its crystal structure using industrial viable methods. The successful completion of this objective would successfully replace the toxic piezoelectric ceramic PZT and spearhead PVDF into commercial applications including energy harvesters. This is an objective that will be achieved beyond this research.

### 2.5.2 Short term objectives

The short term, and main, objective of the proposed research is to elucidate the crystallization and crystal phase formation of PVDF under different processing strategies, mainly utilizing thermal and supercritical carbon dioxide ($ScCO_2$) processing. By understanding the mechanisms that control the crystal phase using a more industrially viable method, the electroactive crystal phases (i.e., $\beta$ and $\gamma$) can be promoted, leading to an enhancement in piezoelectric property. Therefore, this is an important initial step to achieve the long-term goal of producing a PVDF polymer with an enhanced piezoelectric property to replace the toxic PZT.

It is hypothesized that by using a combination of thermal and $ScCO_2$ processing, PVDF's

electroactive $\gamma$ and $\beta$ phases will be promoted, respectively. The thermal processing through multiple temperature profiles and prolonged time will allow molecular chain groups to orient themselves in the stable $\gamma$ phase due to its tight conformation. By utilizing $CO_2$ in the supercritical state, more $CO_2$ is able to dissolve within the polymer at a faster rate due to having high diffusivity, density, and solubility, the combined properties of both gas and liquid. $ScCO_2$ processing will allow $CO_2$ bubble growth inside the polymer and generate stress within the PVDF matrix. It is possible that the stress generated from bubble growth could be comparable to the strain caused by mechanical stretching to align PVDF's crystal dipoles. While mechanical stretching is commonly used, this process is irregular between samples and even resulting in non-piezoelectric regions within the sample. $ScCO_2$ processing is adaptable to any existing processing lines and the polymer processed can be readily used, making it an industrial viable method.

# Chapter 3 Thermal and $ScCO_2$ Processing of PVDF – Temperature Profile 1

## 3.1 Materials

Commercially available PVDF (Kynar 741, from Arkema, with molecular weight of 282,000 g/mol) was used. Carbon dioxide ($CO_2$, from Linde Gas Inc.) of 99.8% purity was used as the physical blowing agent and/or the plasticizing medium of PVDF. Both PVDF and $CO_2$ were used as received without further modification. The supercritical $CO_2$ medium was obtained by injecting pressurized $CO_2$ gas into the PVDF polymer melt in the batch foaming chamber at an elevated temperature.

## 3.2 Film preparation

Weighed amounts of PVDF powder were loaded into a circular disc mold of 120mm in diameter and 500μm in thickness, and subsequently compression molded into film samples using literature, by the following procedures:

Step 1. Based on PVDF density, 10g of PVDF powder was filled into the circular disc mold. The mold was loaded into the compression molding machine (4386 CH, from Craver Press) pre-set at 185°C.

Step 2. The mold was equilibrated at the pre-set molding temperature.

Step 3. The material was compression-molded by applying 5,000, 10,000, and 15,000 lbs-

force for 30s at each pressure (i.e., a total of 90s).

Step 4. The molded sample was cooled to room temperature in the compression molding machine with the heater turned off and constant applied pressure.

The molded samples obtained without additional processing is denoted as the "as-molded PVDF sample" for the rest of the report.

## 3.3 Experimental Process

As-molded PVDF samples were loaded into a batch foaming chamber to undergo thermal and $ScCO_2$ processing (Figure 3.1). All samples were pre-cut into square-shaped samples of 0.5" × 0.5" before being processed. Figure 3.2 illustrates the three-stage temperature profile in the thermal and $ScCO_2$ processing method using temperature profile 1. A brief description of each stage is summarized in Table 3.1. Parametric studies were conducted to study the effects of various processing parameters of each stage on PVDF's crystalline structures. This aims to evaluate the optimal physical foaming condition of PVDF as well as the initial observation on the novel processing method's effect on PVDF's crystal structures. The processing conditions utilized in these parametric studies are summarized in Table 3.2.

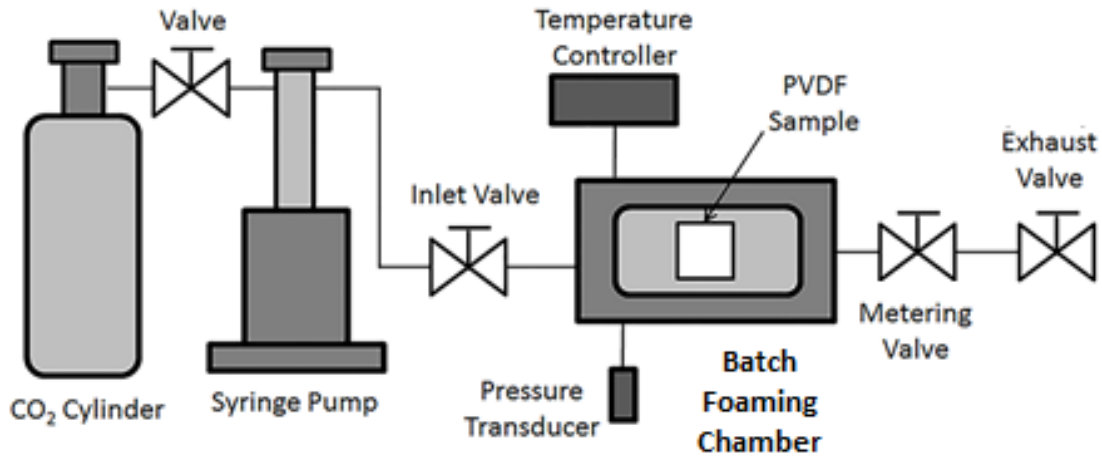


**Figure 3.1 Schematic illustration of the batch foaming system**

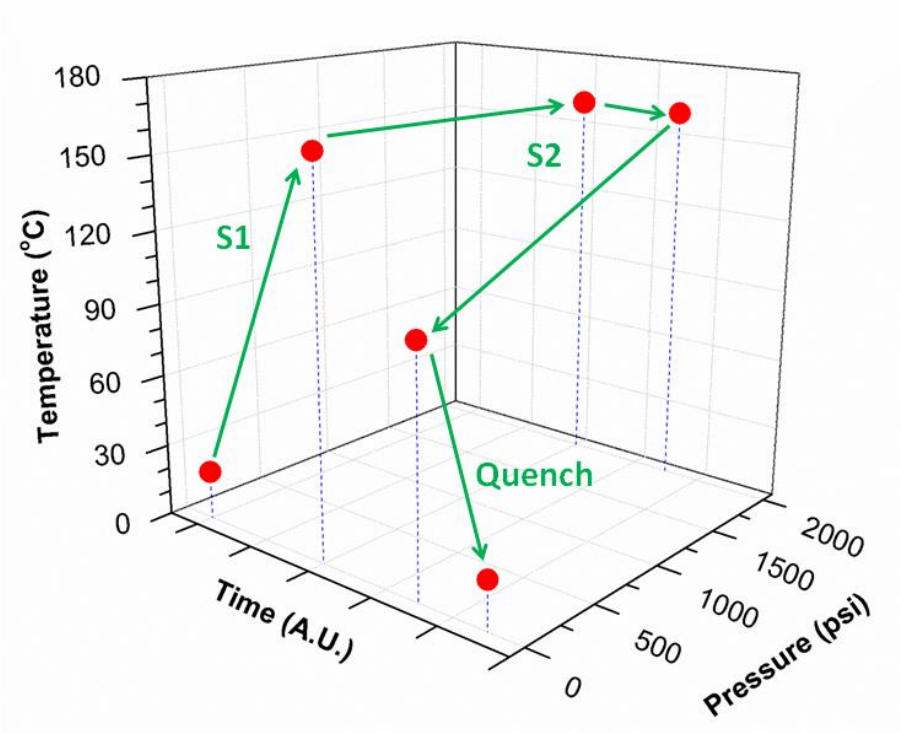


**Figure 3.2 General temperature profile used in the thermal and $ScCO_2$ processing of PVDF using temperature profile 1.**

**Table 3.1 Description of each stage in thermal and $ScCO_2$ processing of PVDF using temperature profile 1.**

| Stage | Description |
|---|---|
| S1 | The as-molded PVDF sample was heated to the saturation temperature ($T_{sat}$). |
| S2 | $ScCO_2$ was injected into the batch foaming chamber to saturate the PVDF sample at saturation pressure ($P_{sat}$) for 15 minutes. After time had elapsed, high pressure $ScCO_2$ was rapidly released from the chamber to initiate physical foaming of PVDF. The processed sample was removed from the foaming chamber and quenched in an ice bath to stabilize resultant microstructure. |

**Table 3.2 Experimental conditions for parametric studies using temperature profile 1**

| Processing Parameters | Value | Unit |
|---|---|---|
| Saturation Temperature ($T_{sat}$) | 100, 120, 140, 160, 180 | ℃ |
| Saturation Pressure ($P_{sat}$) | 1200, 2000, 2500 | psi |

From previous experiments it was found that 15 minutes was enough to saturate the PVDF sample with $ScCO_2$. For comparison purposes, some PVDF samples were processed without the presence of $ScCO_2$.

## 3.4 Characterization of PVDF

PVDF samples that underwent thermal and $ScCO_2$ processing with or without $ScCO_2$ were characterized by their morphology and crystal content using various equipment and standards.

### 3.4.1 Volume expansion ratio

The volume expansion of PVDF samples after $ScCO_2$ foaming was determined using ASTM D792 standard. After measuring its weight in air and in water, the volume expansion ratio (*VER*) can be determined by Equation (1).

$$VER = \frac{\rho \times (m_{air} - m_{water})}{m_{air} \times \rho_{water@T_w}} \quad (1)$$

Here $m_{air}$ and $m_{water}$ are the sample's weights measured in air and water, respectively, $T_w$ is the water temperature, $\rho_{water@Tw}$ is the density of water at $T_w$, and $\rho$ is the density of bulk PVDF (i.e., 1.780 g/cm$^3$).

### 3.4.2 Scanning electron microscopy (SEM)

The foam morphologies of PVDF samples were characterized by SEM (Quanta 3D FEG, from FEI Company). PVDF foam samples were cryo-fractured to expose their cross-sections and the fractured surfaces were sputter-coated with gold (Desk V Sputter, from Denton Vacuum) to make it conductive. For PVDF foam samples, the cell population density ($N_0$) with respect to the unprocessed volume was determined by Equation (2):

$$N_o = VER \times \left(\frac{n \times M^2}{A}\right)^{\frac{3}{2}} \quad (2)$$

Here *n* is the number of cells in the SEM micrograph, *M* is the magnification factor, and *A* is the area of the micrograph.

### 3.4.3 Differential scanning calorimetry (DSC)

DSC (Q20, from TA Instruments) was used to characterize the melting temperatures and the degree of crystallinity ($\chi_c$) of PVDF samples. This was done by analyzing the heat flow through the sample as a function of temperature. Thermal analyses were conducted from 40°C to 220°C at a ramping rate of 10°C/min. $\chi_c$ was calculated using Equation (3).

$$\chi_c = \frac{\Delta H_f}{\Delta H_{f,c}} * 100\% \quad (3)$$

Here $\Delta H_f$ is the heat of fusion of the PVDF sample and $\Delta H_{f,c}$ (i.e., 104.7 J/g) is the heat of fusion of 100% crystalline PVDF.

### 3.4.4 Fourier transform infrared spectroscopy (FTIR)

Infrared spectra of PVDF samples were obtained by a FTIR spectrometer (VERTEX 70/80, from Bruker) by averaging signals from 24 scans from 400 $cm^{-1}$ to 1500 $cm^{-1}$ at a resolution of 1 $cm^{-1}$. It had been common practice to denote the 763 $cm^{-1}$ band as the non-polar $\alpha$ phase and the 840 $cm^{-1}$ band as the $\beta$ phase [83]. However, some literature has denoted the 840 $cm^{-1}$ band as the $\gamma$ phase [59]. Due to the presence of common peaks that appear in multiple crystal phases during FTIR characterization, it has been a challenge to distinguish the PVDF polymorphs. To overcome this challenge, the peak-to-valley height ratio method reported by Cai *et al*. [84] was used to differentiate the three main polymorphs by extending the known absorbance bands of the crystal polymorph beyond the 700 – 900 $cm^{-1}$ range to use $\beta$ and $\gamma$ exclusive bands.

The peak-to-height valley ratio methods denoted the 763 $cm^{-1}$ band as the $\alpha$ phase and

the 840 $cm^{-1}$ band as the electroactive (*EA*) phase. If the $\beta$ band at 1275 $cm^{-1}$ was present but not the $\gamma$ band at 1234 $cm^{-1}$, the entire *EA* band at 840 $cm^{-1}$ would comprise entirely of the $\beta$ phase and Equation (4) would be used.

$$F_{EA} = \frac{A_{EA}}{1.26 \times A_{\alpha} + A_{EA}} \times 100\% \quad (4)$$

Here $F_{EA}$ is the fraction of electroactive crystal phase in PVDF's crystalline region, $A_{EA}$ and $A_{\alpha}$ are the absorbance bands of the electroactive and $\alpha$ phases, respectively. If both 1275 and 1234 $cm^{-1}$ bands existed, $F_{EA}$ would be subdivided into fractions of $\beta$ and $\gamma$ crystals. This could be done using Equations (5) and (6).

$$F_{\beta} = F_{EA} \times \left( \frac{\Delta H_{\beta}}{\Delta H_{\beta} + \Delta H_{\gamma}} \right) \times 100\% \quad (5)$$

$$F_{\gamma} = F_{EA} \times \left( \frac{\Delta H_{\gamma}}{\Delta H_{\beta} + \Delta H_{\gamma}} \right) \times 100\% \quad (6)$$

Here $F_{\beta}$ and $F_{\gamma}$ are the fraction of $\beta$ and $\gamma$ phases, respectively, $\Delta H_{\beta}$ and $\Delta H_{\gamma}$ are the height differences between the peak of 1275 $cm^{-1}$ and 1234 $cm^{-1}$ to their nearest valleys, respectively, as illustrated in Figure 3.3. By using the height to the nearest valley and not the absolute value, this more accurately represents the content of each polymorph. It is important to note that $F_{\beta}$ and $F_{\gamma}$ are the fraction of $\beta$ and $\gamma$ phases out of the crystalline region of the polymer. To obtain the total $\beta$ and $\gamma$ phase content in the entire polymer, $\chi_c$ would need to be taken into consideration.

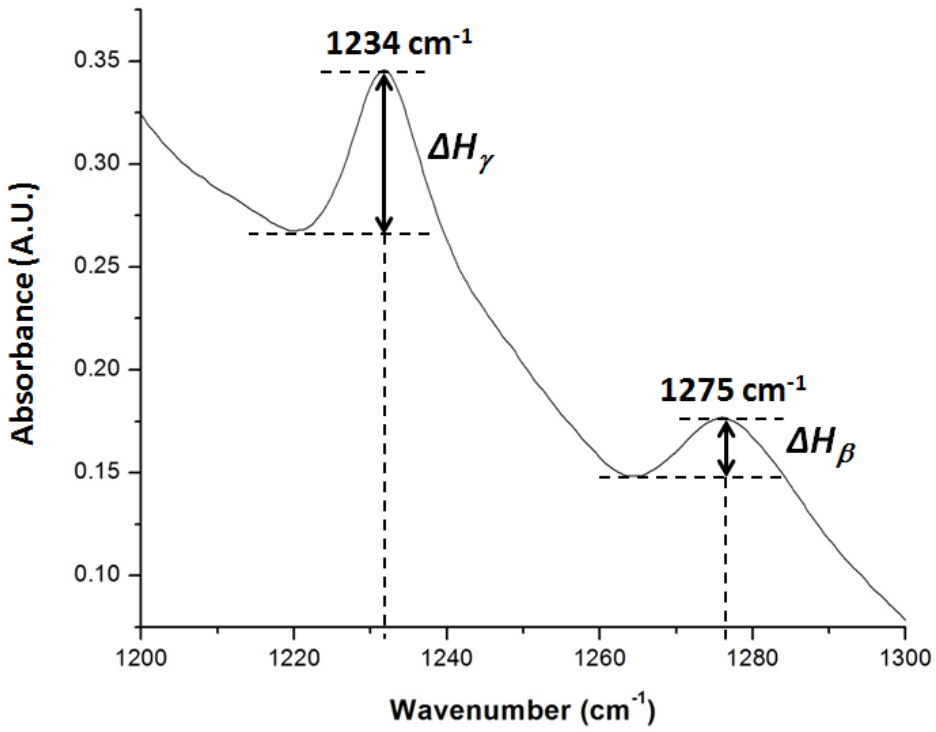


**Figure 3.3 Visual representation of $\Delta H_\beta$ and $\Delta H_\gamma$ for the peak-to-valley height ratio method**

### 3.4.5 X-Ray Diffractometer (XRD)

Diffraction peaks of PVDF were obtained using a XRD (Miniflex 600, from Rigaku) over a scan range from 10° to 30°, and a scan step of 0.02 at a speed of 2 s per step. Common $\alpha$ peaks were observed at 2θ = 18.4° and 19.9°, $\beta$ peak at 20.6°, and $\gamma$ peak at 20.3° [22]. XRD was used as an additional support for the peak-to-valley height ratio method in distinguishing PVDF polymorphs.

## 3.5 Effect of $ScCO_2$ processing using temperature profile 1 on foam morphology

The effect of the expansion of $CO_2$ gas leading to a volume expansion in PVDF was observed with varying $T_{sat}$ and $P_{sat}$. When pressurized $CO_2$ gas was released from the exhaust valve, the sudden pressure drop led to thermodynamic instability in the PVDF-$CO_2$ system and resulted in cellular structures within the PVDF matrix. From Figure 3.4 it can be observed that the saturation temperature ($T_{sat}$) of 160°C led to the highest volume expansion ratio (*VER*), regardless of saturation pressure ($P_{sat}$). When $T_{sat}$ was too low (i.e., ≤ 140°C), the PVDF matrix was too stiff to generate cellular structures. However, when $T_{sat}$ was too high (i.e., 180°C), the foam structure could not sustain, resulting in excessive gas loss and a decrease in *VER*. The optimal physical foaming was observed at 2000 psi and 160°C, resulting in a *VER* of 15.4. Using SEM, the $CO_2$ foam morphologies of PVDF samples processed at 2000 psi were observed (Figure 3.5). The morphology changed from solid polymer matrix (at 100°C and 140°C), to uniform cellular structure (at 160°C), and finally to collapsed foam structures with big voids and gas pockets (at 180°C). The foam morphologies corresponded with the *VER* obtained and this further supported the relationship between saturation temperature and the $CO_2$ cellular structure property in PVDF.

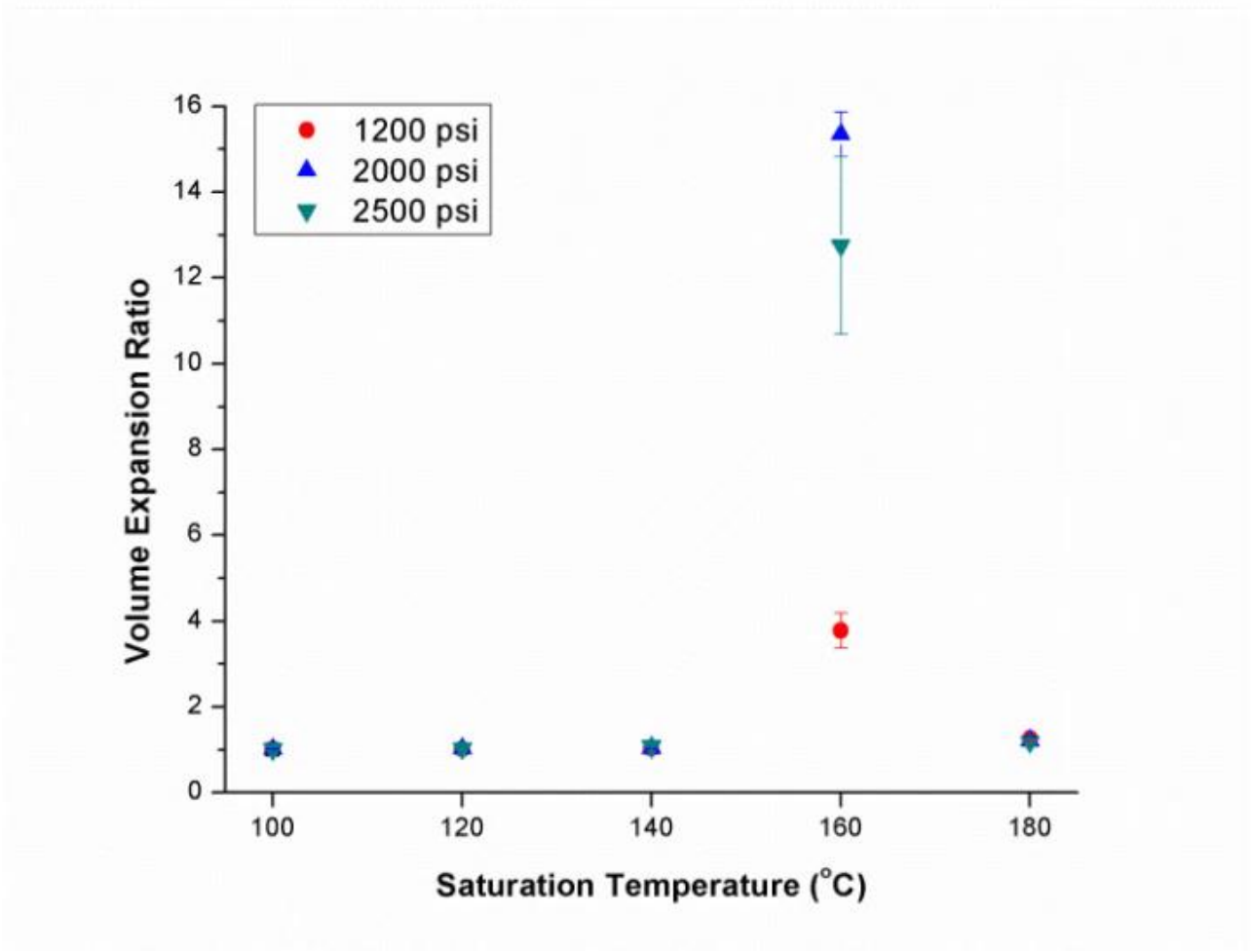


**Figure 3.4 Effect of $ScCO_2$ on the volume expansion ratio of PVDF prepared using temperature profile 1 at various saturation temperatures and saturation pressures**

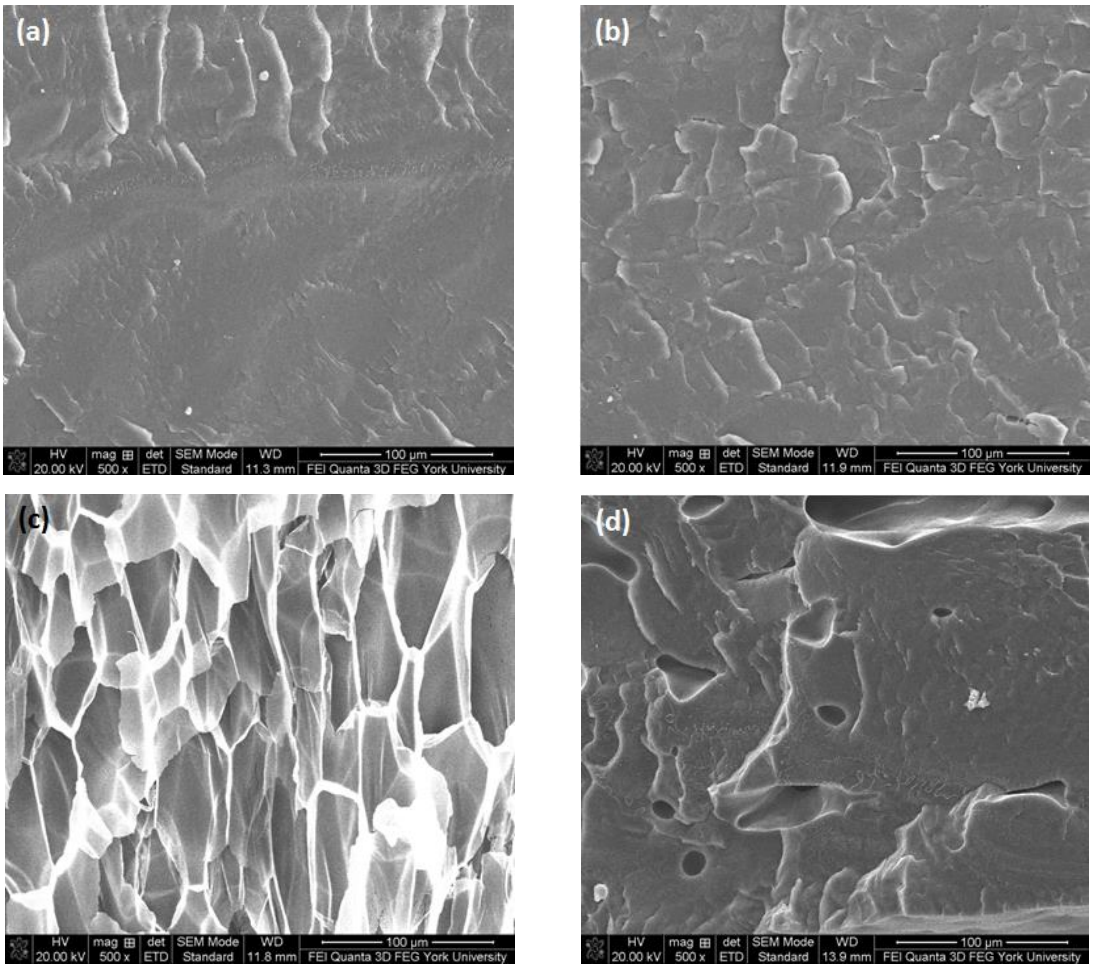


**Figure 3.5 SEM micrographs (at 500x magnification) of PVDF processed with $ScCO_2$ using temperature profile 1 at 2000 psi and various saturation temperatures: (a) 100°C; (b) 140°C; (c) 160°C; and (d) 180°C**

At $T_{sat}$ of 160°C, it was observed that an increase in saturation pressure, $P_{sat}$, from 1200 psi to 2000 psi resulted in an increase in *VER* (i.e., 3.8 to 15.4). $CO_2$ gas had an increased condensability with $P_{sat}$ increase, causing a more rapid sorption process and allowing an enhanced $CO_2$ induced plasticization effect. This resulted in an increase in chain group mobility, allowing more freedom, and bigger and more uniform bubble growth compared to that of the

lower $P_{sat}$ (Figure 3.6(a) and Figure 3.6(b)). However, when the $P_{sat}$ increased from 2000 psi to 2500 psi at $T_{sat}$ of 160°C, the *VER* decreased from 15.4 to 11.4. Such decrease in *VER* is evidenced by thin cell walls with multiple pin holes causing ruptures at 2500 psi (Figure 3.6(c)). The rupture of cell walls could be attributed to the significant plasticization effect induced by $ScCO_2$ and the rapid foam expansion at this high level of saturation pressure. $P_{sat}$ of 2500 psi was the maximum saturation pressure used due to safety limitation of the batch foaming system.

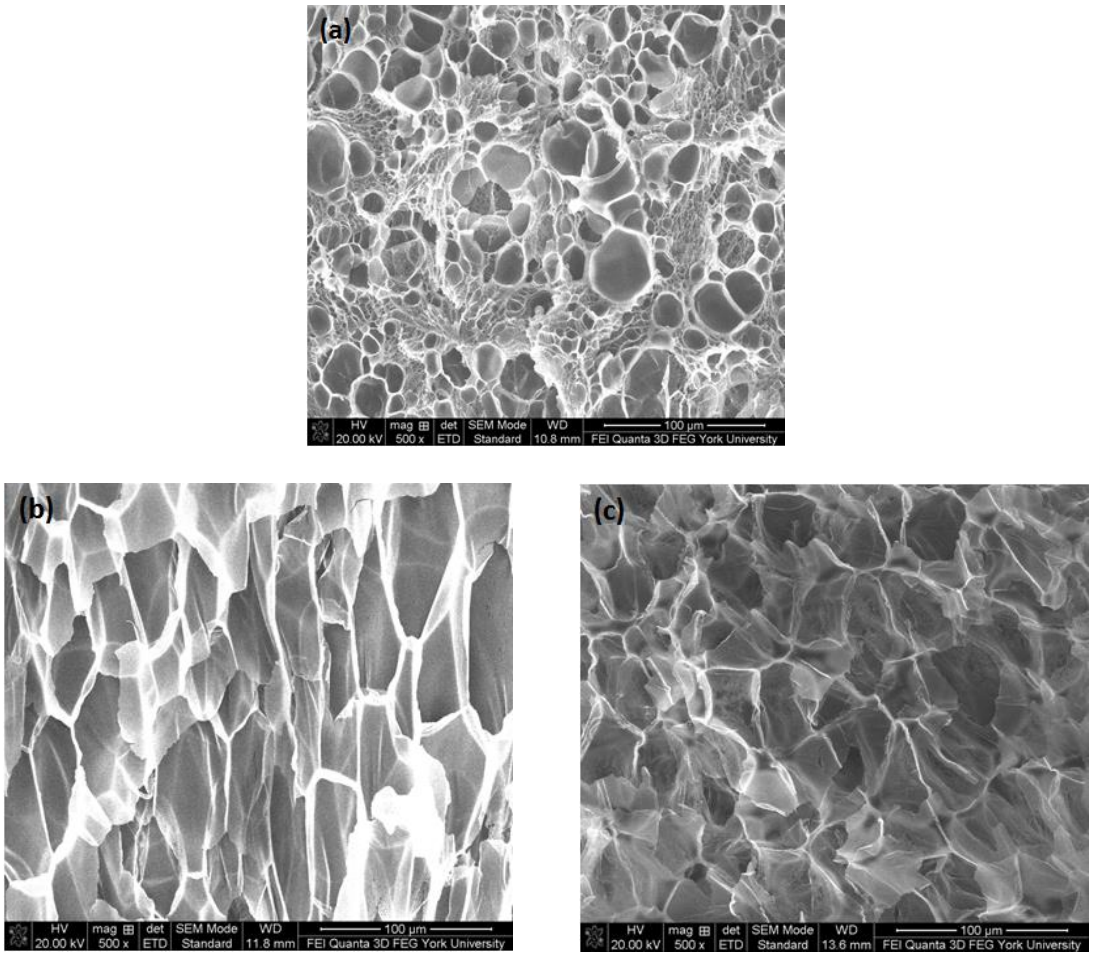


**Figure 3.6 SEM micrographs (500x magnification) of PVDF processed with $ScCO_2$ using temperature profile 1 at $T_{sat}$ of 160 °C and various saturation pressures: (a) 1200 psi; (b) 2000 psi; and (c) 2500 psi**

## 3.6 Effect of $ScCO_2$ processing using temperature profile 1 on the degree of crystallinity

From the previous section, it has been concluded that at the right condition, $CO_2$ bubbles are nucleated and are able to expand to effect PVDF morphology. This section will observe the presence of $ScCO_2$ and its expansion on PVDF's crystallinity. As seen from the thermogram of an as-molded PVDF sample (Figure 3.7), the onset of melting of PVDF's crystals is around 140°C. By 180°C, all the crystals have melted, corresponding with PVDF's melting temperature, $T_m$, of 168°C. This melting of crystals can also be seen in the degree of crystallinity, $\chi_c$, of the processed samples, regardless of saturation pressure (Figure 3.8). Above a saturation temperature of 140°C, crystals starts to melt and $\chi_c$ decreases below the as-molded sample's $\chi_c$ of 51%.

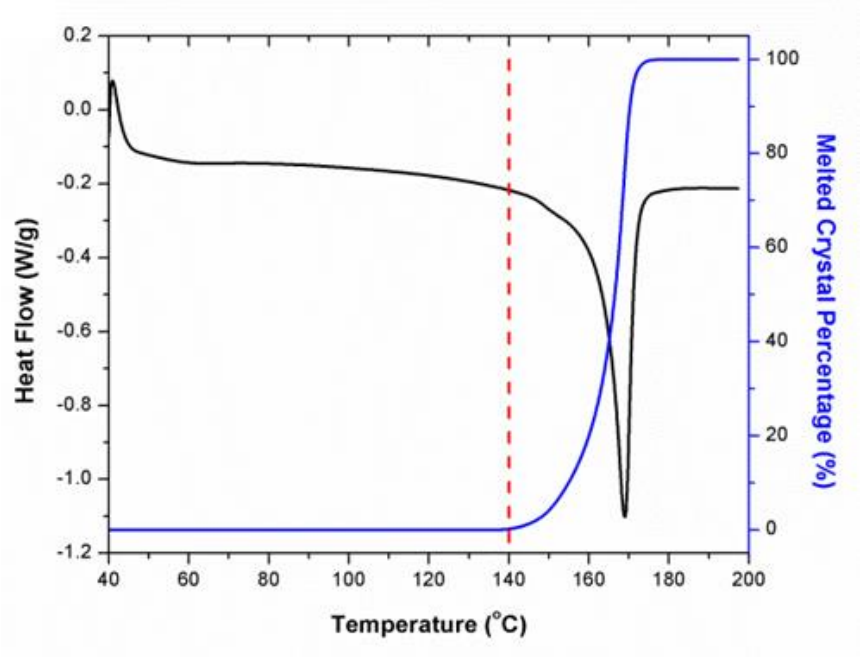


**Figure 3.7 Melted crystal percentage and thermogram for as-molded PVDF sample**

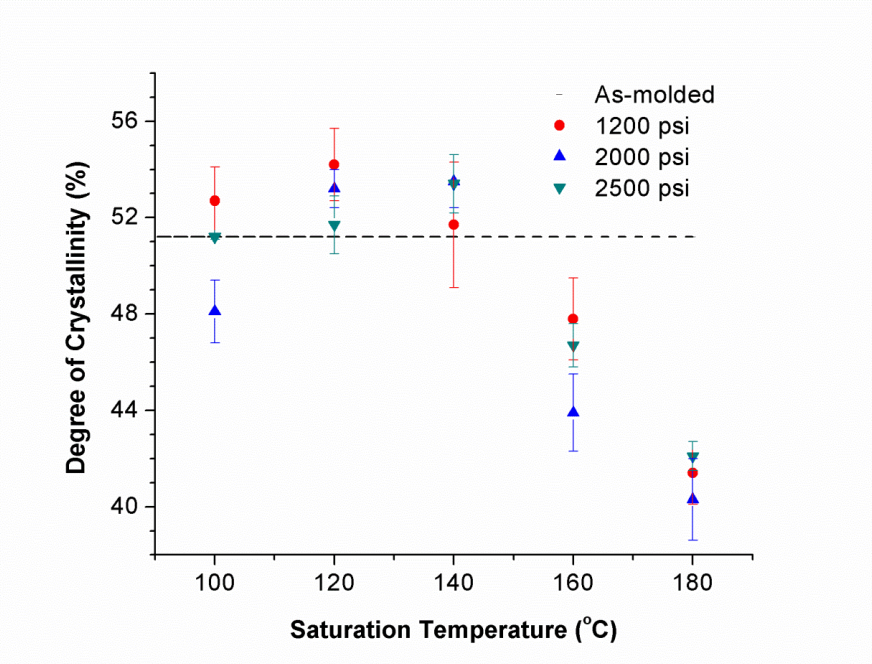


**Figure 3.8 Comparison of the effect of $ScCO_2$ using temperature profile 1 on the degree of crystallinity of PVDF samples at various saturation temperatures and pressures.**

At $T_{sat}$ of 140°C and below, there is little or no melting of crystals. Therefore, the pre-existing crystals in the PVDF matrix were used as seeds for crystal growth. When PVDF samples were subjected to a $ScCO_2$ environment, the plasticization effect from $ScCO_2$ increased PVDF's molecular chain mobility and decreased its melting temperature. An optimal level of plasticizing effect enhanced the chain mobility around the pre-existing crystal nuclei and thereby promoted crystal perfection during gas saturation. This combined with the annealing effect on the pre-existing crystals increased the $\chi_c$, as evidenced by the $\chi_c$ peaks in the 120°C to 140°C $T_{sat}$ region (Figure 3.8). However, when $T_{sat}$ increased to 160°C, the onset of melting (i.e., 140°C) and the suppression of the melting point by $ScCO_2$ plasticizing effect disrupted the pre-existing crystal

structure. This led to a scarce number of seeds for crystal perfection despite the high mobility of PVDF's molecular chain groups. Moreover, the fast $CO_2$ consumption during the physical foaming process rapidly increased the melting temperature back to its original temperature. This did not allow sufficient time for the crystals to grow. As a result, the degree of crystallinity decreased despite the high volume expansion ratio observed at 160°C. Each saturation pressure achieved a maximum degree of crystallinity of approximately 54% at their own distinct saturation temperatures.

At the same saturation temperature but lower saturation pressure, there is a lower degree of plasticization effect. This resulted in a larger amount of existing crystals prior to physical foaming, hindering PVDF's foamability. This was also supported by the non-uniform cell structure and thick cell walls at this low $P_{sat}$, previously seen in Figure 3.6(a). As $P_{sat}$ increased from 1200 psi to 2000 psi at a steady $T_{sat}$ of 160 °C, $\chi_c$ decreased from 48% to 44%. This was due to the higher degree of plasticization effect and high foamability, which reduced the amount of crystals but yielded uniform cell structures as previously observed in the SEM from Figure 3.6(b).

## 3.7 Effect of $ScCO_2$ processing using temperature profile 1 on the electroactive phases

FTIR analysis was conducted for PVDF samples processed using temperature profile 1 with and without the presence of $ScCO_2$ to observe its effect on the distinct three main polymorphs (i.e., $\alpha$, $\beta$, and $\gamma$). With this analysis, the presence and change in the content of the three main

polymorphs can be individually qualified. Figure 3.9 shows the FTIR absorbance curves for the as-molded PVDF sample as well as samples processed at $T_{sat}$ of 160°C, and without and with $ScCO_2$. Peaks at wavenumbers 763 $cm^{-1}$, 840 $cm^{-1}$, and 1275 $cm^{-1}$ are present in all three FTIR spectra but there is no peak at 1234 $cm^{-1}$. This indicates that only $\alpha$ and $\beta$ phases were present, and thereby the $F_{EA}$ peak at 840 $cm^{-1}$ consisted entirely of $\beta$ crystals. It can also be observed that the *EA* phase peak at 840 $cm^{-1}$ increased when processed at $T_{sat}$ of 160°C, and even more when it was subjected to a $ScCO_2$ environment at 2000 psi. The $\beta$ phase peak at 1275 $cm^{-1}$ is also the most pronounced at this condition, thereby indicating a growth in $\beta$ crystals due to $ScCO_2$.

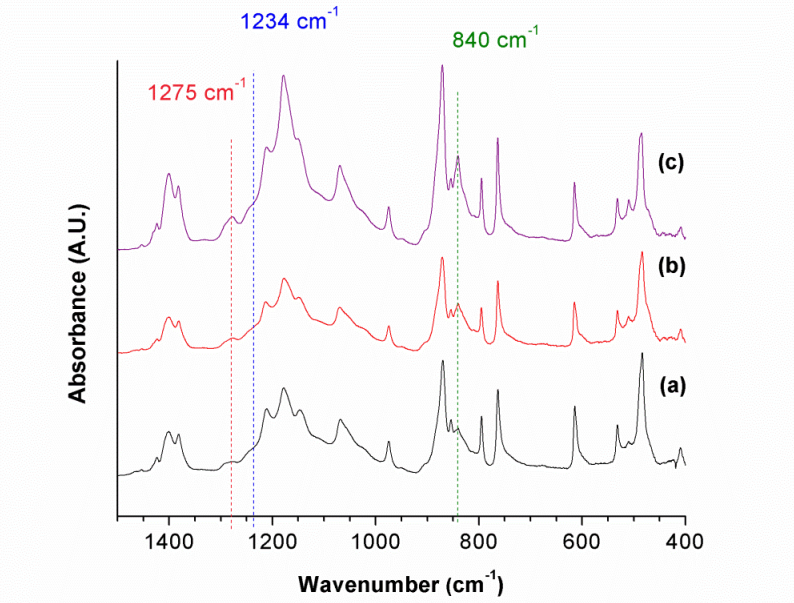


**Figure 3.9 FTIR absorbance graph of PVDF: (a) as-molded sample; processed sample using temperature profile 1 at $T_{sat}$ = 160°C and (b) without $ScCO_2$; and (c) $P_{sat}$ = 2000 psi**

At $P_{sat}$ of 2000 psi and various saturation temperature (i.e., 140°C, 160°C, and 180°C), there is again no peak at 1234 $cm^{-1}$ present, indicating that there are no $\gamma$ phase, and $F_{EA}$ peak at

840 $cm^{-1}$ equaled to $F_\beta$ (Figure 3.10). $T_{sat}$ of 160°C had the most prominent 840 $cm^{-1}$ and 1275 $cm^{-1}$ peak, which was also the condition with the highest *VER*. The increase in $\beta$ phase peak at the highest *VER* could deduce that the formation of $\beta$ phase is related to the foaming induced strain during the rapid depressurization of the foaming chamber. The peaks at 763 $cm^{-1}$, 840 $cm^{-1}$, and 1275 $cm^{-1}$ seemed to be less pronounced at $T_{sat}$ of 180°C, the condition where there was significant melting of crystals and the lowest $\chi_c$. As $T_{sat}$ increased beyond PVDF's melting temperature of 168°C, the crystalline structure transformed to the unorderly amorphous phase due to the excessive chain group mobility. As the quantity of the distinct polymorphs decreased, so did the overall degree of crystallinity, the same trend observed in Figure 3.8.

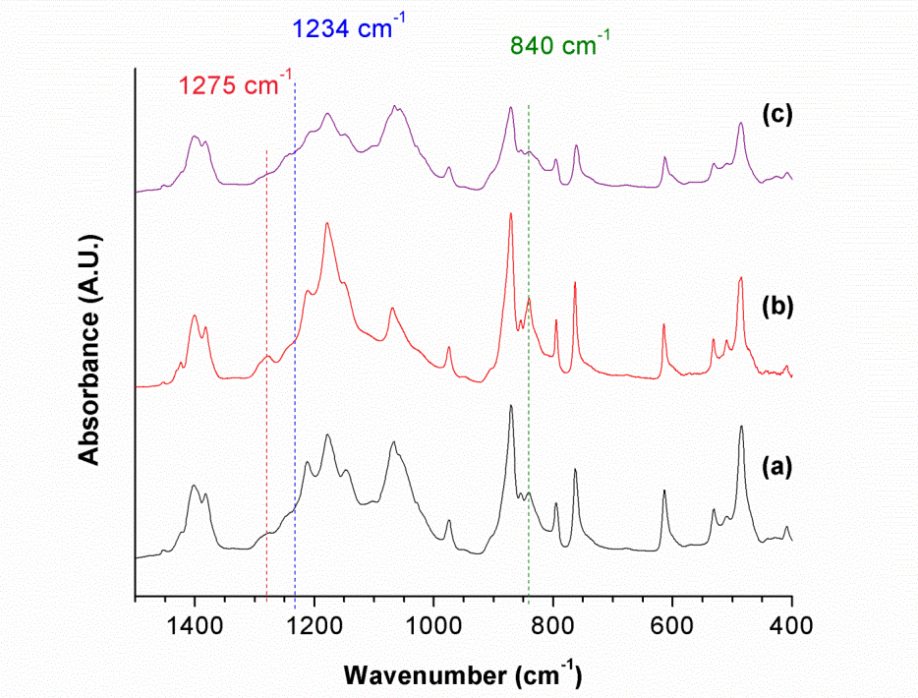


**Figure 3.10 FTIR absorbance graph of PVDF processed with $ScCO_2$ using temperature profile 1 at $P_{sat}$ = 2000 psi and $T_{sat}$ of (b) 140°C; (c) 160°C; and (d) 180°C**

# Chapter 4 Thermal and $ScCO_2$ Processing of PVDF – Temperature Profile 2

Temperature profile 1 provided the optimal physical foaming condition of PVDF at $P_{sat}$ of 2000 psi and $T_{sat}$ of 160°C, resulting in a *VER* of 15.4. It also provided the initial evidence towards foaming induced strain causing an increase in $\beta$ crystals, as observed by the FTIR absorbance curves. Temperature profile 2 took this optimal condition into consideration and added an additional heating step, which heated the PVDF sample to an elevated heating temperature beyond its melting temperature before the injection of $ScCO_2$.

To elucidate the effect of bubble growth-induced strain on the formation of PVDF's electroactive phases and to explore the potential of $ScCO_2$ processing to tailor PVDF's crystalline structures, the saturation temperature and saturation pressure for the base case of samples prepared under temperature profile 2 were kept at 160°C and 2000 psi, respectively.

## 4.1 Experimental Process

The same PVDF and $CO_2$ gas from temperature profile 1 was used, as well as the fabrication of the as-molded PVDF samples of 500μm thickness. Figure 4.1 illustrates the five phase temperature profile used in the temperature profile 2 of the thermal and $ScCO_2$ processing method. A brief description of each phase is summarized in Table 4.1.

The evolution of crystal polymorphs in PVDF after each processing step were studied to elucidate the multi-stage crystallization mechanism. To decouple the effect of each phase on

PVDF's crystallization behaviors, PVDF samples were taken out of the chamber after the completion of each phase and quenched in an ice bath to stabilize their microstructures. Furthermore, parametric studies were conducted to study the effects of the main processing parameters in each phase on PVDF's crystalline structures. This aimed to evaluate the processing-to-structure relationships of PVDF in each processing phase and to provide insights in the promotion of PVDF's electroactive crystal phase content. The processing conditions utilized in these parametric studies are summarized in Table 4.2 with the base case processing conditions bolded. The degree of crystallinity, $\chi_c$, and the fraction of $\alpha$, $\beta$, and $\gamma$ polymorphs in each sample were analyzed by DSC and FTIR, respectively.

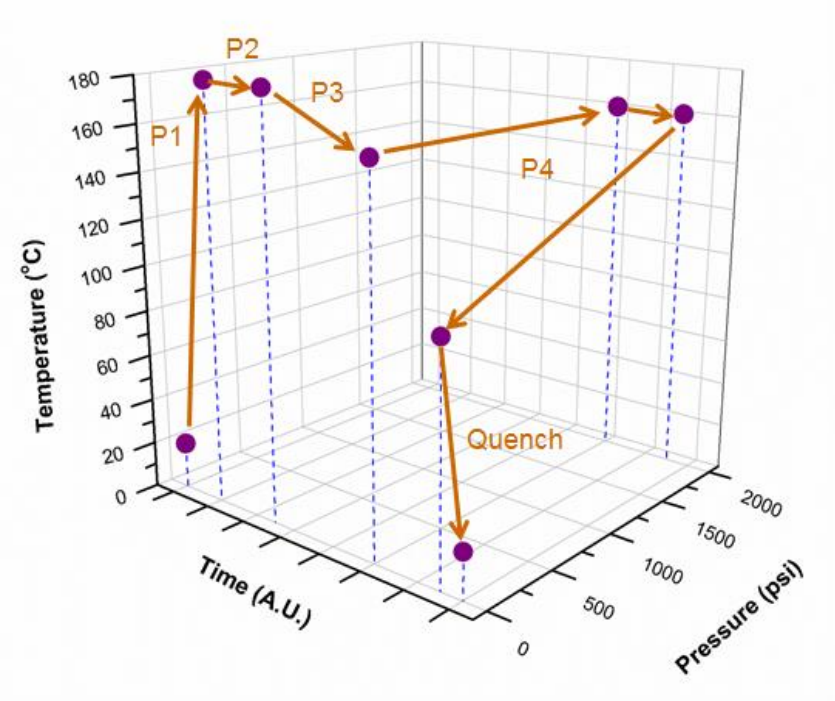


**Figure 4.1 The general temperature profile used in the thermal and $ScCO_2$ processing of PVDF using temperature profile 2**

**Table 4.1 Description of each phase in thermal and $ScCO_2$ processing of PVDF using temperature profile 2**

| **Phase** | **Description** |
|---|---|
| P1 | The as-molded PVDF sample was heated to the heating temperature ($T_H$). (***Crystal melting***) |
| P2 | The heated sample was held at $T_H$ for a holding time ($t_{hold}$). (***Isothermal crystallization***) |
| P3 | The temperature was slowly lowered to the saturation temperature ($T_{sat}$) for the $ScCO_2$ processing. (***Non-isothermal crystallization***) |
| P4 | $ScCO_2$ was injected into the batch foaming chamber to saturate the PVDF sample at the saturation pressure ($P_{sat}$) for 15 minutes. After time had elapsed, high pressure $ScCO_2$ was rapidly released from the foaming chamber at a certain pressure drop rate, *-dP/dt*, to initiate physical foaming of PVDF. The processed sample was removed from the foaming chamber and quenched in an ice bath. (***$ScCO_2$ foaming***) |

**Table 4.2 Experimental conditions for parametric studies using temperature profile 2**

| **Processing parameters** | **Values** | **Units** |
|---|---|---|
| Heating Temperature, $T_H$ | 170, **180**, 190, 200 | °C |
| Holding Time, $t_{hold}$ | **0**, 15, 45, 120, 300, 1440 | min |
| Saturation Temperature, $T_{sat}$ | 120, 140, **160** | °C |
| Saturation Pressure, $P_{sat}$ | 1200, **2000**, 2500 | psi |
| Pressure drop rate, *-dP/dt* | 48, 55, 123, 164, **191** | MPa/s |

## 4.2 Effect of each phase on the crystallinity and crystal phases of PVDF

By quenching the sample after each phase, the main effect of each phase and its specific parameters on PVDF's crystallinity and crystal structure can be distinguished. Figure 4.2 plots the total $\chi_c$ and $\alpha$, $\beta$, and $\gamma$ phase content in the processed PVDF samples after each of the five processing phases. Temperature profile 2 introduces the other electroactive phase, $\gamma$ phase, that was absent when utilizing temperature profile 1. With the presence of both $\beta$ and $\gamma$ phases, the peak-to-valley height ratio method was used to separate the content of the electroactive phase into $F_\beta$ and $F_\gamma$. Each processing phase was concluded by quenching the sample in ice water to stabilize its microstructure. Therefore, the effect of this unavoidable step was observed in each phase analysis and was considered when elucidating the results obtained.

The as-molded PVDF sample only contained $\alpha$ and $\beta$ crystals (Figure 4.2). After phase P1, $\chi_c$ of the quenched PVDF sample decreased from 52% to 43%, and $\beta$ crystal content increased moderately. In addition to the melting of crystals during heating, the rapid cooling induced by the ice bath during the quenching process provided a shorter timespan for crystallization, lowering its $\chi_c$. Furthermore, the low temperature environment and rapid cooling favored the nucleation of $\beta$ crystals, causing the moderate increase in $\beta$ phase content [34] [35].

In phase P2, the sample underwent isothermal crystallization at $T_H$ for a preset period (i.e., $t_{hold}$ = 300 min). The long $t_{hold}$ at high temperature caused a direct $\alpha$ to $\gamma$ transformation, following what was observed previously in literature [59]. This led to the introduction of $\gamma'$ phase, which has a higher melting temperature than the typical $\gamma$ phase but is an electroactive

phase nonetheless [7]. During phase P3, the sample underwent non-isothermal crystallization as the temperature was slowly dropped from $T_H$ (i.e., 180°C) to $T_{sat}$ (i.e., 160°C). This process significantly increased the $\gamma$ phase content, which was initiated at pre-existing $\alpha$ nuclei [56].

In phase P4, PVDF underwent a second stage of isothermal crystallization with or without the presence of $ScCO_2$ at 2000 psi for 15 minutes. Without $ScCO_2$ (i.e., Figure 4.2(e)), $\gamma$ phase content slightly increased due to the isothermal crystallization around the pre-existing $\alpha$ crystals. The annealing of $\alpha$ phase in the vicinity of its melting point and the vibrational energy of the crystals induced conformation fluctuation and preferentially stabilized in the $\gamma$ phase [7]. With $ScCO_2$ (i.e., Figure 4.2(f)), the induced plasticization effect promoted PVDF's chain mobility and suppressed its melting temperature. This potentially led to partial melting of $\gamma$ polymorph formed in the previous phase. Furthermore, the foam expansion and fast cooling from the rapid pressure drop during $ScCO_2$ release favored $\alpha$ to $\beta$ phase transformation and $\beta$ phase crystallization, respectively, increasing $\beta$ phase content.

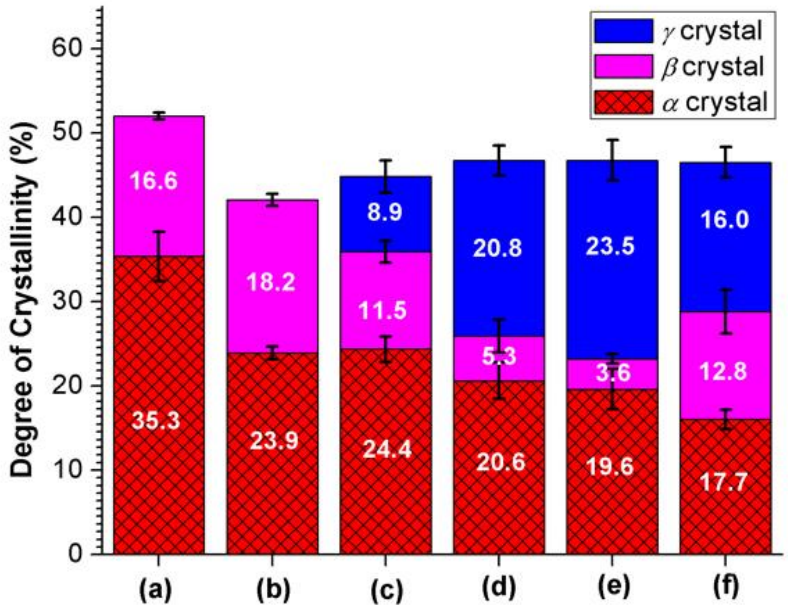


**Figure 4.2 Degree of crystallinity with respect to $\alpha$, $\beta$, and $\gamma$ polymorphs in processed PVDF samples after each phase: (a) as-molded PVDF; (b) after P1; (c) after P2; (d) after P3; (e) after P4 without $ScCO_2$; (f) after P4 with $ScCO_2$. [Processing conditions: $T_H$ = 180°C, $t_{hold}$ = 300 mins, $T_{sat}$ = 160°C, and $P_{sat}$ = 2000 psi].**

## 4.3 Effect of heating temperature ($T_H$) on the electroactive phase content (P1)

The effect of $T_H$ on PVDF's crystallization behaviours were observed by heating PVDF samples to different $T_H$ in phase P1, and then processed using the base case conditions in the rest of the processing phases. Figure 4.3 plots the fractions of $\beta$ and $\gamma$ crystal phases in the processed PVDF samples calculated by the peak-to-valley height ratio method. It can be observed that the $\gamma$ crystal phase content increased as $T_H$ was raised from 170°C to 180°C. However, when PVDF was

heated to above 180°C, it did not possess any $\gamma$ phase. $\alpha$ crystal's melting temperature ranges from 167°C to 172°C. Literature review suggested that the presence of $\alpha$ crystal seeds facilitated $\gamma$ crystal nucleation from the melt [51]. When $T_H$ was too high, the majority of $\alpha$ crystals melted, leaving an insufficient amount of $\alpha$ nuclei to initiate $\gamma$ phase nucleation.

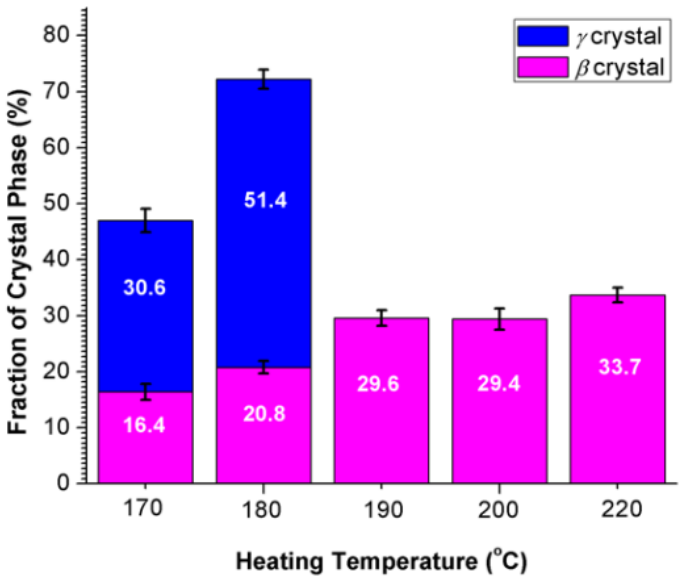


**Figure 4.3 Effect of $T_H$ on the fraction of $\beta$ and $\gamma$ crystal phases. [Processing conditions: $t_{hold}$ = 0 min, $T_{sat}$ = 160°C, $P_{sat}$ = 2000 psi, $-dP/dt$ = 191 MPa/s].**

In addition to FTIR, XRD and DSC analysis were used to confirm the FTIR results. XRD diffraction was conducted for PVDF processed using $T_H$ of 180°C and 200°C (Figure 4.4). The electroactive $\beta$ and $\gamma$ phases have bordering peaks at 20.6° and 20.3°, respectively. Due to their close proximity, this peak has been denoted as the electroactive (EA) phase. This peak is the most pronounced when $T_H$ is 180°C, which has the highest $F_{EA}$ of 72%. $T_H$ of 200°C has a much

lower $F_{EA}$ of 30%, meaning there is a greater content of $\alpha$ crystals (i.e., 70%). Accordingly, this condition has very strong peaks at 18.4° and 19.9°, both characteristics of the $\alpha$ phase. This qualitative XRD analysis provides additional evidence and supports the use of FTIR as the main analysis for the characterization of PVDF's polymorphs.

The DSC thermograms shown in Figure 4.5 further support this observation and have been previously used as complimentary analysis technique to the FTIR in characterizing polymorphs [7]. The $\gamma$ melting peak at 180°C was absent as $T_H$ reached 190°C and above. Instead, the melting peak with a shoulder at 167°C (i.e., $\beta$ crystal melting peak) became sharper, agreeing with the positive relationship between $T_H$ and $\beta$ content revealed by FTIR analysis. Therefore, it can be suggested that the absence of $\gamma$ crystals enhanced $\beta$ crystal nucleation. As $T_H$ increased from 180°C to 190°C, the $\beta$ crystal content increased by 10%, along with the disappearance of $\gamma$ crystals. Due to the tight conformation of $\gamma$ crystals, its presence restricted the dissolution of $ScCO_2$ into the PVDF matrix, and thereby suppressed the volume expansion ratio of PVDF samples during bubble expansion.

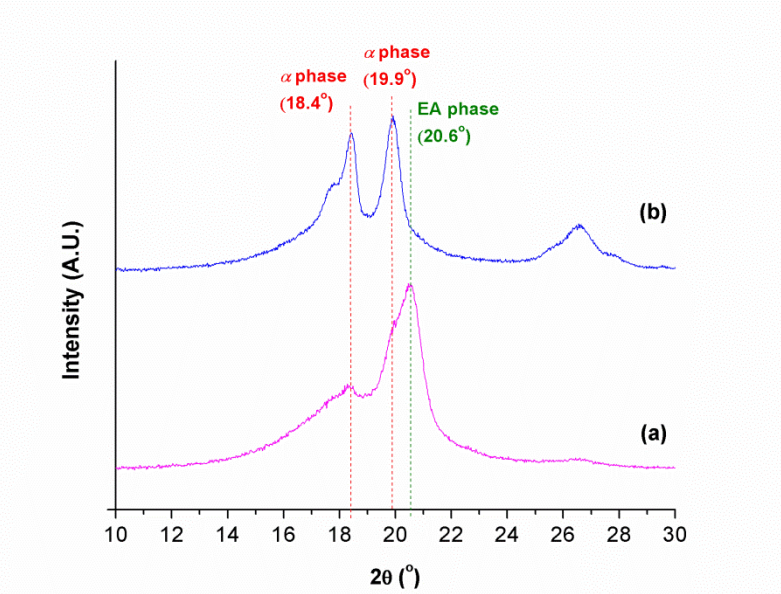


**Figure 4.4 XRD diffraction peaks of PVDF using temperature profile 2 at $T_H$ of: (a) 180°C; (b) 200°C. [Processing conditions: $t_{hold}$ = 0 min, $T_{sat}$ = 160°C, $P_{sat}$ = 2000 psi, $-dP/dt$ = 191 MPa/s].**

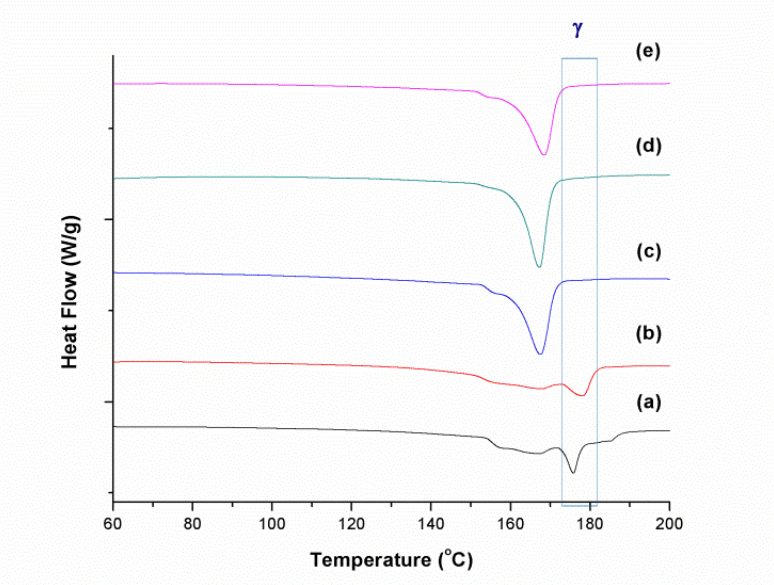


**Figure 4.5 DSC thermograms of PVDF processed at different $T_H$: (a) 170°C; (b) 180°C; (c) 190°C; (d) 200°C; (e) 220°C. [Processing conditions: $t_{hold}$ = 0 min, $T_{sat}$ = 160°C, $P_{sat}$ = 2000 psi, $-dP/dt$ = 191 MPa/s].**

As $T_H$ increased from 170°C to 200°C, the *VER* steadily increased from 3.3 to 12.0, along with their $\beta$ content (16.4% to 29.4%). It is interesting to note that although increasing $T_H$ to 220°C yielded the highest $\beta$ content (i.e., 33.7%), its *VER* decreased to 5.6. This was caused by the excessive gas loss to the surrounding at high saturation temperature. SEM micrographs in Figure 4.6(a) and Figure 4.6(b) indicated that although large uniform cells are omnipresent, evidence of cell ruptures were observed with a higher magnification, causing the *VER* decrease. Nevertheless, the initial expansion of the individual cells, evidenced by the large cell sizes and thin cell walls, promoted $\alpha$ to $\beta$ phase transformation and increased the $\beta$ phase content at $T_H$ of 220°C to a maximum of 33.7%.

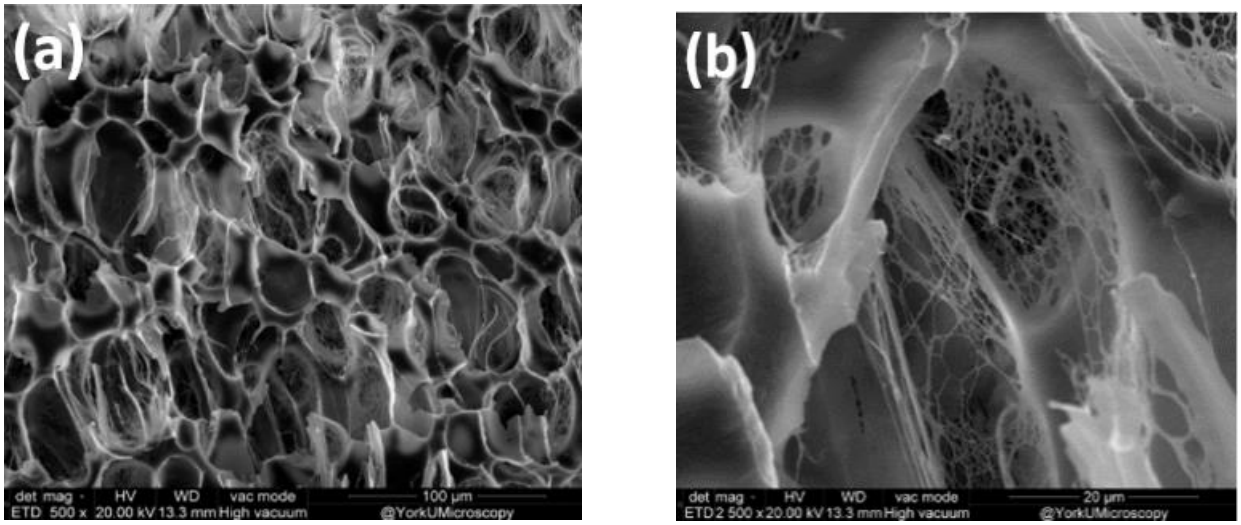


**Figure 4.6 SEM micrographs of processed PVDF samples at different magnifications: (a) 500x; and (b) 2500x. [Processing conditions: $T_H$ = 220°C, $t_{hold}$ = 0 min, $T_{sat}$ = 160°C, $P_{sat}$ = 2000 psi, $-dP/dt$ = 191 MPa/s].**

## 4.4 Effect of isothermal crystallization time ($t_{hold}$) on the electroactive phase content (P2)

The effect of holding time ($t_{hold}$) during phase P2 (i.e., after PVDF had been heated to $T_H$) on the resultant electroactive phases of PVDF were studied parametrically. When PVDF samples were quenched just after the completion of phase P2 (i.e., raise temperature to $T_H$, hold for $t_{hold}$, and then quench in ice water), the appearance of $\gamma$ crystals were observed when $t_{hold}$ was increased to 300 minutes (Figure 4.7). Following literature, the prolonged isothermal crystallization at a high temperature in phase P2 induced a direct $\alpha$ to $\gamma$ transformation, introducing the $\gamma'$ phase [59].

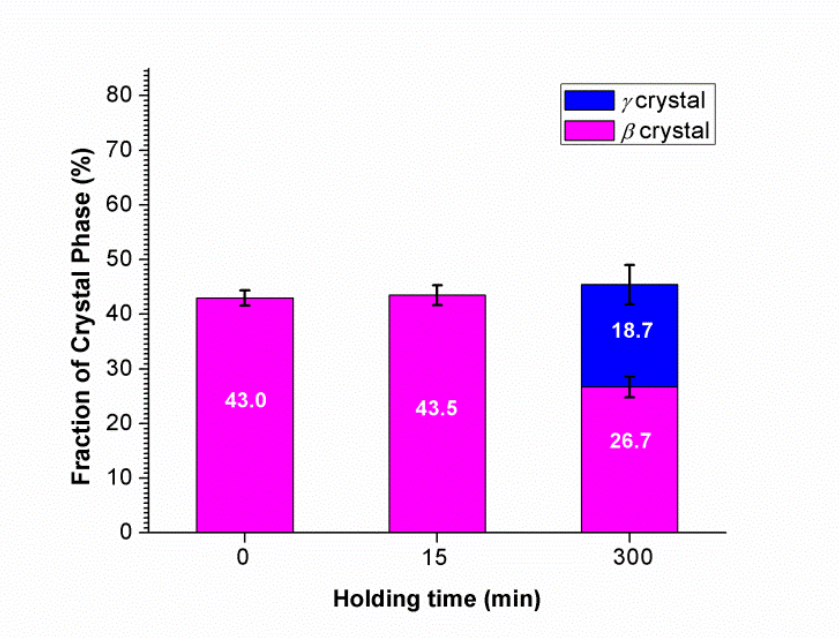


**Figure 4.7 Effect of $t_{hold}$ at $T_H$ of 180°C on the fraction of $\beta$ and $\gamma$ crystal phases. Processing was completed up until phase P2 and then the PVDF samples were quenched in an ice bath.**

To elucidate how the presence of $\gamma'$ crystals influenced the remaining processing phases

(i.e., P3 and P4), PVDF samples that had undergone isothermal crystallization at 180 °C for various $t_{hold}$, ranging from 0 minute to 1440 minutes (i.e., 24 hours), were subjected to the rest of the processing phases using the base case conditions. DSC thermograms clearly showed an increase in the melting peak at 190°C, which represented the more thermally stable $\gamma'$ phase, as $t_{hold}$ increased to 1440 minutes (Figure 4.8) [56]. This $\gamma'$ phase has a melting peak higher than the typical $\gamma$ phase due to its stability from forming over a longer period of time.

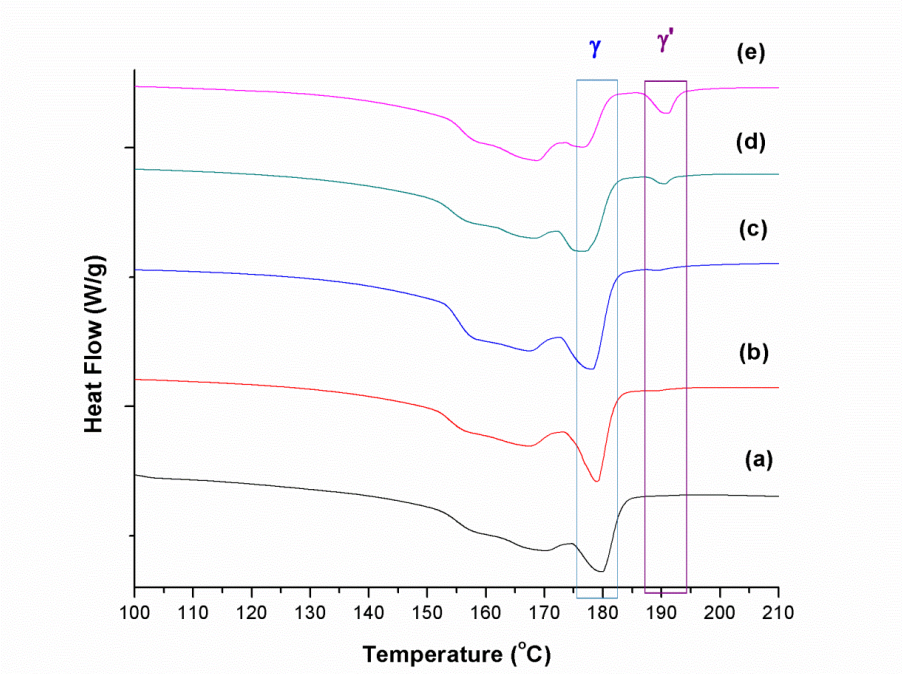


**Figure 4.8 DSC thermograms of PVDF samples processed with different $t_{hold}$: (a) 15 min; (b) 45 min; (c)120 min; (d) 300 min; (e) 1440 min. [Processing conditions: $T_H$ = 180°C, $T_{sat}$ = 160°C, $P_{sat}$ = 2000 psi, $-dP/dt$ = 191 MPa/s].**

Figure 4.9 plots $\chi_c$ with respect to the $\alpha$, $\beta$, and $\gamma$ polymorphs in PVDF. Experimental results reveal that despite the introduction of $\gamma'$ crystals from the long $t_{hold}$ at $T_H$ during phase P2,

increasing $t_{hold}$ decreased the final overall $\gamma$ phase content while increasing the $\alpha$ phase content. It is believed the direct $\alpha$ to $\gamma$ transformation during the long $t_{hold}$ exhausted the $\alpha$ crystal nuclei that were essential to the formation of $\gamma$ crystal phase during phase P3 (i.e., non-isothermal crystallization). Furthermore, the slow cooling during P3's non-isothermal crystallization from $T_H$ to $T_{sat}$ enhanced the nucleation of $\alpha$ polymorphs from the melt, increasing its content. The content of $\beta$ polymorph was independent of $t_{hold}$ and held steady around 11%, with its *VER* ranging from 4.3 to 4.9. This can be attributed to the virtually invariant foaming behaviour where the cell sizes of samples with $t_{hold}$ of 0 and 1440 min were 7.9 and 7.5 μm, respectively (Figure 4.10).

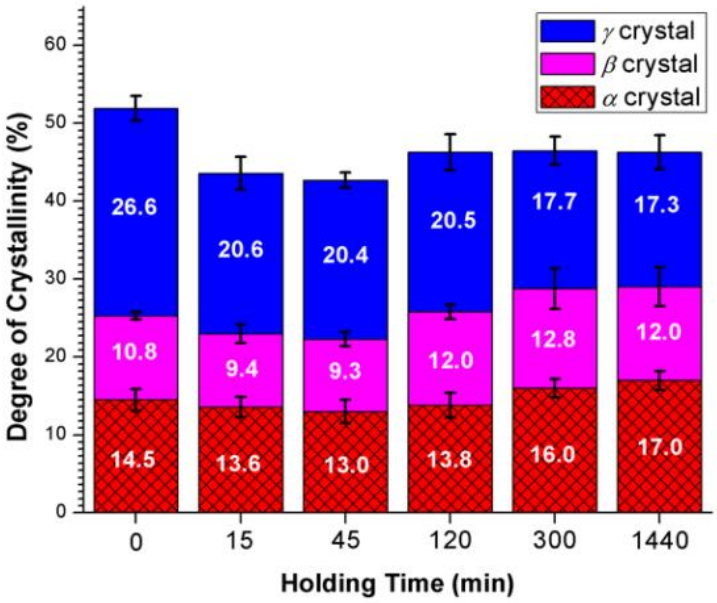


**Figure 4.9 Effect of $t_{hold}$ on the degree of crystallinity with respect to $\alpha$, $\beta$, and $\gamma$ polymorphs in processed PVDF. [Processing conditions: $T_H$ = 180°C, $T_{sat}$ = 160°C, $P_{sat}$ = 2000 psi, and $-dP/dt$ = 191 MPa/s].**

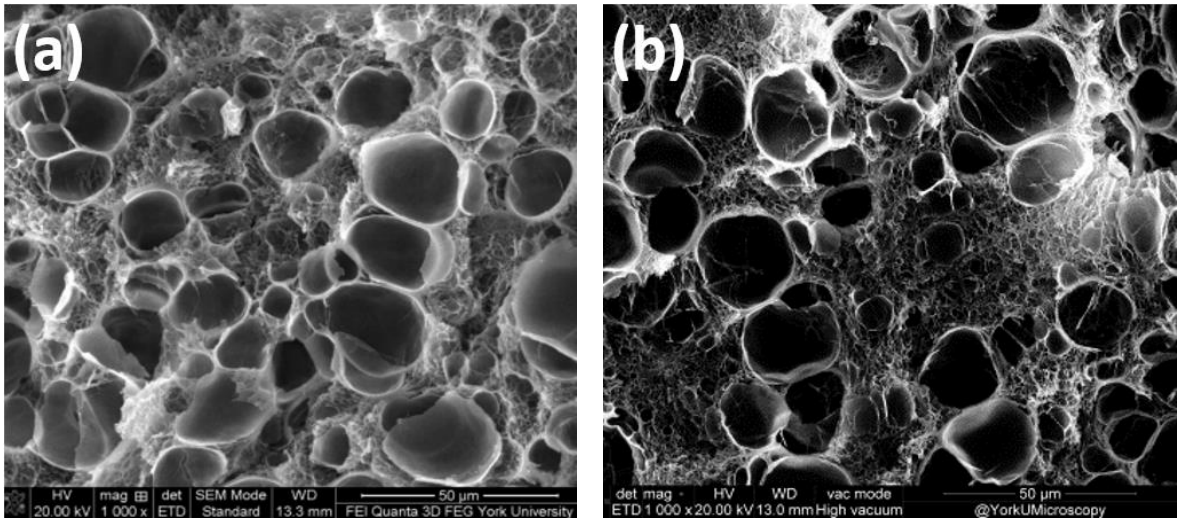


**Figure 4.10 SEM micrographs at 1000x magnification of processed PVDF samples showing very similar foaming behavior at different holding times: (a) 0 min; and (b) 1440 min. [Processing conditions: $T_H$ = 180°C, $T_{sat}$ = 160°C, $P_{sat}$ = 2000 psi, $-dP/dt$ = 191 MPa/s].**

## 4.5 Effect of non-isothermal crystallization on the electroactive phase content (P3)

Varying the saturation temperature ($T_{sat}$) indirectly adjusted the non-isothermal crystallization time, allowing investigation of its effects on PVDF's electroactive phase content. $T_H$ and $t_{hold}$ were set to 180°C and 0 minute, respectively, due to the high $\beta$ and $\gamma$ contents previously obtained in these conditions. The corresponding non-isothermal crystallization time for $T_{sat}$ of 120°C, 140°C, and 160°C were 43, 30, and 20 minutes, respectively. It can be observed that the $\gamma$ crystal phase content has a positive relationship with the duration of non-isothermal crystallization time (Figure 4.11) due to $\gamma$ polymorph'sslow crystallization rate [53]. Decreasing

$T_{sat}$ to extend non-isothermal crystallization time allowed sufficient time for $\gamma$ polymorph to nucleate from existing $\alpha$ crystal seeds. The maximum fraction of 65.6% $\gamma$ phase content was achieved when $T_{sat}$ was reduced to 120°C (i.e., non-isothermal crystallization time of 43 mins). It is interesting to note that the fractions of $\beta$ and $\gamma$ crystal phases have an inverse relationship, $F_\beta$ reaching a low of 3.9% at the maximum $F_\gamma$. This inverse relationship will appear more hereafter and will be discussed in detail later in the report.

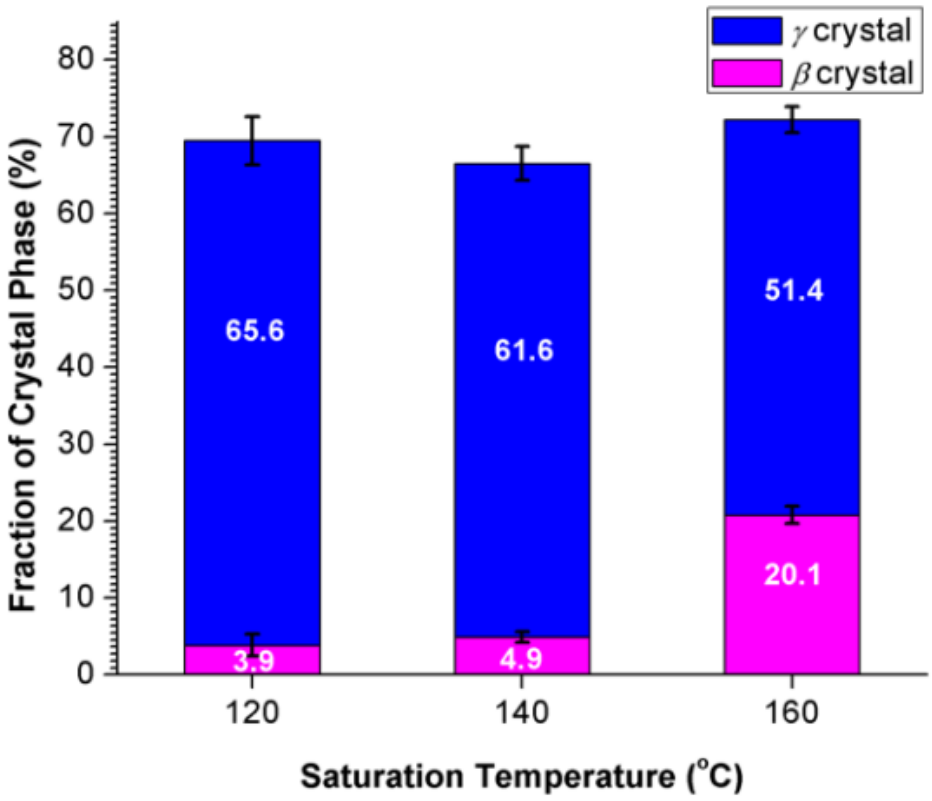


**Figure 4.11 Effect of $T_{sat}$ on the fractions of $\beta$ and $\gamma$ crystal phases. [Processing conditions: $T_H$ = 180°C, $t_{hold}$ = 0 min, $P_{sat}$ = 2000 psi, and $-dP/dt$ = 191 MPa/s].**

## 4.6 Effect of saturation pressure ($P_{sat}$) and pressure drop rate (*-dP/dt*) during $ScCO_2$ processing and foaming on the electroactive phase content (P4)

During phase P4, PVDF samples were subjected to $ScCO_2$ processing at different $P_{sat}$ and the sample underwent physical foaming during $CO_2$ release at various *–dP/dt*. There is a strong positive relationship between $\beta$ crystal content and $P_{sat}$ (Figure 4.12). When $P_{sat}$ increased to 2500 psi, a high $F_\beta$ of 28.5% was achieved. Increasing $P_{sat}$ dissolved more $ScCO_2$ into the PVDF matrix and the higher pressure gradient increased *-dP/dt* during gas release. Both promoted thermodynamic instability in the PVDF-$ScCO_2$ system, resulting in an increased cell nucleation rate and led to bigger and more uniform cell morphology (Figure 4.13). In addition to cell uniformity, the increase in $P_{sat}$ also enhanced *VER*. The highest $P_{sat}$ of 2500 psi resulted in a high *VER* of 8.8 while $P_{sat}$ of 1200 psi had a *VER* of 2.3. It can be concluded that the strain along the cell walls during foam expansion mimicked the strain by mechanical stretching to induce $\alpha$ to $\beta$ phase transformation. Therefore, an enhanced *VER* caused by an increase in $P_{sat}$ resulted in a higher $\beta$ phase content. There was a decrease in $\gamma$ crystals as $P_{sat}$ increased from 2000psi to 2500psi. This could be correlated to the $\gamma$ to $\beta$ phase transformation that occurs when a sample is stretched at higher temperatures (i.e., 130°C) [85]. The high temperature facilitated crystal orientation and coupled with applied strain, the $T_3GT_3G'$ conformation of $\gamma$ crystals were more comfortable converting to $\beta$'s TTT conformation over that of $\alpha$'s TGTG conformation. As the foam expansion mimicked the strain from mechanical stretching, this $\gamma$ to $\beta$ transformation could have occurred as well.

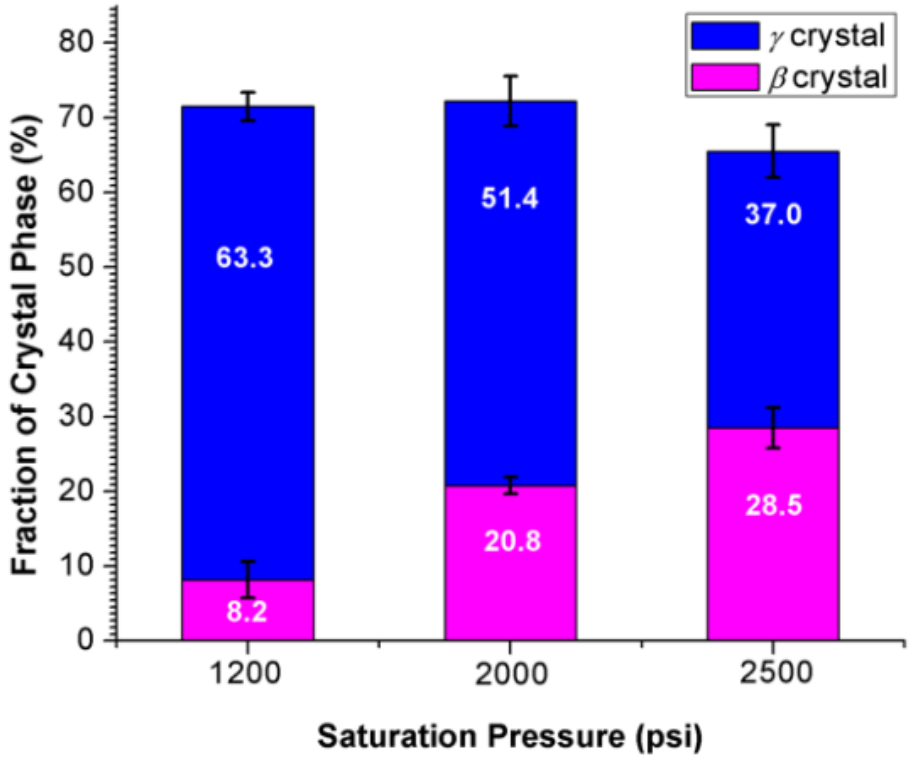


**Figure 4.12 Effect of $P_{sat}$ on the fractions of $\beta$ and $\gamma$ crystal phases. [Processing conditions: $T_H$ = 180°C, $t_{hold}$ = 0 min, $T_{sat}$ = 160°C, and $-dP/dt$ = 191 MPa/s].**

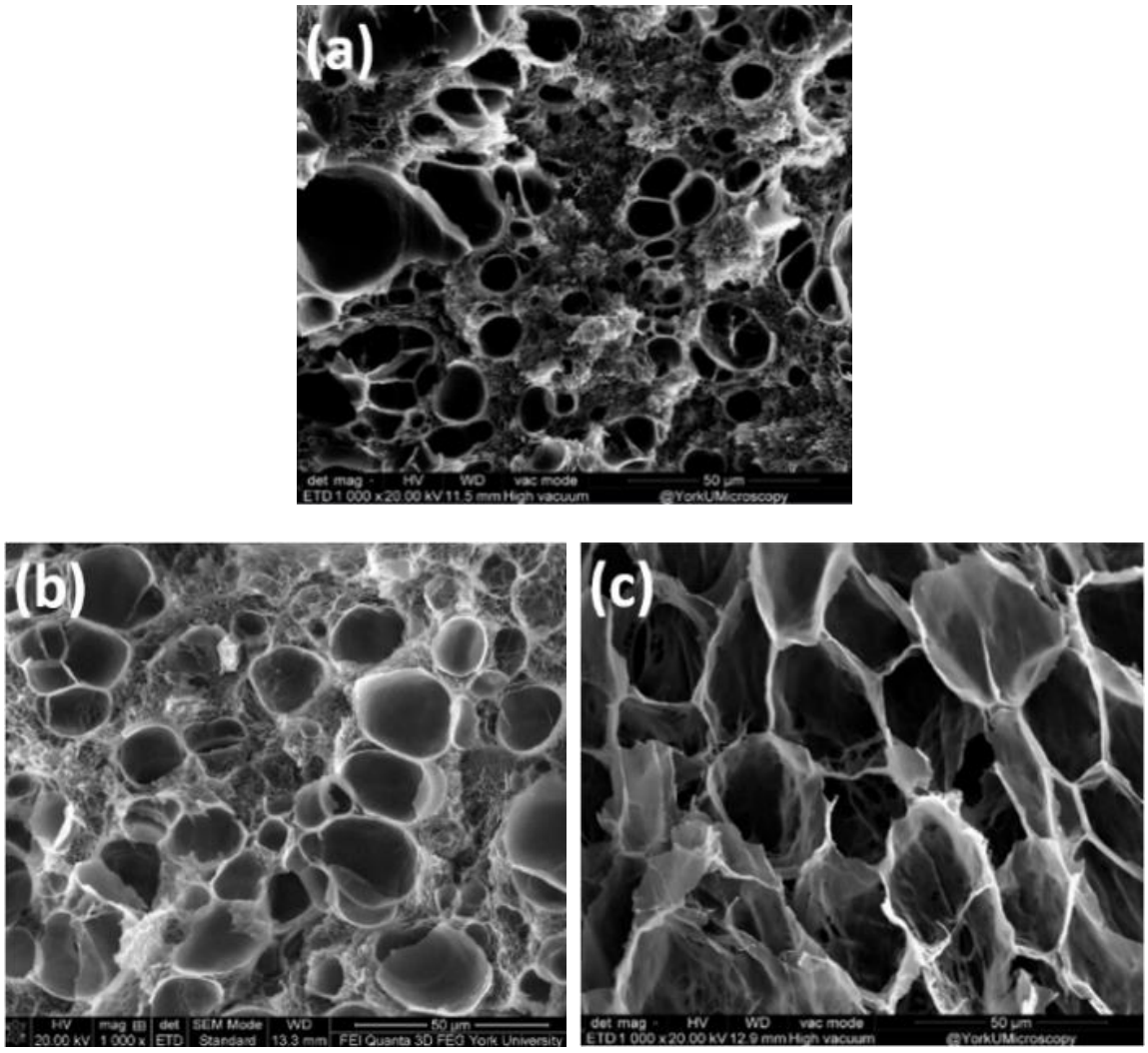


**Figure 4.13 SEM micrographs at 1000x magnification of PVDF samples foamed using $P_{sat}$ of: (a) 1200 psi; (b) 2000 psi; and (c) 2500 psi. [Processing conditions: $T_H$ = 180°C, $t_{hold}$ = 0 min, $T_{sat}$ = 160°C, and $-dP/dt$ = 191 MPa/s].**

Pressure drop rate was varied by partially closing the metering valve to control the gas flow when the exhaust valve was opened. Consistent with the parametric studies for $P_{sat}$, the fast cooling associated with a high $-dP/dt$ favored $\beta$ phase nucleation, resulting in an increase from

8.8% to 20.8% from 48 MPa/s to 191 MPa/s, respectively (Figure 4.14). A reduced *-dP/dt* decreased the cooling rate, which suppressed $\beta$ phase nucleation and favored $\alpha$ phase nucleation. At the lowest *-dP/dt* (i.e., 48 MPa/s), the reduced thermodynamic instability suppressed cell nucleation rate, resulting in a low *VER* of 1.8. The resultant low *VER* failed to effectively apply strain on the PVDF matrix and contributed to the decrease in the $\beta$ phase content.

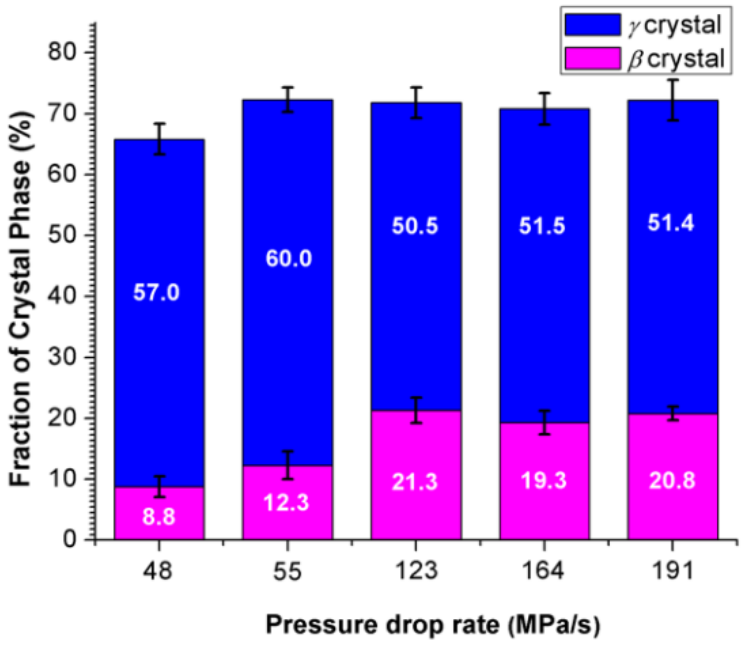


**Figure 4.14 Effect of *–dP/dt* on the fractions of $\beta$ and $\gamma$ crystal phases. [Processing conditions: $T_H$ = 180°C, $t_{hold}$ = 0 min, $T_{sat}$ = 160°C, and $P_{sat}$ = 2000 psi].**

## 4.7 Relationship between $\gamma$ and $\beta$ crystal of the processed PVDF samples

Both $\beta$ and $\gamma$ crystals are electroactive crystals of PVDF and both are very desirable to enhance

PVDF's piezoelectric property. Our processed samples allowed a co-existence of both $\beta$ and $\gamma$ crystals. To optimize and enhance both crystal phases, the relationship between $\beta$ and $\gamma$ crystals must be analyzed. The positive relationship between $\beta$ phase content and PVDF's *VER* has become very evident through various parametric studies. The processing conditions with the highest $F_\beta$ usually had the highest *VER*. High *VER* is beneficial to $\beta$ phase formation, which can be attributed to the high local strain introduced on the cell wall of PVDF foam during bubble expansion. Another relationship that was observed throughout parametric studies was the inverse relationship between $\beta$ and $\gamma$ crystals. It can be identified that while the mechanism for $\beta$ and $\gamma$ crystal formations are independent, they indirectly affect each other through the $ScCO_2$ foaming step. $\gamma$ crystals are formed by thermal processing, either non-isothermal or isothermal crystallization, with the presence of existing $\alpha$ crystals. $\beta$ crystals, on the other hand, are formed during the physical foaming of $CO_2$ bubbles causing local strain on the PVDF matrix. Parametric experiments revealed that PVDF foams would have lower *VER* and $\beta$ phase content when there existed a high content of $\gamma$ crystals prior to foaming. This was observed during parametric analysis for non-isothermal crystallization (i.e. P3) and the reverse during parametric analysis for heating temperature (i.e., P1), where the absence of $\gamma$ crystals resulted in high $\beta$ content and *VER*. $\gamma$ crystals has a melting temperature 10°C higher than that of the $\alpha$ and $\beta$ crystals. The naturally compact chain group conformation of the $\gamma$ phase limited the amount of $ScCO_2$ dissolved into the polymer matrix. Therefore, the amount of $CO_2$ available for bubble growth decreased. This ultimately resulted in a reduced $\beta$ phase content due to the lower degree of local strain within the

cell walls. Figure 4.15 clearly shows the opposing trends of $\beta$ and $\gamma$ phase content as *VER* varied, plotting values obtained from all parametric experiments observed up until now (i.e., $T_H$, $t_{hold}$, $T_{sat}$, $P_{sat}$, and $-dP/dt$). Therefore, to obtain a high fraction of electroactive phase content, a good balance of both $\beta$ and $\gamma$ phases are needed.

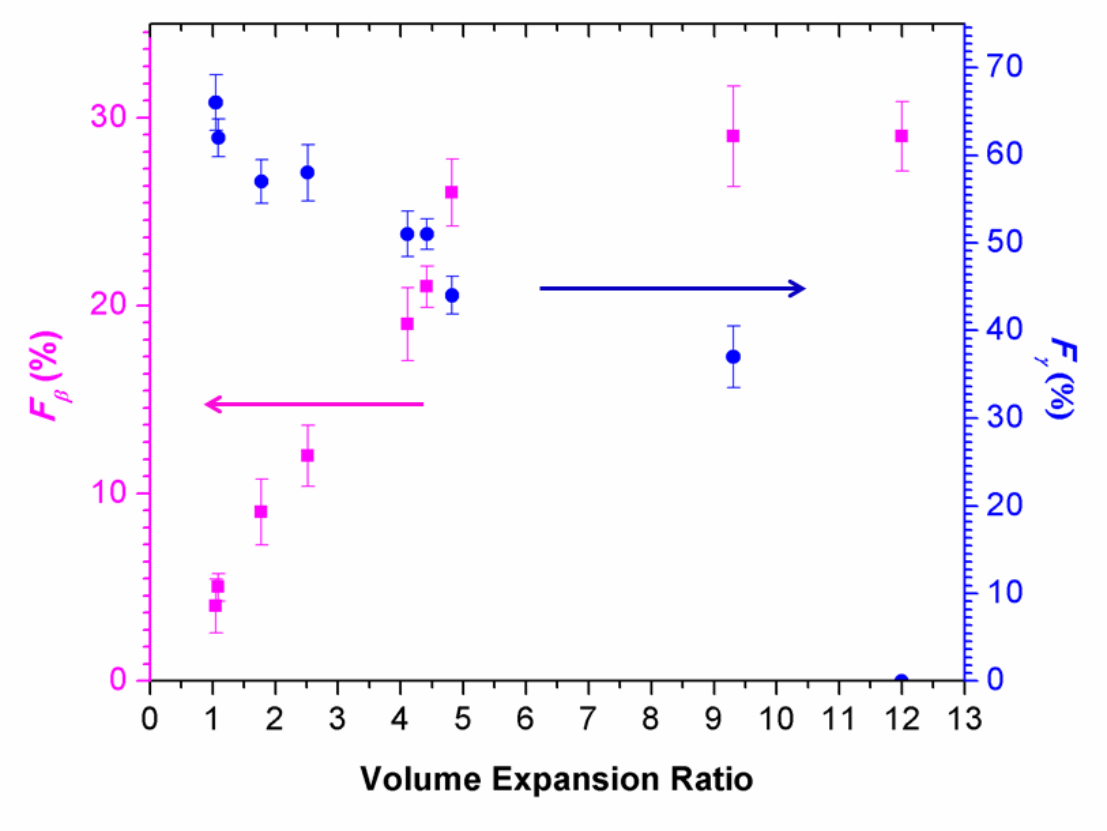


**Figure 4.15 Relationship between $F_\gamma$ (circle) vs. *VER* vs. $F_\beta$ (square) of samples processed through thermal and $ScCO_2$ using temperature profile 2 and various parametric variations.**

## 4.8 Effect of cell morphology on the $\beta$ phase content of PVDF

From the parametric studies from previous sections it can be summarized that large cells increase

*VER* and subsequently, the $\beta$ phase crystals. However, the analysis of the effects of cell uniformity has yet to be analyzed. PVDF foams with similar volume expansion ratio but different cell morphologies (i.e., cell population density and average cell size) could be fabricated by different processing conditions. Two PVDF foams with similar *VER* prepared by different processing conditions, as summarized in Table 4.3, were compared to elucidate the effects of cell morphologies on $\beta$ phase content.

While PVDF samples prepared using processing conditions 1 and 2 yielded foams with similar *VER*, the fraction of $\beta$ phase content using processing condition 2 (i.e., 31.0%) was significantly higher than that prepared using processing condition 1 (i.e., 20.8%). From SEM micrographs, it can be observed that condition 1 yielded extremely non-uniform foam morphology (Figure 4.16(a)). While there existed some large cells with cell diameters of 15μm, the vast majority of the cells were in submicron scale. With the presence of $\gamma$ crystals during $ScCO_2$ foaming, the limited cell expansion in the proximity of crystals led to localized stress fields, promoting the strain-induced nucleation of secondary cells with smaller sizes [86]. These small cells would not be able to induce a high degree of strain, requiring the majority of the strain from the minute number of large cells. This level of stress would be unable to effectively align the molecular chains to the $\beta$ phase. In contrast, condition 2 had very uniform and large cell morphology, with an average cell diameter of 14μm (Figure 4.16(b)). Without the presence of $\gamma$ crystals, larger cells grew throughout the PVDF matrix. The higher degree of strain induced facilitated the alignment of the molecular chains groups into the TTT conformation and resulted in an increased $\beta$ phase content. There is a strong positive relationship between average cell size,

*VER*, and $F_\beta$, which again confirmed the potential of using $ScCO_2$ foaming to mimic the mechanical stretching-induced $\alpha$ to $\beta$ phase transformation.

**Table 4.3 Experimental conditions for parametric studies of $CO_2$ cell morphology**

| | **Processing parameters** | | | | | |
|---|---|---|---|---|---|---|
| | $T_H$ | $t_{hold}$ | $T_{sat}$ | $P_{sat}$ | ***VER*** | $F_\beta$ |
| **Condition 1** | 180°C | 0 min | 160°C | 2000 psi | 4.4 | 20.8% |
| **Condition 2** | 220°C | 0 min | 160°C | 2500 psi | 4.7 | 31.0% |

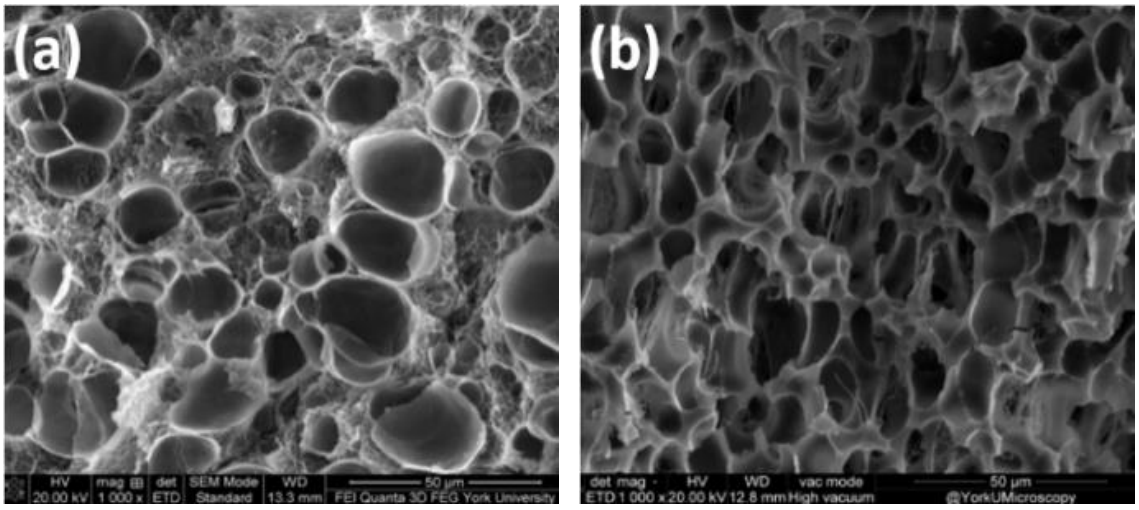


**Figure 4.16 SEM micrographs at 1000x magnification of PVDF samples prepared using: (a) condition 1; and (b) condition 2.**

## 4.9 Comparison of thermal and $ScCO_2$ processing method and uniaxial mechanical stretching to promote PVDF electroactive phase content

The proposed research was compared to the popular and most common mechanical stretching method. From this comparison, we can confirm that our novel processing method is able to achieve a comparable electroactive phase content. 100μm thick as-molded PVDF samples were mechanically stretched at 90°C, which was the ideal stretching temperature reported in literature for various strain levels [26]. The resulting fraction of electroactive crystal phases (i.e., $\beta$ and $\gamma$ polymorphs) in PVDF processed by either thermal and $ScCO_2$ or uniaxial mechanical stretching were compared (Figure 4.17). It must be noted that the maximum strain level that could be applied to PVDF film samples in-house without breaking was three. $\gamma$ crystals were absent in the mechanically stretched samples, and as expected, $\beta$ phase content increased with strain level. Straining PVDF film by three times increased $F_\beta$ to 68%, representing a significant increase from the 31% $F_\beta$ in the 100μm as-molded sample. For PVDF samples that underwent thermal and $ScCO_2$ processing, the maximum fraction of 72% electroactive phase (i.e., including both $\beta$ and $\gamma$ phases) was achieved at the base case condition. This was slightly better than the highest electroactive phase content achieved by mechanical stretching method. However, when taken into account $\chi_c$ of the processed samples, the samples processed by thermal and $ScCO_2$ method was able to maintain the $\chi_c$ at 52% while the mechanically stretched sample destroyed crystals and decreased its $\chi_c$ down to 43%. Therefore, the total electroactive crystal phase of the thermal and $ScCO_2$ processed sample was 50% higher than that of the mechanical stretching method. An

interesting comparison can be made between PVDF with strain level of 200% to thermal and $ScCO_2$ processed PVDF with *VER* of 12. This *VER* is equivalent to a linear strain of approximately 2.3. If $\beta$ phase content with respect to $\chi_c$ (i.e., product of the overall $\chi_c$ and the fraction of $\beta$ phase crystal) of the PVDF foam sample was compared to that of the mechanically stretched sample with a strain rate of two, it was found that both samples yielded a total $\beta$ crystal content of about 17.5%. Therefore, it can be concluded that the local strain caused by the cell growth during $ScCO_2$ foaming did in fact effectively mimic the mechanical stretching method.

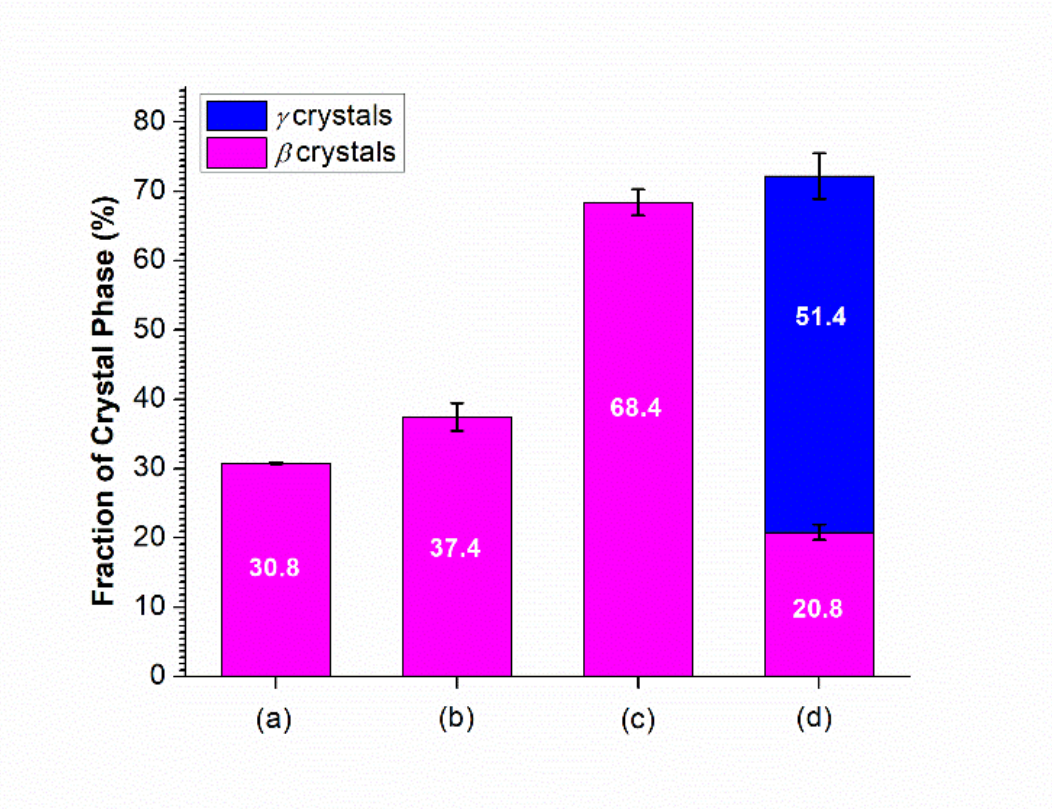


**Figure 4.17 Fractions of $\beta$ and $\gamma$ crystal phases of PVDF prepared at: (a) as-molded 100μm PVDF sample; (b) mechanically stretched to 200%; (c) mechanically stretched to 300%; (d) thermal and $ScCO_2$ processing at base condition.**

# Chapter 5 Piezoelectric property of micro-and-nanostructured PVDF

Before measuring and calculating for PVDF's piezoelectric property, a common post-processing step of electric poling must be completed. The dipoles of PVDF are in random orientation, therefore the electric poling step allowed reorientation of PVDF's dipoles along a common direction to properly measure the material's true piezoelectric property. After this common step, its piezoelectric property can be determined by measuring and calculating for the charge produced and its piezoelectric coefficient, respectively. The piezoelectric coefficient can properly represent the piezoelectric property due to its units of C/N, defined as the amount of charge produced per unit of force applied.

## 5.1 Experimental Procedure

PVDF films were prepared so that the post-processing electric poling step and the piezoelectric coefficient measurement step could be conducted in succession without significant time delays. Therefore, preparation was conducted while considering the main conditions for both steps. First, the processed PVDF films using temperature profile 2 were compressed to 100$\mu$m in the compression molding machine (4386 CH, from Craver Press) at room temperature for approximately 24 hours. By lowering the sample thickness, it ensured that the high voltage applied during the electric poling step would exceed the coercive field of PVDF and successfully align the dipoles. Characterization analysis proved that this compression step did not

significantly affect the crystallinity or crystal phases of the processed sample. The now 100$\mu$m PVDF samples were cut into rectangular pieces of 0.5” x 1.5” to best fit the size of the tensile setup in the piezoelectric coefficient measurement stage. Silver epoxy adhesive (#8331-14G, MG Chemicals) was used as the conducting electrodes on both side of the PVDF sample and put on manually into a 6mm x 6mm square in the centre. To prevent arcing or flashovers during poling that will permanently damage the material, the electrodes were kept at the centre and ensured it did not reach the edge of the film [67]. The application of the silver epoxy was done as thinly as possible to prevent clamping affects on the polymer and to not limit piezoelectric performance [67]. Aluminum wires were attached to the electrodes also using silver epoxy. The wires were coiled on top of the electrode on either side during poling to ensure it does not short circuit the system.

### 5.1.1 Electric Contact Poling

To align the PVDF dipoles, a high voltage power source (ES30, Gamma) with a maximum output voltage of 30 kV was used to create the electrical field over the thickness of the sample. The power supply A homemade electric contact poling setup was designed, with high importance on safety due to the use of high voltage (Figure 5.1). Two cylindrical 6061 Aluminum alloys 0.25” thick and 0.5” in diameter were used as electrodes for the poling system. A glass-mica ceramic square plate of 0.25” × 2” × 2” was used as the dielectric plate, to limit current flow in the PVDF sample and reduce the probability of electrical breakdown [65]. Due to the air voids present in the foamed PVDF films, the breakdown voltage is expected to be lower than standard.

The entire system was covered by high density polyethylene (HDPE) as the insulating material, with holes to tight fit the Aluminum electrodes. To keep the entire system in place and provide a compression force for better contact between the electrodes and the sample, two nylon threaded rods and nuts were used. Lastly, the entire system was placed within a plastic box and inside a fume hood with glass doors. This was to reduce the exposure to the electromagnetic fields (EMFs) from the high voltage during operation. The SolidWorks drawings of the homemade contact poling setup, its components, and their dimensions can be seen in Appendix A.

All samples were poled at around 0.07 kV/µm for 30 minutes at room temperature, following the average values found in literature to sufficiently pole PVDF samples. Some sample could not be poled above 0.07 kV/µm because their thickness could not be made any thinner and the applied voltage was limited at 30 kV. After poling, the setup was short circuited and then grounded overnight to dissipate any remaining charge that could hinder the piezoelectric coefficient measurements.

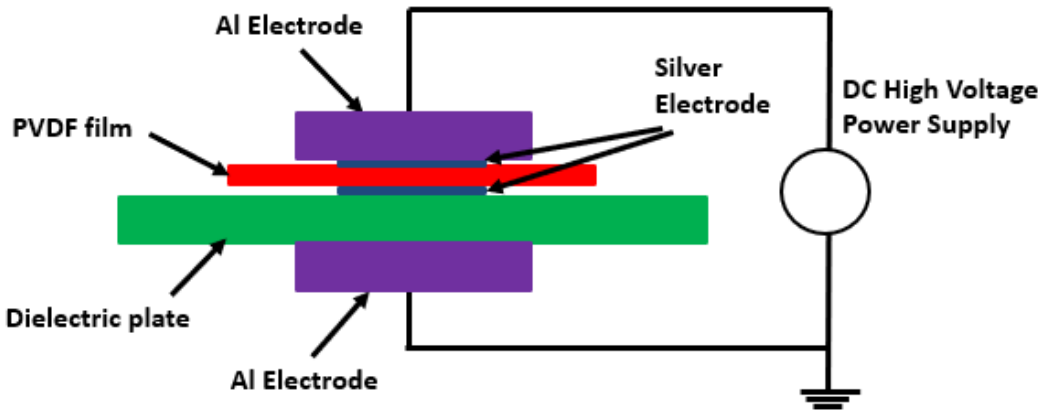


**Figure 5.1 Simple schematic drawing of the contact poling setup. (Note that drawing is not to scale)**

### 5.1.2 Piezoelectric coefficient

The piezoelectric coefficient, $d_{31}$, of the poled and unpoled PVDF samples were determined by using a simple tensile setup (Figure 5.2) Tensile stress was applied along its longest side (i.e., 1 direction) and its developed charge on the electrode surface area was measured along the thickness of the sample (i.e., 3 direction). The applied tensile stress was supplied by a rheometer (Discovery Series Hybrid Rheometer HR-3, TA Instruments) and its developed charge was measured by an electrometer (Model 6514 System Electrometer, Keithley). The resulting piezoelectric coefficient was calculated using Equation (7).

$$d_{31} = \frac{Q \times (\mathrm{w_{PVDF}} \times t_{PVDF})}{F \times (w_{electrode} \times l_{electrode})} \tag{7}$$

Here $Q$ is the induced charge, $F$ is the force applied to the PVDF sample, $w_{PVDF}$ and $t_{PVDF}$ are the PVDF sample's width and thickness, respectively, and $w_{electrode}$ and $l_{electrode}$ are the silver electrode's width and length. HR-3 applied a constant tensile force of 5 N for 45s.

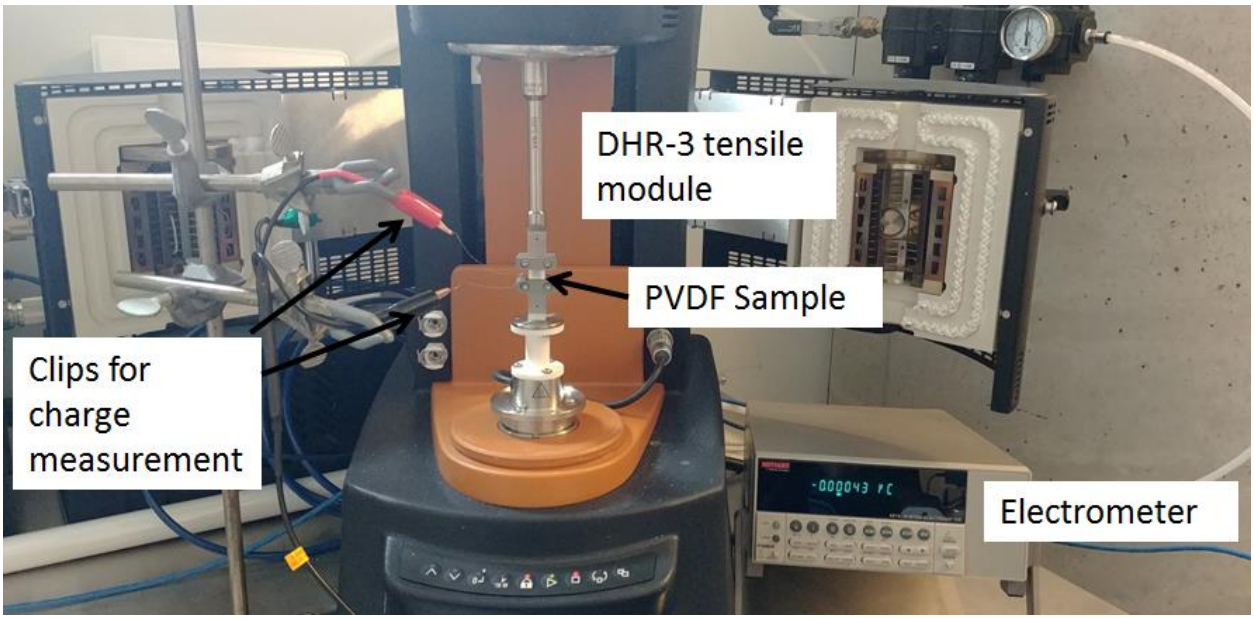


**Figure 5.2 Tensile setup for piezoelectric coefficient, $d_{31}$, measurement**

## 5.2 Results & Discussion

The determination of the $d_{31}$ values were conducted on four main conditions: 100µm thick as-molded sample, best $F_\gamma$ case, best $F_\beta$ case, and best $F_{EA}$ case of the processed PVDF samples. The detailed processing conditions and its crystal content can be seen in Table 5.1. For all three samples that exhibited optimal crystal contents, $t_{hold}$ was set to 0 min and $-dP/dt$ was 191 MPa/s. As stated previously, $\beta$ crystal has the highest dipole moment per unit cell out of all the polymorphs, giving rise to a large spontaneous polarization. It can be observed that before poling, the best $F_\beta$ case with 34% $\beta$ crystal has a slightly higher $d_{31}$ compared to the best $F_\gamma$ case with 66%$\gamma$ crystals, even though this is twice the $\beta$ crystal content (Figure 5.3). After poling, while both $d_{31}$ values increased, the best $F_\beta$ increased significantly. This was expected as with voltage

alone, it is easier to affect the crystalline structure of $\beta$ crystal than the dense, tight conformation of the $\gamma$ crystals.

It is interesting to note that while the 100μm as-molded PVDF and the best $F_\beta$ case had very similar $\beta$ crystal content, the $d_{31}$ of the latter was significantly higher, especially after poling. One possibility could be that for the best $F_\beta$ case, the $CO_2$ bubbles were able to better align the crystalline structure in a common direction compared to the heat and pressure treatment of the 100μm as-molded PVDF. Better molecular alignment of PVDF with enhanced electroactive crystals phase content would create a larger dipole moment, resulting in the higher $d_{31}$ value. Another possibility is that after poling, the voids left by the expansion of the $CO_2$ bubbles could have been internally charged with opposite polarity, enhancing piezoelectric property. It had been observed in piezoelectret foams that when a large voltage is applied, Paschen breakdown occurs in the air voids causing an electrical discharge [87]. This electrical breakdown will only happen in the air voids because the dielectric breakdown of air is much lower than that of the PVDF polymer. This would internally charge the air voids and deposit charges onto the surfaces of the pores. When the material is stretched during piezoelectric coefficient measurement, the air voids would also be stretched, increasing the distance between the void's charged surfaces which would increase the overall dipole moment in the material. Since the best $F_\beta$ case had the one of the biggest average cell diameter of 25μm, it would have the most internally charged void surfaces after poling, accounting for its much larger $d_{31}$ value. Both before and after poling, the sample with the best $F_{EA}$ had the highest piezoelectric coefficient of 4.2 and 7.7 pC/N, respectively, due to its high content of both $\beta$ and $\gamma$ crystals.

When a 110µm thick poled PVDF sample from Measurement Specialties (MSI) was measured, the obtained $d_{31}$ value was half of what was reported in their specifications. It was speculated that the piezoelectric setup in-house was not able to apply the same level of stress as in the literature (i.e., 5 MPa in-house versus 20 – 40 MPa in literature [74]). There are three factors that could account for this. One would be the large size of the polymer which was limited by manual application of the silver epoxy onto the PVDF sample. Second would be the rheometer's limited applied force. Lastly, due to the stiffness of the silver epoxy electrodes, this could not be transferring all the stress to the PVDF sample [81], resulting in lower stress being developed on the PVDF sample and subsequently, a lower piezoelectric property. Additionally, the charge in the ambient surroundings could have hindered the charge measurements made by the electrometer. To prevent this and obtain more accurate measurements, a Faraday's cage is recommended for the future due to its ability to isolate the system using a metal shied [88]. Once these problems are fixed, the $d_{31}$ values are expected to increase closer to its true value.

**Table 5.1 Fraction of $\beta$, $\gamma$, and electroactive phases of different PVDF samples and their processing conditions**

| **Name** | $T_H$ **(°C)** | $T_{sat}$ **(°C)** | $P_{sat}$ **(psi)** | $F_\beta$ **(%)** | $F_\gamma$ **(%)** | $F_{EA}$ **(%)** |
|---|---|---|---|---|---|---|
| 100µm as-molded PVDF | - | - | - | 31.0 | - | 31.0 |
| Best $F_\gamma$ | 180 | 120 | - | 4.3 | **66.2 ± 1.5** | 70.5 |
| Best $F_\beta$ | 220 | 160 | 2000 | **33.7 ± 1.3** | - | 33.7 |
| Best $F_{EA}$ | 180 | 160 | 2000 | 20.8 | 51.4 | **72.2 ± 2.9** |

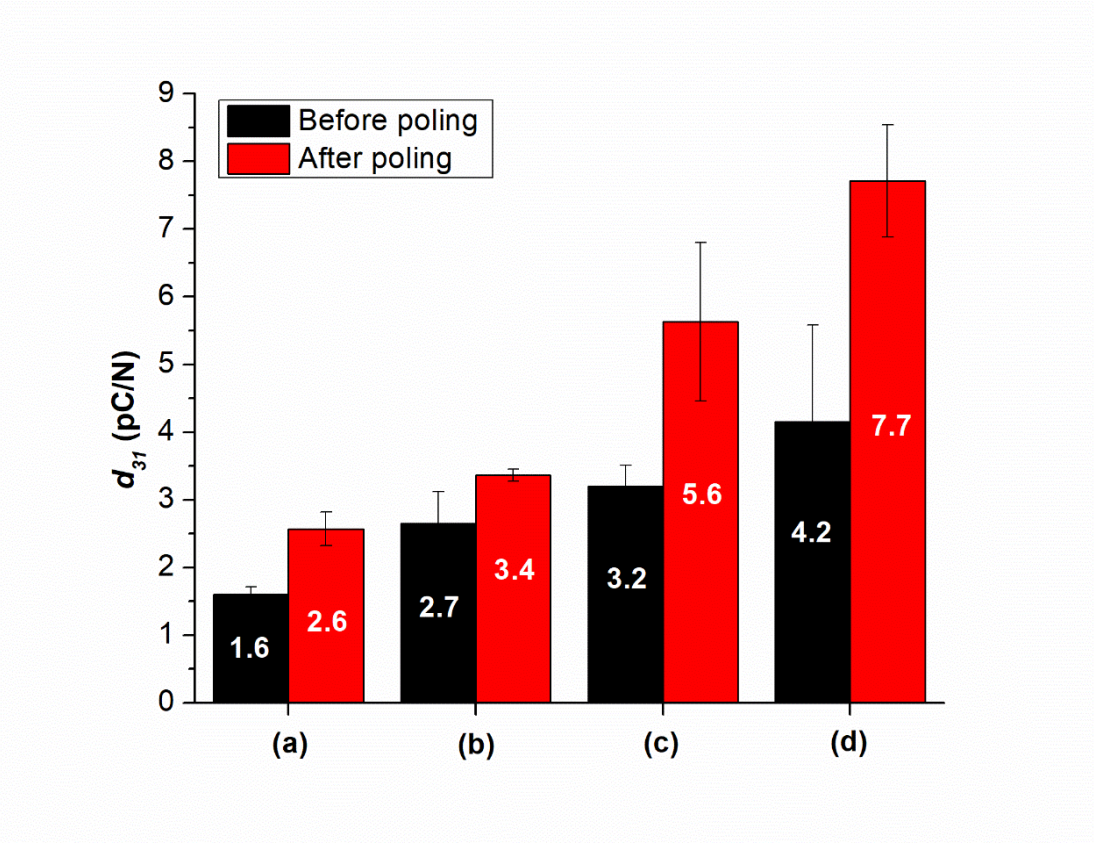


**Figure 5.3 Piezoelectric coefficient $d_{31}$ values before and after poling: (a) 100μm as-molded PVDF; (b) Best $F_\gamma$ sample without the presence of $ScCO_2$; (c) Best $F_\beta$ sample; and (d) Best $F_{EA}$ sample.**

# Chapter 6 Conclusion and Future Directions

## 6.1 Conclusion

Overall, this research was able to use the novel processing method of thermal and $ScCO_2$ to enhance the electroactive crystal phases (i.e., $\beta$ and $\gamma$) and piezoelectric property of PVDF. The two temperature profiles used were able to fully elucidate the various mechanisms to individually nucleate the distinct polymorphs, while allowing them to co-exist within the same sample. The final results obtained were higher than the common mechanical stretching method in terms of crystallinity and its piezoelectric property was comparable to literature.

By utilizing temperature profile 1, this provided the initial investigation of physical $CO_2$ foaming of PVDF and its effect on the crystalline structure and the distinct polymorphs. The sudden pressure drop during the $ScCO_2$ gas release led to thermodynamic instability in the PVDF-$CO_2$ system and resulted in the nucleation of $CO_2$ cellular structures within the PVDF matrix. The optimal physical $CO_2$ foaming of PVDF with a maximum *VER* of 15.4 was at a saturation temperature, $T_{sat}$, of 160°C and a saturation pressure, $P_{sat}$, of 2000psi. If $T_{sat}$ was lower, the PVDF matrix was too stiff to generate cellular structures, and if $T_{sat}$ was higher, the foam structure would rupture. With a lower $P_{sat}$, there was lower plasticization effect, reducing chain mobility and gas condensability. With a higher $P_{sat}$, the plasticization effect was too significant and the resulting increase in foam expansion ruptured the cell walls, lowering its *VER*. It was also observed that the degree of crystallinity, $\chi_c$, increased when the sample was subjected to an optimal level of plasticizing effect. In particular, a sufficient amount of pre-existing crystals was

needed to act as seeds to promote crystal perfection during annealing. Evidenced by this, the decrease in $\chi_c$ was observed as the temperature increased beyond the materials' onset melting temperature, reducing pre-existing crystals. A maximum $\chi_c$.of 54% was achieved for all $P_{sat}$ at its own distinct $T_{sat}$. There was no presence of $\gamma$ crystals, but only $\alpha$ and $\beta$ crystals, using temperature profile 1.

Temperature profile 2 built upon temperature profile 1 with addition of multiple steps while utilizing the optimal foaming conditions of 2000 psi and 160°C. Parametric studies revealed that $\gamma$ phase nucleation was achieved through isothermal and non-isothermal crystallization before $ScCO_2$ processing. The isothermal crystallization caused a direct $\alpha$ to $\gamma$ transformation, introducing the $\gamma'$ phase. Non-isothermal crystallization was the main mechanism for $\gamma$ phase nucleation. With sufficient pre-existing $\alpha$ crystals to act as seeds and long non-isothermal crystallization time, a maximum fraction of $\gamma$ phase content of 65.6% was achieved.

$\beta$ phase nucleation had a positive relationship with $CO_2$ foam expansion during the $ScCO_2$ processing phase. By increasing $P_{sat}$, more $ScCO_2$ dissolved into the PVDF matrix and its higher pressure gradient promoted the thermodynamic instability in the PVDF–$ScCO_2$ system resulting in an enhanced cell nucleation rate. The increase in cell size and *VER* caused more strain on the PVDF sample, inducing $\alpha$ to $\beta$ phase transformation that wasas commonly seen in the mechanical stretching method. Additionally, the fast cooling caused by a high *-dP/dt* favored the nucleation of $\beta$ phase. The significance of foam morphology and uniformity became evident when PVDF samples processed at two different conditions exhibited similar *VER* values but very

contrasting $\beta$ phase contents. The sample with the larger $\beta$ content displayed more uniform cellular structure under SEM. With large and uniform cellular structure, a maximum $F_\beta$ of 33.7% was achieved.

While the mechanism for $\beta$ and $\gamma$ phase formations were found to be independent, they indirectly affected each other through the $ScCO_2$ processing step. When there were large amounts of $\gamma$ crystals present, its tight conformation hindered the growth of bubbles and lowering $\beta$ phase content due to lack of local strain on the PVDF matrix. Evidently, the samples with the highest *VER* and $\beta$ phase content had no presence of $\gamma$ crystals. It can be concluded that to obtain a high fraction of electroactive phase content, a good balance of both $\beta$ and $\gamma$ phases are needed.

The highest fraction of PVDF electroactive phase achieved by thermal and $ScCO_2$ processing (i.e., 72.2%) was shown to be slightly higher than that yielded by mechanically stretching PVDF film by 300% (i.e., 68.4%). Additionally, 200% stretched sample and $ScCO_2$ processed sample with *VER* of 12 (i.e., linear strain of 2.3), had a similar total $\beta$ crystal content of 17.5%, proving the successful mimicking of $CO_2$ gas strain to that by the mechanical stretching method. Multiple temperature and pressure phases within this processing approach were conducted in a single batch foaming chamber, representing an industrially viable process. Overall, this method revealed the potential of using thermal and $ScCO_2$ processing for the individual and combined promotion of the electroactive $\beta$ and $\gamma$ phase nucleation.

After electric poling at 0.07 kV/μm for 30 minutes at room temperature, the piezoelectric coefficient, $d_{31}$, value was measured. As expected, $d_{31}$ increased after electric poling for all

samples due to better alignment of the dipoles. $\beta$ crystal's high dipole moment was affirmed when the best $F_\beta$ case with 34% $\beta$ crystal had higher $d_{31}$ compared to the best $F_\gamma$ case with 66%$\gamma$ crystals, twice the $\beta$ crystal content. The thermal and $ScCO_2$ processed samples had a higher $d_{31}$ values compared to as-molded samples, before and after poling, despite having similar $\beta$ phase content. It can be elucidated that the expansion of the $CO_2$ bubbles could have better aligned the dipoles, and/or it is due to the many internally charged gas voids within the polymer, increasing the overall dipole moment in the sample. A maximum $d_{31}$ of 7.7 pC/N was achieved after poling the best $F_{EA}$ case, having a good balance of both $\beta$ and $\gamma$ crystals.

## 6.2 Future Directions

The main goal of this research was to understand and elucidate the crystallization and crystal formation of PVDF under various conditions. The current processing method could be enhanced by applying constrained foaming. This will allow expansion in one direction which will apply a greater strain on the polymer than expansion through 3 directions (i.e., the current volume expansion). Additionally, the post-processing step of electric poling could be enhanced by replacing it with corona poling. This method is able to apply a greater voltage without breaking down the material due to not directly applying the voltage onto the polymer itself. With a higher applied voltage, the dipoles will be better aligned along a common direction.

Through this study, the independent processing methods for $\beta$ and $\gamma$ phase nucleation were explored. Using this knowledge, future research on piezoelectric polymer PVDF will most likely explore sustaining a high $\gamma$ phase while increasing the $\beta$ phase, or vice versa, by splitting

up the thermal and $ScCO_2$ processing method and combining it with other processing method/s. This could include thermal processing to increase its $\gamma$ content, and then mechanically stretching to increase its $\beta$ content. Another method could be the addition of fillers and then subjecting the sample to a $ScCO_2$ environment. It is possible that the fillers may organize itself around the surfaces of the bubbles to assist in the alignment of the crystalline structures. Additionally, the use of air voids to increase the piezoelectric property could be explored as well. With an abundance of cell sizes and densities from SEM micrographs, the effectiveness of internally charged voids could be parametrically examined, along with poling voltages.

Promotion of the overall degree of crystallinity of PVDF are of interest as well. Many methods, including mechanical stretching, led to a partial destruction of the crystalline structure, lowering the degree of crystallinity [27] [28]. Overall, without a high degree of crystallinity, a high electroactive phase content, whether $\beta$ or $\gamma$, or both, will not enhance the piezoelectric property enough. The earlier stages of this study suggested that an optimal level of plasticizing effect coupled with pre-existing crystals promoted $\chi_c$. Utilizing this as a stepping stone and realizing the importance of $\chi_c$, the next focus could be on increasing the degree of crystallinity.

Using this study, the long term goal to enhance the piezoelectric property of PVDF can be achieved. The success of this goal could replace the current toxic piezoelectric ceramic PZT and be used in more application involving complex shapes and durability. The author hopes that in the future, a great enhancement of PVDF's piezoelectric property will also propel its uses towards energy harvesting applications, such as nanogenerators, that can be easily integrated into currently existing tools.

# REFERENCES


[1] P. Ueberschlag, "PVDF Piezoelectric Polymer," *Sensor Review,* vol. 21, no. 2, pp. 118-125, 2001.

[2] H. Kawai, "The Piezoelectricity of Poly(vinylidene Fluoride)," *Japanese Journal of Applied Physics,* vol. 8, pp. 975-976, 1969.

[3] A. J. Lovinger, "Poly(Vinylidene Fluoride)," in *Developments in Crystalline Polymers - 1*, Springer, Dordrecht, 1982, pp. 195-273.

[4] D. Mandal, S. Yoon and K. J. Kim, "Origin of Piezoelectricity in an Electrospun Poly(vinylidene fluoride-trifluoroethylene) Nanofiber Web-Based Nanogenerator and Nano-Pressure Sensor," *Macromolecular Rapid Communications,* vol. 32, pp. 831-837, 2011.

[5] M. Vijatovic, J. Bobic and B. Stojanovic, "History and Challenges of Barium Titanate: Part 1," *Science of Sintering,* vol. 40, pp. 155-165, 2008.

[6] A. Jain, P. J, A. Sharma, A. Jain and R. P.N, "Dielectric and Piezoelectric Properties of PVDF/PZT Composites: A Review," *Polymer Engineering and Science,* pp. 1589-1613, 2015.

[7] P. Martins, A. Lopes and S. Lanceros-Mendez, "Electroactive phases of poly(vinylidene fluoride): Determination, processing and applications," *Progress in Polymer Science,* vol. 39, pp. 683 - 706, 2014.

[8] Q. Zhou, S. Lau, D. Wu and K. Shung, "Piezoelectric films for high frequency ultrasonic transducers in biomedical applications," *Progress in Material Science,* vol. 56, pp. 139-174, 2011.

[9] M. Sherar and F. Foster, "The design and fabrication of high frequency poly(vinylidene fluoride) transducers," *Ultrasonic Imaging,* vol. 11, pp. 75-94, 1989.

[10] X. Xue, S. Wang, W. Guo, Y. Zhang and Z. L. Wang, "Hybridizing Energy Conversion and Storage in a Mechanical-to-Electrochemical Process to Self-Charging Power Cell," *Nano Letters,* vol. 12, pp. 5048-5054, 2012.

[11] B. Dickens, E. Balizer, A. DeReggi and S. Roth, "Hysteresis measurements of remanent polarization and coercive field in polymers," *Journal of Applied Physics,* vol. 72, no. 9, pp. 4258-4264, 1992.

[12] H. Correia and M. Ramos, "Quantum modelling of poly(vinylidene fluoride)," *Computational Materials Science,* vol. 33, pp. 224-229, 2005.

[13] C. Riberiro, S. Moreira, V. Correia, V. Sencadas, J. Rocha, F. Gama, J. Ribelles and S.

Lanceros-Mendez, "Enhanced proliferation of pre-osteoplastic cells by dynamic piezoelectric stimulation," *RSC Advances,* vol. 2, pp. 11504-11509, 2012.

[14] B. Basse, B. Baguley, E. Marshall, G. Wake and D. Wall, "Modelling cell population growth with applications to cancer therapy in human tumour cell lines," *Progress in Biophysics and Molecular Biology,* vol. 85, pp. 353-368, 2004.

[15] K. Choi, S. Kim, H. Ha, E. Kil, C. Lee, S. Lee, J. Shim and S. Lee, "Compliant polymer network-mediated fabrication of a bendable plastic crystal polymer electrolyte for flexible lithium-ion batteries," *Journal of Materials Chemistry A,* vol. 1, pp. 5224-5231, 2013.

[16] Z. Wang, "From nanogenerators to piezoelectronics - A decade long study of ZnO nanostructures," *MRS Bulletin,* vol. 37, pp. 814-827, 2012.

[17] J. Rocha, L. Goncalves, P. Rocha, M. Silva and S. Lanceros-Mendez, "Energy Harvesting from Piezoelectric Materials Fully Integrated in Footwear," *IEEE Transactions on Industrial Electronics,* vol. 57, no. 3, 2010.

[18] E. Hasler, L. Stein and G. Harbauer, "Implantable Physiological Power Supply with PVDF Film," *Ferroelectrics,* vol. 60, no. 1, pp. 277-282, 1984.

[19] C.-H. Wong, Z. Dahari, A. A. Manaf and M. A. Miskam, "Harvesting Raindrop Energy with Piezoelectrics: a Review," *Journal of Electronic Materials,* vol. 44, no. 1, pp. 13-21, 2015.

[20] V. Cauda, G. Canavese and S. Stassi, "Nanostructured Piezoelectric Polymers," *Journal of Applied Polymer Science,* vol. 132, no. 13, 2015.

[21] J. Bae and S. Chang, "Characterization of an electroactive polymer (PVDF-TrFE) film-type sensor for health monitoring of composite structures," *Composite Structures,* vol. 131, pp. 1090-1098, 2015.

[22] L. Li, M. Zhang, M. Rong and W. Ruan, "Studies on the Transformation Process of PVDF from α to β Phase by Stretching," *RSC Advances,* vol. 4, no. 8, pp. 3938-3943, 2014.

[23] P. Sajkiewicz, "Crystallization behaviour of poly(vinylidene fluoride)," *European Polymer Journal,* vol. 35, pp. 1581-1590, 1999.

[24] C. Du, B. Zhu and Y. Xu, "Effects of stretching on crystalline phase structure and morphology of hard elastic PVDF fibers," *Journal of Applied Polymer Science,* 2006.

[25] J. Kim, J. Jung, H. Wang, S. Lee, T. Moore, A. Sanguineti, E. Drioli and Y. Lee, "Microporous PVDF membranes via thermally induced phase separation (TIPS) and stretching methods," *Journal of Membrane Science,* vol. 509, pp. 94-104, 2016.

[26] A. Salimi and A. Yousefi, "FTIR Studies of β-Phase Crystal Formation in Stretched PVDF Films," *Polymer Testing,* vol. 22, pp. 699-704, 2003.

[27] S. Lanceros-Mendez, J. Mano, A. Costa and V. Schmidt, "FTIR and DSC studies of

mechanicallly deformed β-PVDF films," *Jounral of Macromolecular Science, Part B,* vol. 40, pp. 517-527, 2001.

[28] J. Gomes, J. Nunes, V. Sencadas and S. Lanceros-Mendez, "Influence of the β-phase content and degree of crystallinity on the piezo- and ferroelectric properties of poly(vinylidene fluoride)," *Smart Material Structures,* vol. 19, 2010.

[29] V. Sencadas, R. Gregorio and S. Lacneros-Mendez, "a to b phase transformation and microstructural changes of PVDF films induced by uniaxial stretch," *Journal of Macromolecular Science, Part B,* vol. 48, pp. 514-525, 2009.

[30] S. Satapathy, S. Pawar, P. Gupta and K. Varma, "Effect of annealing on phase transition in poly(vinylidene fluoride) films prepared using polar solvent," *Bullentin of Material Science,* vol. 34, no. 4, pp. 727-733, 2011.

[31] M. Benz and W. B. Euler, "Determination of the Crystalline Phase of Poly(vinylidene fluoride) Under Different Preparation Conditions Using Differential Scanning Calorimetry and Infrared Spectroscopy," *Journal of Applied Polymer Science,* vol. 89, pp. 1093-1100, 2003.

[32] N. Soin, D. Boyer, K. Prashanthi, S. Sharma, A. Narasimulu, J. Luo, T. Shah, E. Siores and T. Thundat, "Exclusive self-aligned b-phase PVDF films with abnormal piezoelectric coefficient prepared via phase inversion," *Chem. Communication,* vol. 51, pp. 8257-8260,

2015.

[33] S. Ramasundaram, S. Yoon, K. Kim and C. Park, "Preferential formation of electroactive crystalline phases in poly(vinylidene fluoride)/organically modified silicate nanocomposites," *Journal of Polymer Science Part B: Polymer Physics,* vol. 46, pp. 2173-2187, 2006.

[34] A. Gradys, P. Sajkiewicz, S. Adamovsky, A. Minakov and C. Schick, "Crystallization of poly(vinylidene fluoride) during ultra-fast cooling," *Thermochimica Acta,* vol. 461, pp. 153-157, 2007.

[35] Y. Oka and N. Koizumi, "Formation of unoriented form I poly(vinylidene fluoride) by high-rate quenching and its electrical properties," *Bulletin Inst. Chem. Res.,* vol. 63, no. 3, 1985.

[36] J. Scheinbeim, C. Nakafuku, B. Newman and K. Pae, "High-pressure crystallization of poly(vinylidene fluoride)," *Journal of Applied Physics,* vol. 50, 1979.

[37] K. Matsushige, K. Nagata and T. Takemura, "Direct Observation of crystal transformation process of poly(vinylidene fluoride) under high pressure by PSPC X-Ray system," *Japanese Journal of Applied Physics*, vol. 17, no. 3, pp. 467-472, 1978.

[38] S. K. Mahadeva, J. Berring, K. Walus and B. Stoeber, "Effect of Poling Time and Grid Voltage on Phase Transition and Piezoelectricity of Poly(vinyledene Fluoride) Thin Films

using Corona Poling," *Journal of Physics D: Applied Phyiscs,* vol. 46, 2013.

[39] K. Ramadan, D. Sameoto and S. Evoy, "A review of piezoelectric polymer as funtional materials for electromechanical transducers," *Smart Materials and Structures,* vol. 23, 2014.

[40] C. Ribeiro, V. Sencadas, J. Ribelles and S. Lanceros-Mendez, "Influence of processing conditions on polymorphism and nanofiber morphology of electroactive poly(vinylidene fluoride) electrospun membranes," *Soft Materials,* vol. 8, no. 3, pp. 274-287, 2010.

[41] S. Choi, Y. Lee, C. Joo, S. Lee, J. Park and K. Han, "Electrospun PVDF Nanofbier web as polymer electrolyte or seperator," *Electrochimica Acta,* vol. 50, pp. 339-343, 2004.

[42] C. Pan, Y. Hwang, L. Lin and Y.-C. Chen, "Design and Fabrication of Electrospun PVDF Piezo-Energy Harvesters," in *Design and Fabrication of Self-Powered Micro-Harvesters : Rotating and Vibrating Micro-Power Systems*, Singapore, John Wiley & Sons, 2014, pp. 183-264.

[43] K. Hwang, B. Kwon and H. Byun, "Preparation of PVDF Nanofiber Membranes by electrospinning and their use as secondary battery separators," *Journal of Membrane Science,* vol. 378, pp. 111-116, 2011.

[44] J. Zheng, A. He, J. Li and C. Han, "Polymorphism control of poly(vinylidene fluoride) through electrospinning," *Macromolecular Rapid Communications,* vol. 28, pp. 2159-2162,

2007.

[45] G. Zhong, L. Zhang, R. Su, K. Wang, H. Fong and L. Zhu, "Understanding Polymorphism Formation in Electrospun Fibers of Immiscible Poly(vinylidene Fluoride) Blends," *Polymer,* vol. 52, pp. 2228-2237, 2011.

[46] S. Wolff, F. Jirasek, S. Beuermann and M. Turk, "Crystal phase transformation of a into b phase poly(vinylidene fluoride) via particle formation caused by rapid expansion of supercritical solutions," *RSC Advances,* vol. 5, pp. 66644-66649, 2015.

[47] P. Alessi, A. Cortesi, I. Kikic and F. Vecchione, "Plasticiazation of polymers with supercritical carbon dioxide: experimental determination of glass-transition temperatures," *Journal of Applied Polymer Science,* vol. 88, pp. 2189-2193, 2003.

[48] P. Pandey, R. Chauhan and A. Shrivastava, "Carbon dioxide induced plasticization effects in solvent-cast Polyethylene membranes," *Journal of Applied Polymer Science,* vol. 83, pp. 2727-2731, 2002.

[49] Y. Xiang, F. Liu, L. Xue, J. Shen and H. Lin, "Morphology evolution of poly(vinylidene fluoride) membranes during supercritical CO2 assisted phase inversion," *Chinese Journal of Polymer Science,* vol. 32, no. 12, pp. 1628-1638, 2014.

[50] Y. Shieh, T. Hsiao and S. Chang, "CO2 pressure effects on melting, crystallization, and

morphology of poly(vinylidene fluoride)," *Polymer,* vol. 47, pp. 5929-5937, 2006.

[51] P. Thakur, A. Kool, N. Hoque, B. Bagchi, S. Roy, N. Sepay, S. Das and P. Nandy, "Improving the thermal stability, electroactive β phase crystallization and dielectric constant of NiO nanoparticle/C-NiO nanocomposite embedded flexible poly(vinylidene fluoride) thin films," *RSC Advances,* vol. 6, pp. 26288-26299, 2016.

[52] P. Martins, C. Caparros, R. Goncalves, P. Martins, M. Benelmekki, G. Botelho and S. Lanceros-Mendez, "Role of nanoparticle surface charge on the nucleation of the electroactive b-poly(vinylidene fluoride) nanocomposites for sensor and actuator applications," *Journal of Physical Chemistry C,* vol. 116, pp. 15790-15794, 2012.

[53] P. Thakur, A. Kool, B. Bagchi, N. Hoque, S. Das and P. Nandy, "In situ synthesis of Ni(OH)2 nanobelt modified electroactive poly(vinylidene fluoride) thin films: remarkable improvement in dielectric properties," *Phys.Chem.Chem.Phys.,* vol. 17, pp. 13082-13091, 2015.

[54] M. Sebastian, A. Larrea, R. Goncalves, T. Alejo, J. Vilas, V. Sebastian, P. Martins and S. Lanceros-Mendez, "Understanding nucleation of the electroactive b-phase of poly(vinylidene fluoride) by nanostructures," *RSC Advances,* vol. 6, pp. 113007-113015, 2016.

[55] Y. Takahashi, Y. Matsubara and H. Tadokoro, "Mechanisms for crystal phase

transformations by heat treatment and molecular motion in poly(vinylidene fluoride)," *Macromolecules,* vol. 15, pp. 334-338, 1982.

[56] M. Silva, V. Sencadas, G. Botelho, A. Machado, A. Rolo, J. Rocha and S. Lanceros-Mendez, "a and y-PVDF: crystallization kinetics, microstructural variations and thermal behaviour," *Materials Chemistry and Physics,* vol. 122, pp. 87-92, 2010.

[57] W. Prest and D. Luca, "The formation of the γ phase from the α and β polymorphs of polyvinylidene fluoride," *Journal of Applied Physics,* vol. 49, no. 10, pp. 5042-5047, 1978.

[58] R. Gregorio, "Determination of the α, β, and γ crystalline phases of poly(vinylidene fluoride) films prepared at different conditions," *Journal of Applied Polymer Science,* vol. 100, pp. 3272-3279, 2006.

[59] R. Gregorio and C. Cregger, "Morphology and phase transition of high melt temperature crystallized poly(vinylidene fluoride)," *Journal of Materials Science,* vol. 35, pp. 299-306, 2000.

[60] A. Lopes, C. Costa, C. Tavares, I. Neves and S. Lanceros-Mendez, "Nucleation of the electroactive y phase and enhancement of the optical transparency in low filler content poly(vinylidene)/clay nanocomposites," *Journal of Physical Chemistry C,* vol. 115, pp. 18076-18082, 2011.

[61] A. Lopes, S. Carbineiro, M. Pereira, G. Botelho and S. Lanceros-Mendez, "Nanoparticle size and concentration dependence of the electroactive phase content and electrical and optical properties of Ag/Poly(vinylidene fluoride) composites," *ChemPhysChem,* vol. 14, pp. 1926-1933, 2013.

[62] Y. Li, J. Xu, L. Zhu, H. Xu, M. Pan, G. Zhong and Z. Li, "Multiple stage crystallization of gamma phase poly(vinylidene fluoride) induced by ion-diople interaction as reveale by time-resove FTIR and two-dimensional correlation analysis," *Polymer,* vol. 553, pp. 4765-4775, 2014.

[63] J. J. Stroyan, *Processing and characterization of PVDF, PVDF-TrFE, and PVDF-TrFE-PZT Composites,* Washington State University, 2004.

[64] American Society for Testing Materials, "D 3755-97: Dielectric breakdown voltage and dielectric strength of solid electrical insulating materials under direct voltage stress," ASTM International, 1998.

[65] T. Wang and J. West, "Polarization of poly(vinylidene fluoride) by application of breakdown fields," *Journal of Applied Physics,* vol. 53, pp. 6552-6556, 1982.

[66] J. Kenney and S. Roth, "Room temperature poling of poly(vinylidene fluoride) with deposited metal electrodes," *Journal of Research,* vol. 84, no. 6, 1979.

[67] T. R. Dargaville, M. Celina, J. Elliott, P. Chaplya, G. Jones, D. Mowery, R. Assink, R. Clough and J. Martin, "Characterization, performance and optimization of PVDF as a piezoelectric film for advanced space mirror concepts," Sandia National Laboratories, Albuquerque, New Mexico, 2005.

[68] G. Sessler, "Piezoelectricity in polyvinylidenefluoride," *Journal of Acousitcal Society of America,* vol. 70, no. 6, pp. 1596-1608, 1981.

[69] W. Blevin, "Poling rates for films of polyinylidene fluoride," *Applied Physics Letters,* vol. 31, pp. 6-8, 1977.

[70] B. Newman, C. Yoon, K. Pae and J. Scheinbeim, "Piezoelectric activity and field-induced crystal structure transitions in poled poly(vinylidene fluoride) films," *Journal of Applied Physics,* vol. 50, no. 10, pp. 6095-6100, 1979.

[71] F. Mopsik and A. DeReggi, "Poling behavior of polyvinylidene fluoride at room temperature," *Applied Physics Letters,* vol. 44, pp. 65-67, 1984.

[72] S. Chen, K. Yao, F. Tay and L. Chew, "Comparative Investigation of the structure and properties of ferroelectric poly(vinylidene fluoride) and poly(viylidene fluoride-trifluoroethylene) thin films crystallized on substrates," *Journal of Applied Polymer Science,* vol. 116, pp. 3331-3337, 2010.

[73] J. Harrison and Z. Ounaies, "Piezoelectric Polymers," National Aeronautics and Space Administration, Hampton, Virginia, 2001.

[74] B. Gusarov, "PVDF piezoelectric polymers: characterization and application to thermal energy harvesting," Universite Grenoble Alpes, 2015.

[75] T. Zeng, R. Claus, Y. Liu, F. Zhang, W. Du and K. Cooper, "Piezoelectric ultrathin polymer films synthesized by electrostatic self-assembly processing," *Smart Materials and Structure,* vol. 9, pp. 801-804, 2000.

[76] W. Ren, H. Zhou, X. Wu, L. Zhang and X. Yao, "Measurement of piezoelectric coefficients of lead zirconate titanate thin films by the normal load method using a composite tip," *Materials Letters,* vol. 31, pp. 185-188, 1997.

[77] F. Bernard, L. Gimeno, B. Viala, B. Gusarov and O. Cugat, "Direct piezoelectric coefficient measurements of PVDF and PLLA under controlled strain and stress," in *Eurosensors,* Paris, 2017.

[78] J. Liu, B. Pan, H. Chan, S. Zhu, Y. Zhu and Z. Liu, "Piezoelectric coefficient measurement of piezoelectric thin films: an overview," *Materials Chemistry and Physics,* vol. 75, pp. 12-18, 2002.

[79] T. Wang and H. von Seggern, "High electric field poling of electroded poly(vinylidene

fluoride) at room temperature," *Journal of Applied Physics,* vol. 54, pp. 4602-4604, 1983.

[80] D. Das-Gupta and K. Doughty, "Corona chargin and the piezoelectric effect in polyvinylidene fluoride," *Journal of Applied Physics,* vol. 49, p. 4601, 1978.

[81] G. Haghiashtiani and M. A. Greminger, "Fabricatoin, polarization, and characterization of PVDF matrix composites for integrated structural load sensing," *Smart Materials and Structure,* vol. 24, 2015.

[82] T. Kaura, R. Nath and M. Perlman, "Simultaneous stretching and corona poling of PVDF films," *Journal of Physics D: Applied Physics,* vol. 24, pp. 1848-1852, 1991.

[83] J. Liu, X. Lu and C. Wu, "Effect of Preparation Methods on Crystallization Behavior and Tensile Strength of Poly(vinylidene fluoride) Membranes," *Membranes,* vol. 3, pp. 389-405, 2013.

[84] X. Cai, T. Lei, D. Sun and L. Lin, "A critical analysis of the α, β and γ phases in poly(vinylidene fluoride) using FTIR," *RSC Advances,* vol. 7, pp. 15382-15389, 2017.

[85] R. Imamura, A. Silva and J. R. Gregorio, "γ to β phase transformation induced poly(vinylidene fluoride) by stretching," *Journal of Applied Polymer Science,* vol. 110, pp. 3242-3246, 2008.

[86] S. N. Leung, A. Wong, L. C. Wang and C. B. Park, "Mechanism of extensional stress-

induced cell formation in polymeric foaming processes with the presence of nucleating agents," *Journal of Supercritical Fluids,* vol. 63, pp. 187-198, 2012.

[87] S. Anton, K. Farinholt and A. Erturk, "Piezoelectret foam-based vibration energy harvesting," *Journal of Intelligent Material Systems and Structures,* vol. 25, pp. 1681-1692, 2014.

[88] M. Faraday, Experimental Researches in Electricity, Volume 1, London: Richard and John Edward Taylor, 1839.

# APPENDIX A: SOLIDWORKS DRAWINGS FOR CONTACT POLING SYSTEM

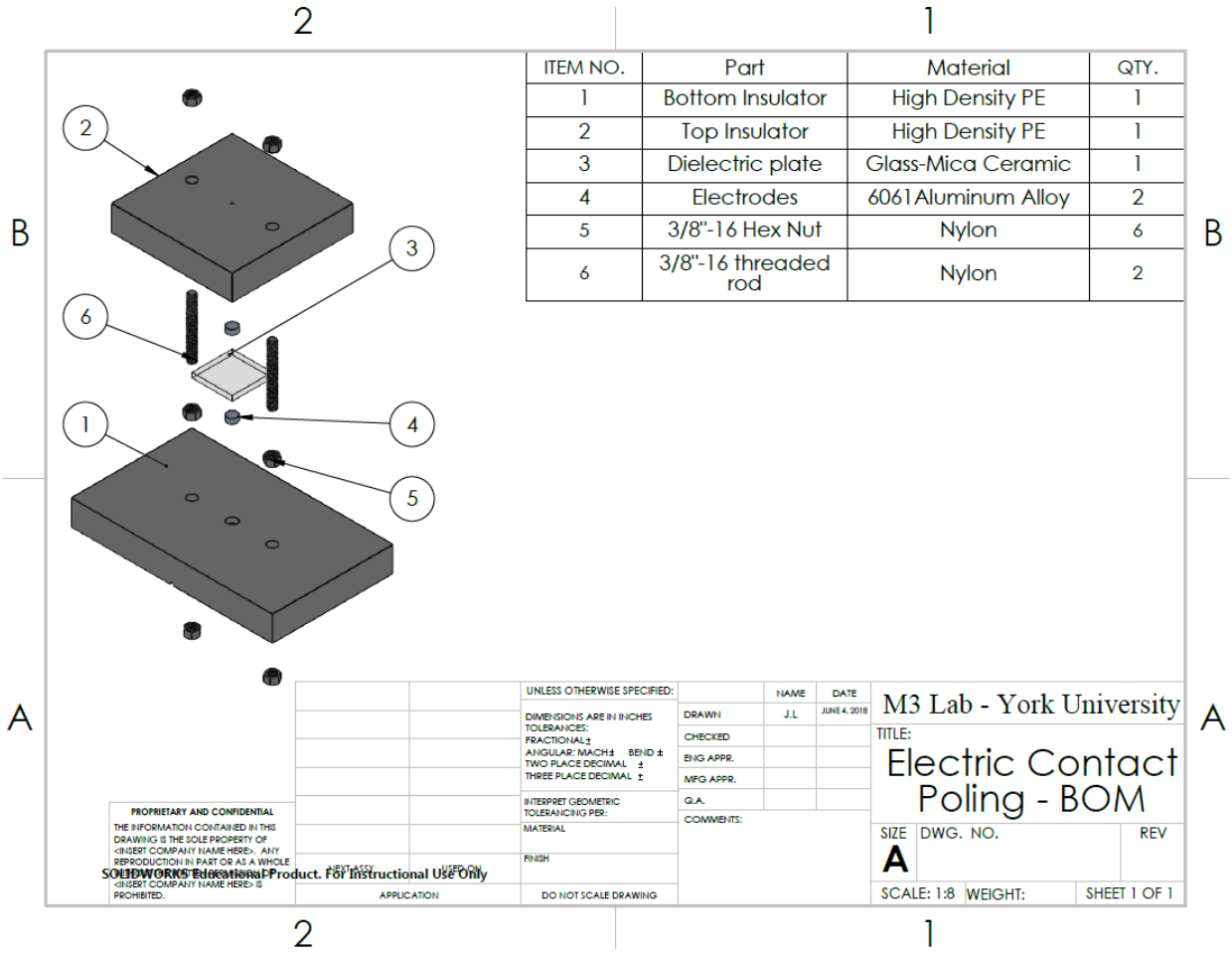

| ITEM NO. | Part | Material | QTY. |
|---|---|---|---|
| 1 | Bottom Insulator | High Density PE | 1 |
| 2 | Top Insulator | High Density PE | 1 |
| 3 | Dielectric plate | Glass-Mica Ceramic | 1 |
| 4 | Electrodes | 6061Aluminum Alloy | 2 |
| 5 | 3/8"-16 Hex Nut | Nylon | 6 |
| 6 | 3/8"-16 threaded rod | Nylon | 2 |

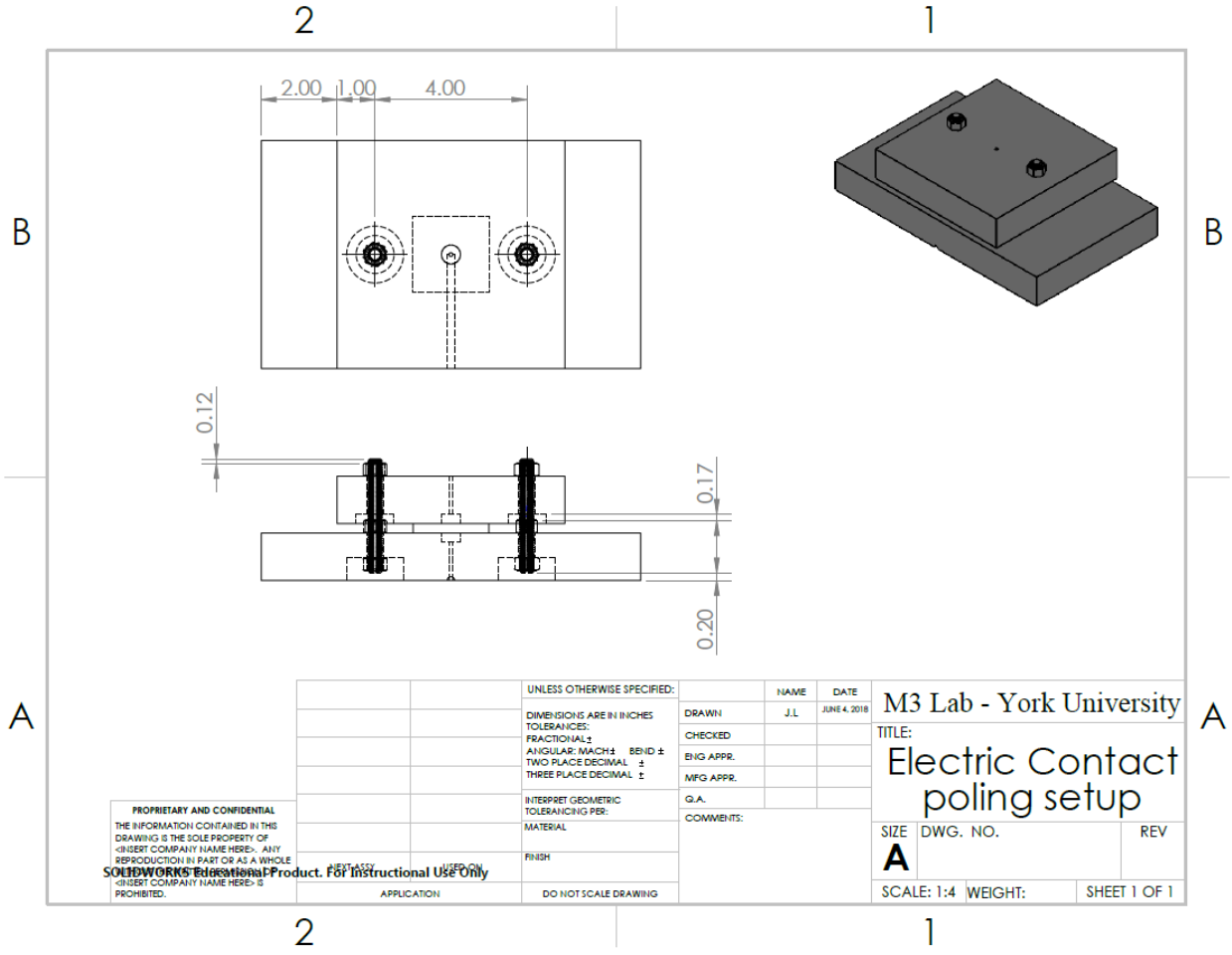
2
1
B
A
2.00
1.00
4.00
0.12
0.17
0.20
UNLESS OTHERWISE SPECIFIED:
DIMENSIONS ARE IN INCHES
TOLERANCES:
FRACTIONAL ±
ANGULAR: MACH ± BEND ±
TWO PLACE DECIMAL ±
THREE PLACE DECIMAL ±
INTERPRET GEOMETRIC TOLERANCING PER:
MATERIAL
FINISH
DO NOT SCALE DRAWING
NAME
DATE
DRAWN
J.L
JUNE 4, 2018
CHECKED
ENG APPR.
MFG APPR.
Q.A.
COMMENTS:
M3 Lab - York University
TITLE:
Electric Contact poling setup
SIZE
A
DWG. NO.
REV
SCALE: 1:4
WEIGHT:
SHEET 1 OF 1
PROPRIETARY AND CONFIDENTIAL
THE INFORMATION CONTAINED IN THIS DRAWING IS THE SOLE PROPERTY OF <INSERT COMPANY NAME HERE>. ANY REPRODUCTION IN PART OR AS A WHOLE WITHOUT THE WRITTEN PERMISSION OF <INSERT COMPANY NAME HERE> IS PROHIBITED.
NEXT ASSY
USED ON
APPLICATION
SOLIDWORKS Educational Product. For Instructional Use Only

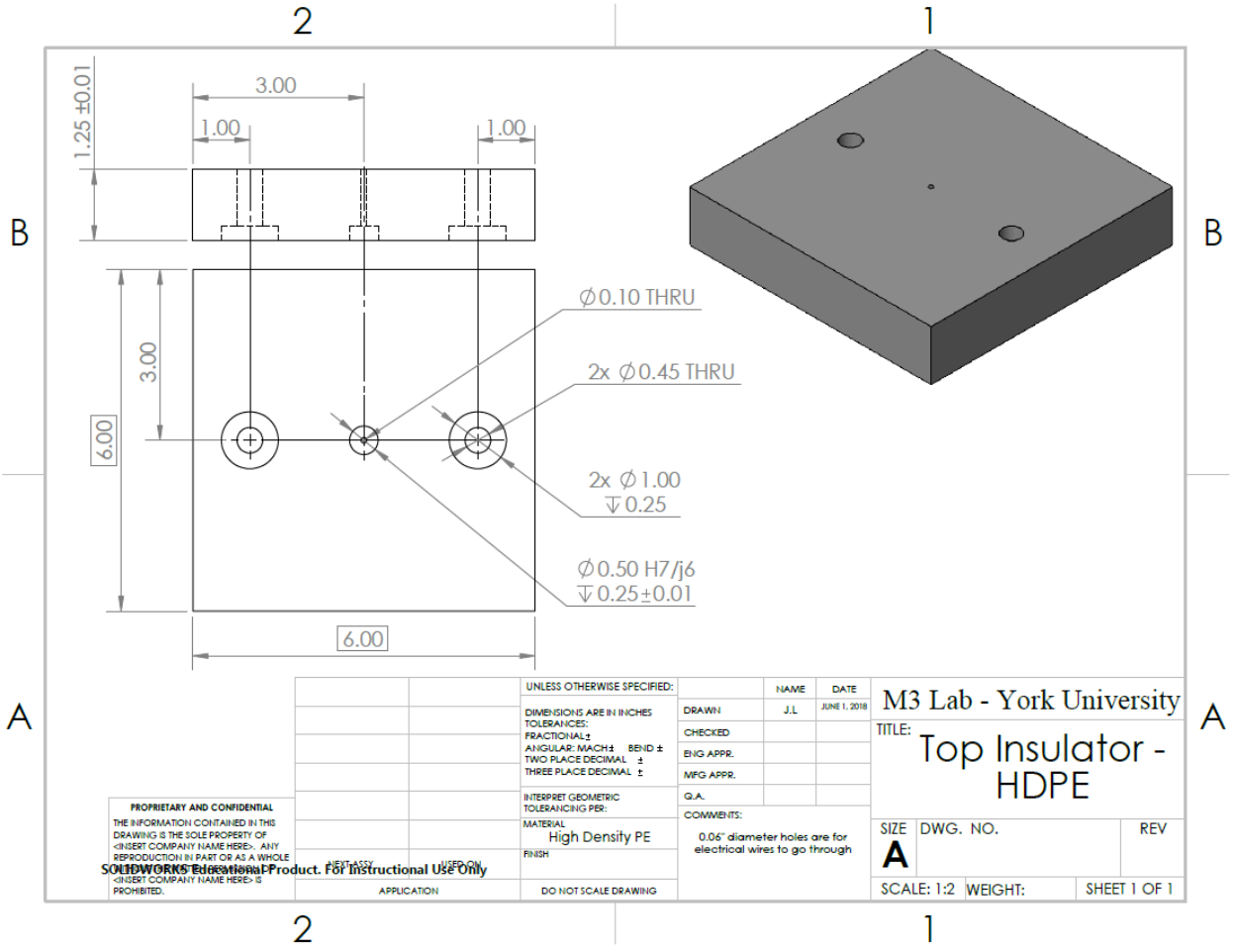
2
1
B
A
3.00
1.00
1.00
1.25 ±0.01
3.00
6.00
6.00
∅0.10 THRU
2x ∅0.45 THRU
2x ∅1.00
↧0.25
∅0.50 H7/j6
↧0.25±0.01
UNLESS OTHERWISE SPECIFIED:
DIMENSIONS ARE IN INCHES
TOLERANCES:
FRACTIONAL ±
ANGULAR: MACH ± BEND ±
TWO PLACE DECIMAL ±
THREE PLACE DECIMAL ±
INTERPRET GEOMETRIC TOLERANCING PER:
MATERIAL
High Density PE
FINISH
DO NOT SCALE DRAWING
NAME
DATE
DRAWN
J.L
JUNE 1, 2018
CHECKED
ENG APPR.
MFG APPR.
Q.A.
COMMENTS:
0.06" diameter holes are for electrical wires to go through
M3 Lab - York University
TITLE:
Top Insulator - HDPE
SIZE
A
DWG. NO.
REV
SCALE: 1:2
WEIGHT:
SHEET 1 OF 1
PROPRIETARY AND CONFIDENTIAL
THE INFORMATION CONTAINED IN THIS DRAWING IS THE SOLE PROPERTY OF <INSERT COMPANY NAME HERE>. ANY REPRODUCTION IN PART OR AS A WHOLE WITHOUT THE WRITTEN PERMISSION OF <INSERT COMPANY NAME HERE> IS PROHIBITED.
NEXT ASSY
USED ON
APPLICATION
SOLIDWORKS Educational Product. For Instructional Use Only

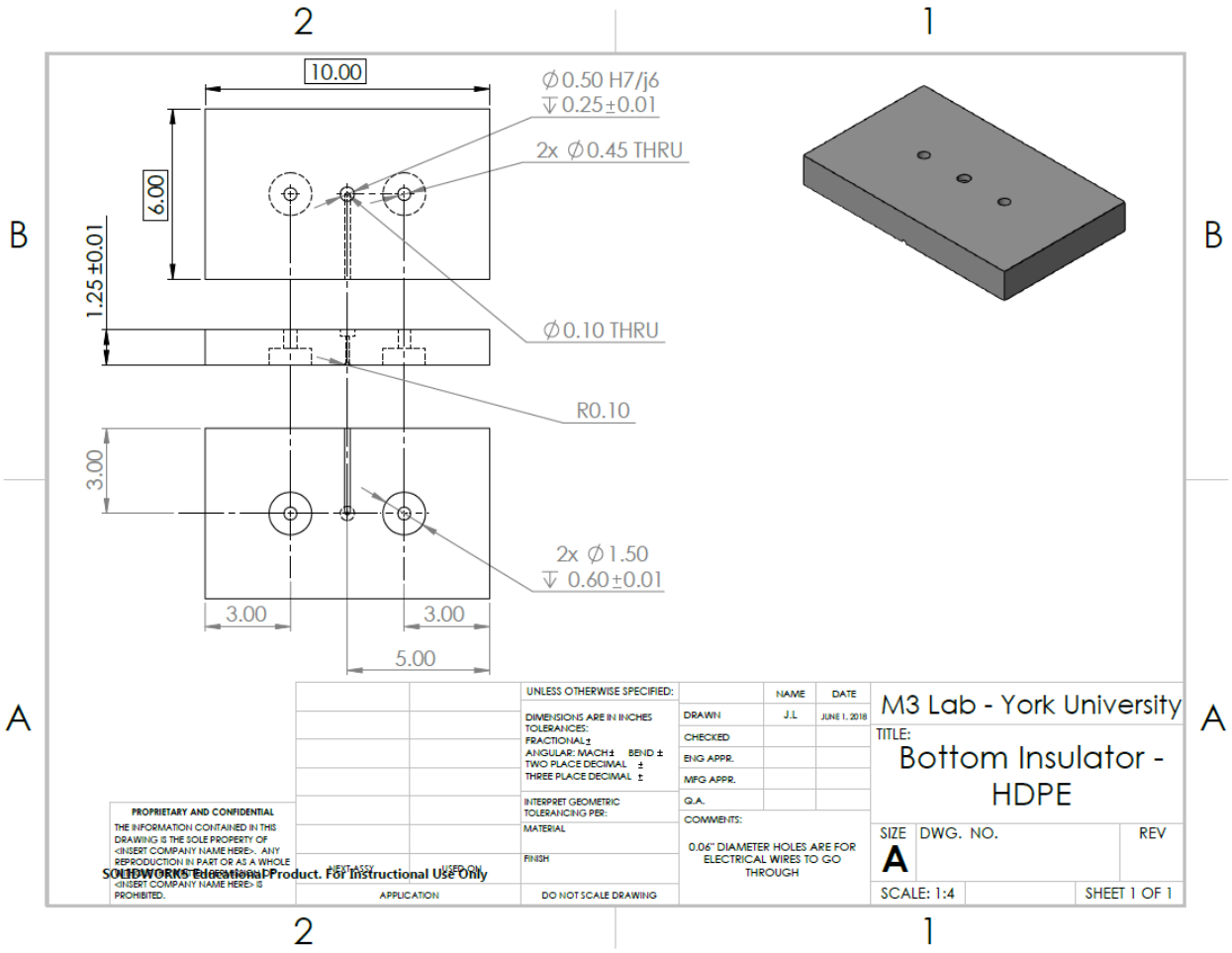
2
1
B
A
10.00
6.00
1.25 ±0.01
3.00
3.00
3.00
5.00
⌀0.50 H7/j6
↧0.25±0.01
2x ⌀0.45 THRU
⌀0.10 THRU
R0.10
2x ⌀1.50
↧ 0.60±0.01
UNLESS OTHERWISE SPECIFIED:
DIMENSIONS ARE IN INCHES
TOLERANCES:
FRACTIONAL ±
ANGULAR: MACH ± BEND ±
TWO PLACE DECIMAL ±
THREE PLACE DECIMAL ±
INTERPRET GEOMETRIC TOLERANCING PER:
MATERIAL
FINISH
DO NOT SCALE DRAWING
NAME
DATE
DRAWN
J.L
JUNE 1, 2018
CHECKED
ENG APPR.
MFG APPR.
Q.A.
COMMENTS:
0.06" DIAMETER HOLES ARE FOR ELECTRICAL WIRES TO GO THROUGH
M3 Lab - York University
TITLE:
Bottom Insulator - HDPE
SIZE
A
DWG. NO.
REV
SCALE: 1:4
SHEET 1 OF 1
PROPRIETARY AND CONFIDENTIAL
THE INFORMATION CONTAINED IN THIS DRAWING IS THE SOLE PROPERTY OF <INSERT COMPANY NAME HERE>. ANY REPRODUCTION IN PART OR AS A WHOLE WITHOUT THE WRITTEN PERMISSION OF <INSERT COMPANY NAME HERE> IS PROHIBITED.
NEXT ASSY
USED ON
APPLICATION
SOLIDWORKS Educational Product. For Instructional Use Only

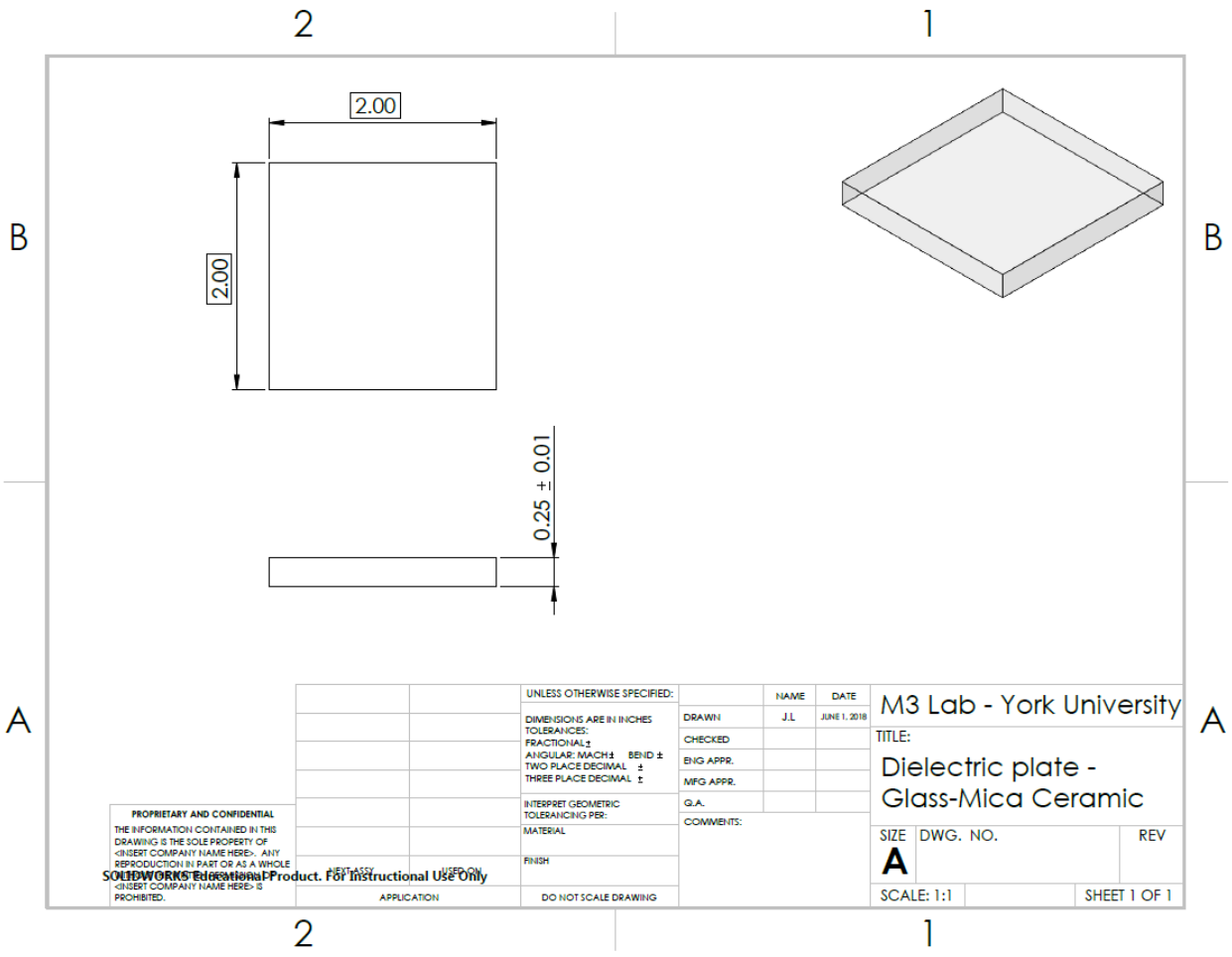
2
1
2.00
2.00
0.25 ± 0.01
B
A
UNLESS OTHERWISE SPECIFIED:
DIMENSIONS ARE IN INCHES
TOLERANCES:
FRACTIONAL ±
ANGULAR: MACH ± BEND ±
TWO PLACE DECIMAL ±
THREE PLACE DECIMAL ±
INTERPRET GEOMETRIC TOLERANCING PER:
MATERIAL
FINISH
DO NOT SCALE DRAWING
NAME
DATE
DRAWN
J.L
JUNE 1, 2018
CHECKED
ENG APPR.
MFG APPR.
G.A.
COMMENTS:
M3 Lab - York University
TITLE:
Dielectric plate - Glass-Mica Ceramic
SIZE
A
DWG. NO.
REV
SCALE: 1:1
SHEET 1 OF 1
PROPRIETARY AND CONFIDENTIAL
THE INFORMATION CONTAINED IN THIS DRAWING IS THE SOLE PROPERTY OF <INSERT COMPANY NAME HERE>. ANY REPRODUCTION IN PART OR AS A WHOLE WITHOUT THE WRITTEN PERMISSION OF <INSERT COMPANY NAME HERE> IS PROHIBITED.
NEXT ASSY
USED ON
APPLICATION
SOLIDWORKS Educational Product. For Instructional Use Only

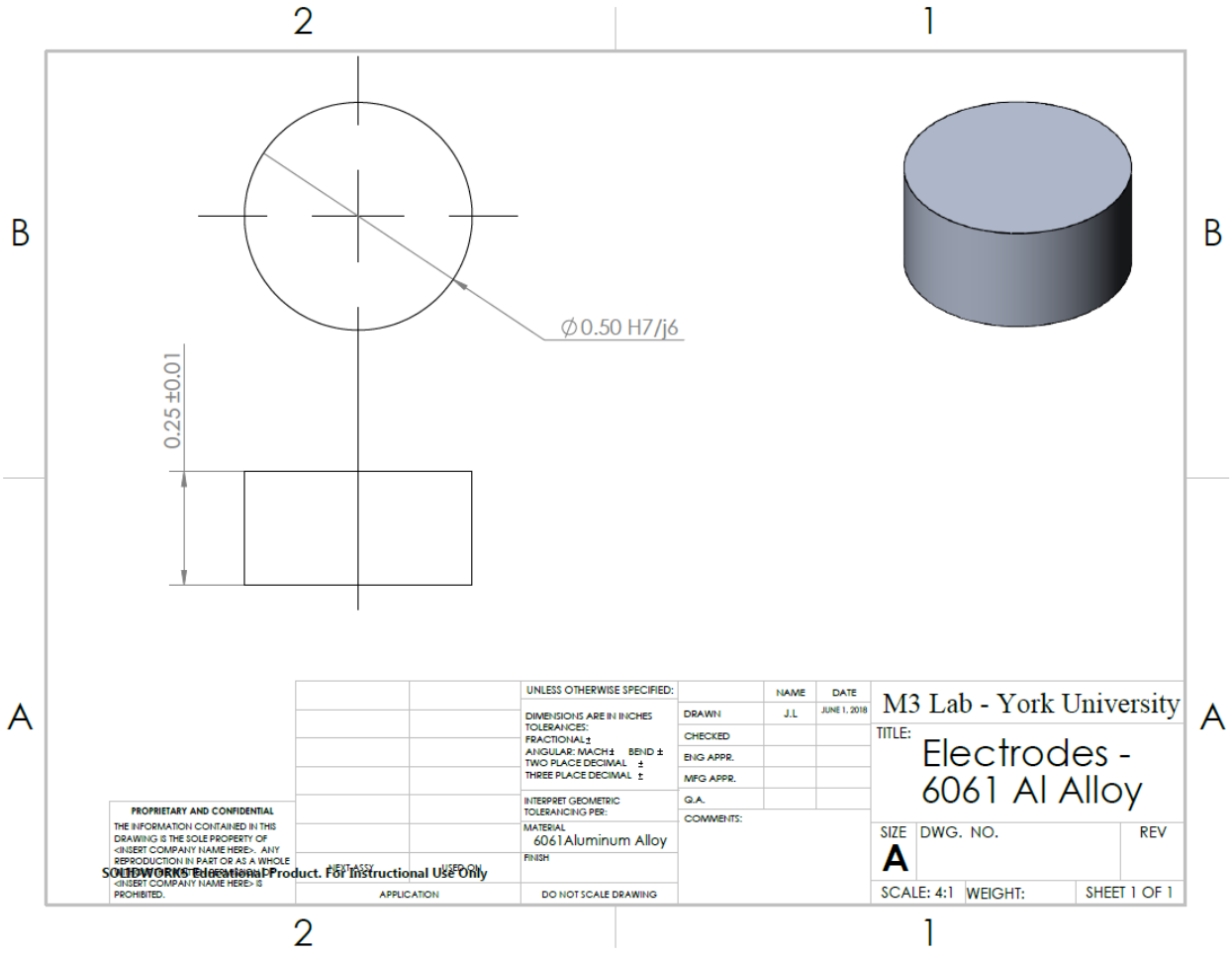
2
1
B
B
A
A
∅0.50 H7/j6
0.25 ±0.01
UNLESS OTHERWISE SPECIFIED:
DIMENSIONS ARE IN INCHES
TOLERANCES:
FRACTIONAL ±
ANGULAR: MACH ± BEND ±
TWO PLACE DECIMAL ±
THREE PLACE DECIMAL ±
INTERPRET GEOMETRIC TOLERANCING PER:
MATERIAL
6061Aluminum Alloy
FINISH
DO NOT SCALE DRAWING
NAME
DATE
DRAWN
J.L
JUNE 1, 2018
CHECKED
ENG APPR.
MFG APPR.
Q.A.
COMMENTS:
M3 Lab - York University
TITLE:
Electrodes - 6061 Al Alloy
SIZE
A
DWG. NO.
REV
SCALE: 4:1
WEIGHT:
SHEET 1 OF 1
PROPRIETARY AND CONFIDENTIAL
THE INFORMATION CONTAINED IN THIS DRAWING IS THE SOLE PROPERTY OF <INSERT COMPANY NAME HERE>. ANY REPRODUCTION IN PART OR AS A WHOLE WITHOUT THE WRITTEN PERMISSION OF <INSERT COMPANY NAME HERE> IS PROHIBITED.
NEXT ASSY
USED ON
APPLICATION
SOLIDWORKS Educational Product. For Instructional Use Only